Laser Beam Interaction with Spheroidal Droplets: Computation and Measurement

PhD Thesis
M. Sc. Haitao Yu | Matrikelnummer: 1591246
Fachgebiet Strömungslehre und Aerodynamik
Maschinenbau, Technische Universität Darmstadt

TECHNISCHE
UNIVERSITÄT
DARMSTADT

Laser Beam Interaction with Spheroidal Droplets: Computation and Measurement

Vom Fachbereich Maschinenbau

an der Technische Universität Darmdtadt

zur

Erlangung des Grades eines Doktors der Naturwissenschaften

(Dr. rer. nat.)

genehmigte

Dissertation

vorgelegt von

M.Sc. Haitao Yu

aus Shangdong, China

Berichterstatter: Prof. Dr.–Ing. Cameron Tropea

Mitberichterstatter: Prof. Dr.–Ing. Thomas Weiland

Tag der Einreichung: 20.08.2013

Tag der mündlichen Prüfung: 27.11.2013

Darmstadt 2013

D17

Laser Beam Interaction with Spheroidal Droplets: Computation and Measurement

Erklärung

Hiermit erkläre ich, dass ich die vorliegende Arbeit, abgesehen von den in ihr ausdrücklich genannten Hilfen, selbständig verfasst habe.

Darmstadt, den 17. December 2013   Haitao Yu

Acknowledgements

First of all, I would like to express my sincere gratitude to my supervisor, Prof. Cameron Tropea, for his great encouragement and support. All the fruits of this research are results of his patient instructions and fruitful advices. I will never forget that he spent his spare time to discuss with me about my research work and to help me correct my manuscripts and conference reports as well as the thesis.

Acknowledgement is given to my co-supervisor, Prof. Thomas Weiland, for his kind support on my research work and the organization of the periodic meetings with Prof. Cameron Tropea and me.

I acknowledge Dr. Feng Xu in Jet Propulsion Laboratory, California Institute of Technology, for his excellent guidance and great encouragement during my Ph. D study. His enthusiastic encouragement allowed me to face the difficulties and challenges encountered during this research work. I also would like to express my respect for him for his carefulness in correcting my manuscripts and very useful comments.

I would like to give my thanks to Prof. James A. Lock in Cleveland State University, USA, for his helpful remarks and insightful suggestions on my research work on LIP conference in Rouen in 2012. Thanks are also given to him for his encouragements on my future work.

Then, I would like give my sincere acknowledgement to Mrs. Stephanie Lath, the secretary in Fachgebiet Strömungslehre und Aerodynamik (SLA), for her kind help. Without her help, I cannot prepare the experimental materials and implement my experiment research so successfully. Thanks are also given to Mrs. Birgit Neuthe and Mrs. Petra Fuhrmann for their kind help on my work. Moreover I also wish to express my gratitude to Ms. Kathleen Feustel and Mr. Denis Schinko, IT administrators in SLA, and Ilona Kaufhold, head of workshop in SLA, for their assistence to my research work. Acknowledgements are also given to Dr. Walter Schäfer and M. Sc. Patrick Stegmann for the useful and fruitful discussions with me. I also would like give my thanks to Chi-Yao Chang, Imdat Maden, Ilja Buchmüller, Hai Li, Lukas Kutej and other colleagues in SLA for their encouragement and help.

Furthermore, acknowledgement is due to Prof. Jianqi Shen and Prof. Xiaoshu Cai for their useful suggestions on my research career. I would like to express my respect to their scientific competence. Special graditudes are given to Prof. Jianqi Shen for kindly providing

me with his Mie program. I also would like to give my great thanks to Dr. Chunxia Feng, in Philips Lumileds Lighting Company, for many wonderful conversations and her encouragements on my work and life, which are always the inspiration of my work. And thanks are due to Dr. Bin Yu, Dr. Huarui Wang, Dr. Song Liu, Dr. Yuehuan Wei and Guilin Liu for their encouragement and helping on searching several references .

Most of all, I would like to give my appreciation to my parents for their selfless love and support. Their encouragement has always been the source of strength and inspiration. Thanks are due to my bother and sister for their supporting of our family.

Abstract

Sprays and droplets are involved in numerous industrial processes and in nature, e.g. fuel injection in combustion chambers, painting, spray cooling, spray coating, chemical engineering, cloud physics, etc. The understanding of the light scattering features from the droplets, or particles in general, lays the foundation for extending existing techniques or devising novel techniques for particle characterization. The optical techniques are clearly advantageous over sampling, because of their non-intrusiveness and immediacy of results. Typical particle characteristics of interest include refractive index, size, velocity, and especially for non-spherical particles, some information regarding shape or form and orientation. However, most of existing optical techniques are only available for the measurement of spherical particles. In this thesis, the light scattering from a spheroid is studied and the generalized rainbow technique is proposed for droplet non-sphericity measurement.

First, the vector ray tracing (VRT) model is employed to simulate the optical caustic structures in the primary rainbow region of oblate spheroidal droplets, which includes the rainbow and hyperbolic umbilic (HU) fringes. The location of cusp caustic is calculated by use of the VRT simulation and compared with that calculated by using analytic solution, exhibiting excellent agreement. Furthermore, the evolution process of the optical caustic structures is consistent with the experimental observation. It reveals that the optical caustic structures in the primary rainbow region can be used to measure the non-sphericity of oblate droplets. The VRT model can also be used to simulate and predict the optical caustic structures observed in higher-order rainbows. As a further validation, the cusp location and optical caustic structures in the secondary rainbow region also have been studied using the VRT method. The secondary rainbow fringe, as well as the location and opening rate of the cusp caustic provide a further avenue for non-sphericity measurement of oblate droplets.

Then the character of the generalized rainbow pattern from a spheroidal water droplet is investigated experimentally. In the experiment, light scattering from spheroidal water droplets in the vicinity of the primary rainbow region has been observed to contain a variety of characteristic interference patterns which are the generalization of the rainbow from a sphere. These patterns start from being a fold rainbow, change to transverse cusp caustics

and then to hyperbolic umbilic catastrophe as the aspect ratio of the droplet increases. A comparison of the intensity distribution of the observed rainbow patterns in the horizontal equatorial plane with those of Airy simulation reveals that these patterns can be used for characterizing droplets, in particular for determining the refractive index and the diameter of the spheroidal droplet in the equatorial plane.

According to the generalized rainbow patterns and Airy approximation, the refractive index and equatorial diameter of water droplets can be inverted from the corresponding generalized rainbow patterns. A comparison of the refractive indices inverted from the corresponding generalized rainbow patterns with that of pure water shows good agreement with absolute errors less than 0.5×10^{-4}. The water droplet diameters in the horizontal equatorial plane are calculated from the generalized rainbow patterns and compared to that measured by direct imaging. It is shown that the relative errors of droplet diameters associated with the generalized rainbow patterns lie between -5% and 5%; hence reliable diameter estimations of droplets can be obtained from the generalized rainbow patterns. The curvatures of simulated rainbow fringes are compared with observed ones from the generalized rainbow patterns, in which good agreement is also shown. Since for a given type of droplet, the curvatures of the rainbow fringes are only a function of the aspect ratios, the non-sphericity (in terms of aspect ratio) of water droplets are inferred from the relevant generalized rainbow patterns. The relative errors of aspect ratios calculated from the generalized rainbow pattern lie between -1% and 1%. Accordingly, the complete informations of a spheroidal water droplet in terms of geometric and optical properties are obtained.

Then, the evolution of the optical caustic structures for tilted spheroidal droplets is investigated. The rainbow fringes are tilted counterclockwise as the spheroidal droplet is tilted counterclockwise and vice versa. The changes of the fringes depend on the aspect ratio and tilt angle. A preliminary experiment for tilted spheroidal droplet is shown.

Furthermore, Möbius's approximation is modified to calculate the deviation between the geometrical rainbow angle for an ellipse and that for a sphere. And the vector ray tracing model is also used to compute the rainbow angle deviation for an ellipse, which agrees with modified Möbius equation for small eccentricity. Moreover, the application range of Möbius's approximation is also investigated. It is demonstrated that, for small eccentricity

(0.95≤a/c ≤1.05), the Möbius's approximation can predict the rainbow angle difference of ellipse.

Keywords:

Zusammenfassung

Sprays und Tropfen treten in verschiedenen industriellen Prozessen und in der Natur auf, z.B. Treibstoffeinspritzung in Brennstoffkammern, Lackierungen, Spraykühlung, Spraybeschichtung, chemische Reaktionen, atmosphärische Physik und vieles mehr. Das Verständnis der Lichtstreuungsmerkmale der Tropfen oder kleiner Teilchen im Allgemeinen bestimmt die Grundlagen zur Erweiterung bestehender Methoden oder zur Entwicklung neuer Techniken zur Partikelcharakterisierung. Optische Methoden sind hier klar im Vorteil gegenüber direkter Stichprobenentnahme, aufgrund ihrer nicht-invasiven Natur und der sofortige Verfügbarkeit der Resultate. Typische Eigenschaften von Partikeln die untersucht werden sind der Brechungsindex, die Größe, Geschwindigkeit und besonders für nicht-sphärische Teilchen jegliche Information betreffend Gestalt und Orientierung. Allerdings sind die meisten optischen Messmethoden nur für die Charakterisierung von sphärischen Teilchen bestimmt. In dieser Dissertation wird die Lichtstreuung von einem Sphäroid untersucht und die verallgemeinerte Regenbogen-Methode (*generalized rainbow technique*) wird vorgeschlagen, um die Abplattung eines Tropfens zu messen.

Zunächst verwenden wir ein vektorielles Strahlverfolgungsmodel (Vector Ray-Tracing), um die optischen Kaustiken in der primären Regenbogenregion eines oblat-sphäroiden Tropfens zu simulieren, die den konventionellen Regenbogen und hyperbolisch-umbilische (HU) Muster miteinschließen. Die Position dieser Scheitelpunktskaustik wird mit der VRT-Simulation bestimmt und mit einer analytischen Lösung verglichen. Hierbei wurde eine exzellente Übereinstimmung festgestellt. Des Weiteren ist der simulierte Evolutionsprozess der optischen Kaustik-Strukturen deckungsgleich mit den experimentellen Beobachtungen. Es zeigt sich, dass die optischen Kaustik-Strukturen in der primären Regenbogenregion dazu genutzt werden können, die Abplattung von oblaten Tropfen zu messen. Das VRT-Modell kann ebenfalls dazu benutzt werden, die optischen Kaustik-Strukturen in Regenbögen höherer Ordnung zu simulieren. Als weitere Validierung wurden die Form der Kaustiken und der Ort des Scheitelpunkts in der sekundären Regenbogenregion mit dem VRT-Modell untersucht. Das sekundäre Regenbogenmuster sowie der Ort und die Öffnungsrate der hyperbolisch-umbilischen (Sattelpunkts-) Kaustik zeigen einen weiteren Weg zur Messung der Abplattung von oblaten Tropfen auf.

Im Anschluss wurde der Charakter des verallgemeinerten Regenbogenmusters von Wassertropfen experimentell untersucht. Im Experiment wurde festgestellt, daß Streulicht in der Nähe der primären Regenbogenregion von sphäroiden Wassertropfen eine Reihe von charakteristischen Mustern aufweist, die die Verallgemeinerung des Regenbogens eines gänzlich runden Tropfens darstellen. Diese Muster beginnen mit zunehmender Streckung des Tropfens als gewöhnliche Falten-Kaustik, ändern sich zu einer transversalen Sattelpunkts-Kaustik und schließlich zu einer hyperbolisch-umbilischen Kaustik. Ein Vergleich der Regenbogenmuster in der Äquatorialebene mit der Auswertung einer Airy-Funktion zeigt, daß diese Muster zur Charakterisierung von Tropfen genutzt werden können, insbesondere zur Bestimmung des Brechungsindex und des Durchmessers des Tropfens in der Äquatorialebene.

Gemäß der verallgemeinerten Regenbogenmuster und der Airy-Approximation kann der Brechungsindex und der Äquatorialdurchmesser von Wassertropfen aus den korrespondierenden Regenbogenmustern invertiert werden. Der Vergleich der Brechungsindices, invertiert von den zugehörigen verallgemeinerten Regenbogenmustern, mit denen von reinem Wasser zeigt gute Übereinstimmung mit absoluten Fehlern in der Größenordnung von weniger als $0,5 \times 10^{-4}$. Die Durchmesser der Tropfen in der Äquatorialebene wurden aus den verallgemeinerten Regenbogenmustern berechnet und mit den durch direkte Photographie Bestimmten verglichen. Es wurde gezeigt, daß der relative Fehler bei der Bestimmung des Tropfendurchmessers aus den verallgemeinerten Regenbogenmustern bei 5 Prozent liegt, was die Zuverlässigkeit der verwendeten Methode bestätigt. Die Krümmung der simulierten Regenbogenmuster wurde mit der an verallgemeinerten Regenbogenmustern beobachteten verglichen und eine gute Übereinstimmung gefunden. Da die Krümmung des Regenbogens für einen spezifischen Tropfen nur eine Funktion der Streckung ist, kann die Abplattung (ausgedrückt durch die Streckung) aus den relevanten verallgemeinerten Regenbogenmustern abgeleitet werden. Die relativen Fehler der Streckungen berechnet aus den verallgemeinerten Regenbogenmustern liegen im Bereich von einem Prozent. Dementsprechend können sämtliche geometrischen und optischen Eigenschaften eines sphäroiden Tropfens gewonnen werden.

Im Anschluss ist die Entwicklung der optischen Kaustik-Strukturen von zur Laborebene geneigten sphäroiden Tropfen untersucht worden. Die Regenbogen Muster sind bei gegen

den Uhrzeigersinn geneigten sphäroiden Tropfen ebenfalls gegen den Uhrzeigersinn geneigt und umgekehrt. Die Änderungen in den Beugungsmustern hängen von der Streckung und dem Neigungswinkel ab. Ein vorläufiger experimenteller Aufbau für einen geneigten sphäroiden Tropfen wurde aufgezeigt.

Des Weiteren wurde Möbius Näherung abgewandelt, um die Abweichung des Regenbogenwinkels zwischen einer Ellipse und eines Kreises zu berechnen. Und das Vektorstrahlverfolgungsmodell wurde ebenfalls benutzt, um die Abweichung des Regenbogenwinkels für eine Ellipse zu bestimmen. Die Ergebnisse stimmen mit der modifizierten Möbius-Näherung für kleine Exzentrizitäten überein. Zusätzlich wurde die Anwendbarkeitsgrenze von Möbius-Approximation ebenfalls untersucht. Es wurde gezeigt, dass für kleine Exzentrizität, also einer Streckung um 5 %, die Möbius-Näherung die Differenz des Regenbogenwinkels einer Ellipse vorhersagen kann.

Schlüsselworte:

Airy-Approximation, Katastrophen-Optik, Debye-Reihen, Beugungskatastrophe, geometrische Optik-Approximation, allgemeine Regenbogenmuster, Lorenz-Mie-Theorie, sphäroide Tropfen, Regenbogenmuster, vektorielle Strahlverfolgung

Contents

Contents

List of symbols and abbreviations

Roman symbols

a	radius of spherical particle (m)
	long semi-diameter of ellipse (m)
	equatorial diameter of spheroid (m)
	parameter for Airy integral
a_n	Mie coefficient
a_{GRP}	equatorial diameter of spheroidal droplet inverted from the corresponding generalized rainbow patterns (m)
A	amplitude of electric vector (kg·m·s^{-3}·A^{-1})
Ai	Airy function
b	semi-principal axis of spheroid along the y axis (m)
b_n	Mie coefficient
$\mathbf{B}$	magnetic induction (kg·s^{-2}·A^{-1})
c	short semi-diameter of the ellipse (m)
	semi-principal axis of spheroid along the z axis (m)
C	constant (C=0.3137)
C_1, C_2, C_3	control parameters in catastrophe optics
d	diameter of spherical particle (m)
D	diameter of spheroidal particle in the horizontal equatorial plane (m)
$\mathbf{D}$	electric displacement (s·A·m^{-2})
$D^{(p)}$	divergence factor
$\mathbf{E}$	electric field (kg·m·s^{-3}·A^{-1})
E_{10}	incident electric field component for the perpendicularly polarized direction (kg·m·s^{-3}·A^{-1})
E_{20}	incident electric field component for the parallel polarized direction (kg·m·s^{-3}·A^{-1})
E_1	scattered amplitude for the perpendicularly polarized direction (kg·m·s^{-3}·A^{-1})
E_2	scattered amplitude for the parallel polarized direction (kg·m·s^{-3}·A^{-1})
F	Airy integral

h	parameter for Airy approximation
H	diameter of spheroid along the vertical axis of the rotational symmetry (m)
H	magnetic field (A·m^{-1})
$H^{(2)}_{n+\frac{1}{2}}$	Hankel function of the second kind
i	dimensionless intensity of un-polarized scattered light
i_1, i_2	dimensionless intensities for the perpendicularly and parallel polarized directions of scattered light
$i_j^{(p)}$	dimensionless intensity due to the reflection and/or the refraction for the emergent ray of order p
I_0	incident light intensity (cd)
$I_j^{(p)}$	scattering light intensity (cd)
j	integer representing the perpendicularly and parallel polarized directions of light respectively (j=1, 2)
J$_f$	electric current density (A·m^{-2})
J_1	the first order Bessel function
$J_{n+\frac{1}{2}}$	Bessel function of the first kind
$J_{1/3}$, $J_{-1/3}$	Bessel functions
k	wave number (m^{-1})
$K_{1/3}$	modified Bessel function
L$_0$	incident ray
L$_r$, **L**$_{12}$, **L**$_{23}$	reflection rays
L$_{01}$, **L**$_1$, **L**$_2$, **L**$_3$	refraction rays
m	relative refractive index
m_1, m_2	refractive indexes of the ambient medium and the particle
m_0, n_0, p_0	vector components of light ray
m_{GRP}	relative refractive index of water droplet inverted from the corresponding generalized rainbow patterns
n	real part of complex refractive index

n	unit normal pointing from the first medium into the second medium
	unit normal at the incident point on the interface between the two media
$\mathbf{n}_0$	unit vector along the direction of the incident ray
$\mathbf{n}_1$	unit vector along the reflection ray
$\mathbf{n}_2$	unit vector along the refractive ray
$\mathbf{n}_A$, $\mathbf{n}_B$, $\mathbf{n}_C$, $\mathbf{n}_D$	surface normals at point A, *B*, *C*, and *D* respectively
n_{stop}	criterion for the terminating order of the Mie simulation
p	order of the emerging ray
q, l	integers
$P_n^{(1)}$	associated Legendre function
r	location of one point in polar spherical coordinate (m)
r	distance of one point off the origin in polar spherical coordinate (m)
r_{GRP}	aspect ratio of water droplet inverted from the corresponding generalized rainbow patterns
$r_{Imaging}$	aspect ratio of water droplet measured by imaging
r_1, r_2	Fresnel coefficients
s	integer denoting +1 or -1
S_1, S_2	Mie scattering amplitudes for two polarized directions
$S_{diffraction}$	dimensionless amplitude of diffraction
$S_{reflection}$	dimensionless amplitude of the reflection for the emergent ray
$S_{refraction}$	dimensionless amplitude of the refraction for the emergent ray
$S_j^{(p)}$	dimensionless amplitude of the reflection and/or the refraction for the emergent ray of order p
t_1, t_2	Fresnel coefficients
U	component of electric vector (s·A·m^{-2})
x_0, y_0, z_0	coordinates of a point where the light ray impinging on the particle surface (m)
x_2, y_2, z_2	the coordinates of other point where the light ray impinging on the particle surface (m)
z	parameter for Airy integral
z_1	constant parameter (α_1=1.0874)

z_2	constant parameter (α_2=3.4668)

Greek symbols

α	dimensionless size parameter
$\boldsymbol{\alpha}$	surface current density (A·m^{-2})
α_1	constant parameter (α_1=1.0874)
α_2	constant parameter (α_2=3.4668)
Γ	Gamma function
δ_1', δ_2'	phase shifts due to total reflection for two polarized directions (rad)
δ_j	phase difference due to the length of optical path (rad)
Δ_a	error of equatorial diameter of droplet inverted from the corresponding generalized rainbow patterns
Δ_m	error of refractive index of droplet inverted from the corresponding generalized rainbow patterns
$\Delta\theta_{rg}$	deviation angle between the geometrical rainbow angle for an ellipse and that for a sphere (^{o})
ε	permittivity (A^2·s^4·kg^{-1}·m^{-3})
ε_1, ε_2	infinitesimal shift amounts in x' and y' directions respectively
ε_j	fraction of the scattering intensity due to the reflection and/or the refraction for the emergent ray of order p
ζ_j	phase difference due to focal line (rad)
η	absorption coefficient
θ	scattering angle (^{o})
	off-axis angle (^{o})
θ_1, θ_2	angles of the first two peaks of the Airy simulation (^{o})
	angles of the first two peaks of the filtered intensity distribution (^{o})
θ_b	Brewster angle (^{o})
θ_c	critical angle (^{o})
ϑ_{gn}	rainbow angle for an ellipse in the sense of geometric optics (^{o})
θ_i	incident angle (^{o})

θ_{irg} , θ_{rrg}	incident angle and refractive angle for rainbow ray (^{o})
$\theta_{p}^{'}$	angle of deflection (^{o})
θ_{p}	angle of deflection (^{o})
θ_{psa}	polarization scattering angle (^{o})
θ_{r}	refractive angle (^{o})
θ_{rg}	scattering angle for the first rainbow (^{o})
ϑ_{r0}	the corresponding incident angle of the rainbow ray (^{o})
θ_{t}	refractive angle (^{o})
λ	wavelength of the incident light in the medium (m)
	wavelength of acoustic wave
μ	magnetic permeability (kg·m·s^{-2}·A^{-2})
v_{2}	velocity of light in a medium (m/s)
$\xi_{n}^{(2)}$	Riccati-Bessel function
π_{n}	function of scattering angle
ρ	eccentricity of the elliptical profile
p_{f}	free charge density (s·A·m^{-3})
σ	specific conductivity (kg·m^{2}·s^{-3}·A^{-2}·m)
σ_{j}	total phase shifts for the perpendicularly and parallel polarized directions of light ray (rad)
τ	charge density on the surface density (A/m^{2})
τ_{n}	function of scattering angle
φ	tilt angle of tilted droplet (^{o})
ϕ	elevation angle (^{o})
ϕ_{fp}	phase shift due to the focal point (rad)
ψ	oblique angle of incident light ray with respect to the major axis of spheroid (^{o})
ψ_{n}	Riccati-Bessel function
ω	angular frequency of the light (s^{-1})

Abbreviations

EBCM	extended boundary condition method
FLMT	Fourier-Lorenz Mie Theory
CCD	charged-coupled device
GLMT	generalized Lorenz-Mie theory
GO	geometrical optics
GRP	generalized rainbow pattern
HU	hyperbolic umbilic
HUFS	hyperbolic umbilic focal section
ILIDS	interferometric laser imaging for droplet sizing
IPI	interferometric particle imaging
LED	light-emitting diode
LMT	Lorenz-Mie theory
VRT	vector ray tracing

Chapter 1 Introduction

1.1 Development of particle optical diagnostic techniques

This research is devoted to basic light scattering computations and experiments for non-spherical particles, as they are often encountered in a wide variety of applications and in nature. Such a basic understanding of the light scattering features of particles lays the foundation for extending existing measurement techniques or devising novel techniques for particle characterisation, required for diagnostic purposes in research and development. Typical applications where such diagnostic techniques are indispensable include fuel injection in combustion chambers, spray cooling, spray coating, chemical engineering or cloud physics. Optical techniques are clearly advantageous over sampling, because of their non-intrusiveness and immediacy of results. Such droplet characterization of interest include refractive index, size, shape, orientation, velocity, and especially as well as for evaluating errors arising from the spherical shape assumption by many scattering-based measurement techniques.

The present work is restricted to spheroidal shapes and indeed to droplets, for which the scattering problem is defined by the aspect ratio (ratio of major to minor axes), refractive index and orientation with respect to the incident beam. At this stage the orientation angle will be fixed to 0°, but first results are available for particles tilted out of plane.

According to a recent review (Tropea, 2011), optical particle characterization techniques are classified as direct imaging, intensity or intensity ratio, interferometry, time shift, pulse delay and Raman scattering, according to measurement principles. A brief review of existing optical techniques for particle characterisation reveals that few are candidates for non-spherical particle shapes (Damaschke, et al., 1998). The most prominent and widely used techniques include the phase Doppler technique (Albrecht, et al., 2003), in which the measurability and measurement accuracy are affected by the non-sphericity of the particle (Damaschke, et al., 1998). Interferometric particle imaging (IPI) or interferometric laser imaging for droplet sizing (ILIDS) is a planar technique for sizing of spherical droplets (Maeda, et al., 2000), but is equally sensitive to non-sphericity as the phase Doppler technique. The time-shift technique (also known as the pulse-displacement technique), first introduced by Semidetnov (Semidetnov, 1985), holds significant potential for characterising non-spherical

droplets (Damaschke, et al., 2002), but has yet to be introduced as a commercial instrument (Schäfer, et al., 2012).

The primary rainbow has also been used previously for particle characterisation, for instance for size and temperature (refractive index) (Roth, et al., 1988). The measurement accuracy of the rainbow technique is also affected by the non-sphericity of droplets (van Beeck, et al., 1996); however with the global rainbow technique, both the droplet size distribution and average temperature can be estimated locally in a spray ((van Beeck, et al., 1999), (van Beeck, et al., 2001), (Vetrano, et al., 2004), and (Saengkaew, et al., 2009)). It is assumed that the non-spherical droplets and liquid ligaments provide a uniform background; hence they do not influence the interference pattern from which droplets size and temperature are derived. Nonetheless, none of the above methods are readily available for droplet non-sphericity measurements.

For further advancement and improvement of these optical techniques, the interpretion of light scattering from a droplet is a pre-requisite. Lorenz-Mie Theory ((Mie, 1908) and (Lorenz, 1890)) provides a rigorous solution to describe the scattering of a linearly polarized plane wave by a homogeneous sphere. Debye (Debye, 1909) interpreted the scattered light from a cylinder in terms of different orders. To describe the interaction between an arbitrarily shaped beam and a sphere, the Generalized Lorenz-Mie theory has been developed ((Gouesbet, et al., 1988) and (Gouesbet, 1994)).

On the other hand, many particles of interest are non-spherical particles. To calculate the light scattering from non-spherical particles, the separation of variables approaches (e.g. spheroidal expansion), surface based methods (e.g. T matrix method), volume-based methods (e.g. finite difference time domain), etc. have been developed (Wriedt, 1998). Most notably, Debye series for light scattering by a non-spherical particle with arbitrary shape has been studied (Xu, et al., 2010). Due to its intuitive physical interpretation, Debye series has been widely untilized by other researchers ((Lock, et al., 1994), (Wu, et al., 2008), (Shen, et al., 2010), and (Xu, et al., 2010)). However, the computation of the light scattering from non-spherical particles using these approach is only valid for very small particles (Ren, et al., 2011). For larger particles, light scattering can be approximately computed by geometrical optics ((van de Hulst, 1981) (Glantschnig, et al., 1981) (Xu, et al., 2004), (Lugovtsov, et al., 2007), and (Yu, et al., 2009)). The physical optical approximation was also proposed ((Ravey, et al., 1982), (Mazeron, et al., 1996), and (Onofri, et al., 2012)). Light scattering for bubbles

in liquid also has been studied based on physical-optics approximation (Marston, et al., 1982) and geometrical optics (Yu, et al., 2008).

Considering these difficulties in computing the light scattering from non-spherical particles, it is instructive to observe the scattering patterns experimentally. A variety of characteristic diffraction patterns from spheroidal droplets have been observed in the vicinity of the primary rainbow region (Marston, et al., 1984). The diffraction patterns, also known as generalized rainbow patterns, start from being a fold rainbow, then change to transverse cusp caustics and then to hyperbolic umbilic caustics as the axes ratio (major to minor) gradually increases ((Nye, 1992), (Marston, 1999), and (Lock, et al., 2010)). When the particle is spherical, the standard rainbow patterns are observed. To visually understand the patterns, this dissertation starts with the rainbow in nature and the laboratory.

1.2   Rainbows in nature and the laboratory

Rainbows have long been a source of inspiration both for poets and scientists who would prefer to treat them impressionistically or mathematically. People were historically attracted and puzzled by the following questions: What makes colors in the rainbows? Why the sequences of colors reverse in the higher bows? If there can be two rainbows, why not more? The classical Greek scholar Aristotle (384-322 BC) was the first to devote serious attention to the rainbow. The attraction to this phenomenon of Descartes, Newton, Yong, Airy and others, has resulted in the formulation and test of some of the most fundamental principles of mathematical physics (Nussenzveig, 1977). Most notably, Theodoric of Freiberg (1250-1310) provided an accurate explanation of the colors and positions of the primary and secondary rainbows (Edward, 1974). Now it is clear that the rainbow is an optical and meteorological phenomenon and the primary rainbow arises from the second-order refraction of light from the water droplets in the earth's atmosphere, resulting in a multicolored arc in the sky.

The primary rainbow photographed after a rainstorm is shown in Fig. 1.1, which is the rainbow most commonly known and observed. The rainbow caused by sunlight always appears in the section of the sky directly opposite to the sun. And the colors of the primary rainbow are always followed the sequence: violet is innermost, blending gradually with various shades of blue, green, yellow and orange, with red outermost. Under favourable conditions one can also see a double rainbow in the sky (see Fig. 1.4 in ref. (van Beeck,

1997)). In this case, higher in the sky than the primary arc is the secondary one, which is faint and indeed not always present. In the second rainbow, the colors appear in reverse order. Careful observation reveals that the region between the two bows is considerably darker than the surrounding sky. The dark region has been given the name Alexander's dark band after the Greek philosopher Alexander who first described it in about A. D. 200 (Nussenzveig, 1977).

Rainbows could be caused by many forms of airborne water. These include not only rain, but also mist, spray, and airborne dew. For example, the rainbow effect is also commonly seen near waterfalls or fountains. In most cases, we only see the semicircle when we are on the ground. Exceptions can occur when the observer is high above the ground, for example in an aeroplane or on top of a mountain. Then one can see the entire circle of the rainbow, with the observer's shadow in the center.

Fig. 1.1.   The primary rainbow in the sky (photographed at Darmstadt on 8th August 2011).
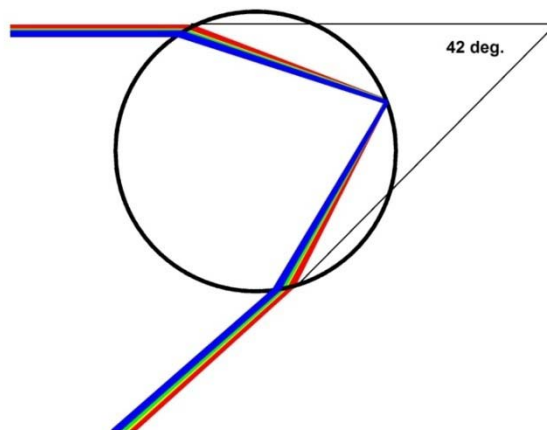

Fig.1.2.   Dispersion of white light into different colors on entering and leaving water droplet.

A more detailed explanation of formation of rainbow is given in following. The light is first refracted entering the surface of the rain droplet, reflected off the back of the droplet, and again refracted leaving the droplet (see Fig. 1.2.) In conventional use, the scattering angle can be defined by the deviation angle of the exiting light ray from the incidence direction. According to geometrical optics, the scattering angle exhibits a minimal value, which is called the rainbow angle and denoted by ϑ_{rg}, independent of the size of the droplet, but dependent on relative refractive index of droplet, as will be discussed in detail in next Chapter. Consequently light rays are strongly scattered at an angle of about 138° for a water droplet. However, geometrical optics can only approximately determine the rainbow position. As is well known, white light is the effect of combining the visible colors of light with different wavelengths in suitable proportions. The relative refractive index is different for different wavelengths. So the rainbow angles are slightly different for each wavelength of light, with the result that the colors are dispersed, as shown in Fig. 1.2. Consequently, white light is separated into different colors on entering and leaving the rain droplet. Because red light is refracted by a lesser angle than blue light, when leaving the raindrop, the red light rays have turned through a smaller angle than the blue rays, producing the primary rainbow.

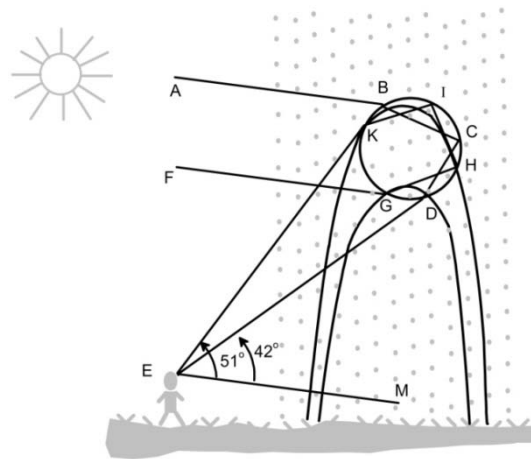Fig. 1.3.   Descartes' sketch of the rainbow formation.

So far, only interaction with a single droplet has been considered. Actually the rainbow arcs in the sky are caused by a large number of droplets. Descartes' sketch (see Fig. 1.3) reveals how the primary and secondary rainbows are formed (Han, 2000). In Descartes' sketch of rainbow, the rainbow angle is defined by the angle between the scattering light and the

direction opposite the sunlight. According to geometrical optics, the primary rainbow is formed by the ray ABCDE while the secondary rainbow is formed by the ray of FGHIKE. For the primary rainbow, the light rays encounter one inner reflection and two refractions and is located at the angle of 40°-42°. However, the secondary rainbow, which appears at the angle of 50°-53°, is caused by light rays undergoing two reflections inside the raindrop and two refractions. As a result of the second reflection, the colors of the second rainbow are inverted to the colors of the primary bow, with blue on the outside and red on the inside. And the second rainbow is much fainter than the primary rainbow because more light exits the drop at each of the two reflections compared to a single reflection. Furthermore, the second rainbow is spread over a great area of the sky. Therefore it is not always simultaneously present with the primary rainbow. While higher-order rainbows also exist, they are generally not visible to the observer. Many excellent textbooks and articles do exist on this subject, and the more detailed history and explanations of rainbow can be found ((Khare, et al., 1974), (Walker, 1977), (Nussenzveig, 1977), (Sassen, 1979), (Nussenzveig, 1979), (Wang, et al., 1991), (Lock, 1993), (van Beeck, 1997), and (Lee, 1998)).

Even though it is difficult to observe higher-order rainbows in nature, in the laboratory extremely bright and well collimated light produced by laser can be used to visualize these. It is reported that higher-order rainbows, up to 200th, formed by a pendant water drop, have been observed (Ng, et al., 1998). The higher-order rainbows have been studied theoretically and experimentally ((Lock, 1987) and (Ng, et al., 2007)). The significant difference of such rainbows to natural rainbows is that the light source is a laser beam and the origin is a single, spherical droplet. In the present study the scattering patterns from droplets which are deformed and non-spherical are studied.
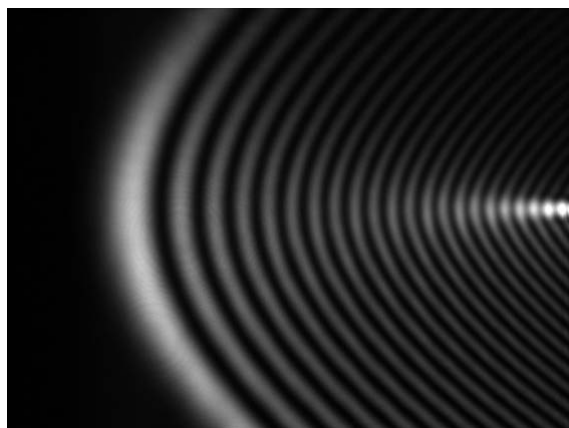
Fig. 1.4.　Generalized rainbow pattern from a spheroidal water droplet with aspect ratio of 1.21.

Considering the the difficulties in computation of the light scattering from large particles with complex shape, a simplified problem is to start from spheroidal particles. A variety of characteristic scattering patterns from spheroidal water droplets have been observed in the vicinity of the primary rainbow region (Marston, et al., 1984). These patterns are called diffraction patterns in the language of catastrophe optics (Berry, et al., 1980). The diffraction patterns, also known as generalized rainbow patterns, start from being a fold rainbow, then change to transverse cusp caustics and then to hyperbolic umbilic caustics as the aspect ratio gradually increases ((Nye, 1992) and (Marston, 1999)). A generalized rainbow pattern from a spheroid water droplet with aspect ratio of 1.21 is shown in Fig. 1.4. As the ratio is further increased, other catastrophes will appear. To understand more of the generalized rainbow patterns, one can refer the articles ((Berry, et al., 1980), (Nye, 1992), (Kaduchak, et al., 1994), (Kaduchak, et al., 1994), and (Marston, et al., 1994)). And the detailed explanation and more rainbow patterns will be given in Chapter 4.

1.3 Thesis overview

The development of new measurement techniques for non-spherical droplet characterization is the main subject of the thesis. The application of the optical characterization technique is the non-intrusive measurement of droplets and sprays in a numerous industrial processes e.g. painting, spray cooling, spray drying, inhalators, aerosol sprays, etc. It is based on the generalized rainbow patterns.

The light scattering theories including exact theories and approximation methods are given in Chapter 2. Lorenz-Mie theory (also known as Mie theory) is the solution to Maxwell's equation which can be used to describe the scattering of plane electromagnetic radiation by an optically homogeneous spherical particle. The solution takes the form of an analytical infinite series and is named after its developer Gustav Mie and Ludvig Lorenz who developed the theory independently. Debye series expansion is developed for scattering of light by a homogeneous particle which could interpret the scattered intensity in terms of various physical processes (Debye, 1909). However, these rigorous theories cannot be applied to particles of complex shape. Geometrical optics approximation is a very simple and intuitive

method for treating the interaction of a particle with light. The shape of the particle could be complex, but the size of particle must be much larger than the wavelength of the light. Moreover, the Airy approximation can be used to calculate the light scattering in the rainbow region.

In Chapter 3, vector ray tracing (VRT) model for spheroid is presented, which can be used both for a sphere and a particle with complex shape. For a given incident light ray, the calculation of the reflected ray, transmitted rays, and the intersection of the inside ray with the particle are given in detail. Some first simulation results are also given in this Chapter.

In Chapter 4, the VRT model is employed to simulate optical caustic structures including the rainbow and hyperbolic umbilic (HU) fringes in the primary rainbow region of light scattering from oblate water droplets. The location of cusp caustics are calculated by VRT and compared to results obtained using an analytic solution, in which a good agreement is found. The evolution of the optical caustic structures in response to shape deformation of oblate water droplets is investigated using the VRT method and is found to be consistent with experimental observation. For the secondary rainbow, the location of the cusp caustic is also calculated using the VRT method and compared with that calculated using analytic solutions; again excellent agreement is found. The optical caustic structures for the secondary rainbow are first simulated and analyzed systematically according to VRT model and the evolution process of the optical caustic structures is consistent with experimental observations.

Then, the experimental investigation of light scattering by oblate spheroidal particle in the primary rainbow region is shown in Chapter 5. The generalized rainbow patterns are presented and discussed in detail. By comparison of experimental results with Airy approximation, the validity of the Airy approximation for spheroidal droplets is confirmed.

In Chapter 6, based on the generalized rainbow patterns and Airy approximation, the refractive index and equatorial diameter of spheroidal water droplets are determined. It is shown that absolute error of the refractive index is less than 0.5×10^{-4} and of the droplet diameter 5%. Furthermore, the relation between the curvature of the rainbow fringes and the aspect ratio of spheroidal water droplets is established. Then the aspect ratio of spheroidal droplets is inferred from the corresponding generalized rainbow patterns with relative errors lying between -1% and 1%.

Then, the evolution of the optical caustic structures for tilted spheroidal droplets is given in Chapter 7. The rainbow fringes are counterclockwise tilted as the spheroidal droplet is

counterclockwise tilted and vice versa. The experimental investigation for a tilted spheroidal droplet is also presented.

In Chapter 8, Möbius's approximation is modified to calculate the deviation between the geometrical rainbow angle for an ellipse and that for a sphere. And the vector ray tracing model is also used to compute the rainbow angle deviation for an ellipse, which agrees with modified Möbius equation for small eccentricity. Moreover, the application range of Möbius's approximation is also investigated. It is demonstrated that, for small eccentricity, that is, 0.95≤a/c ≤1.05, the Möbius's approximation can be used to predict the rainbow angle deviation of an ellipse.

Finally, the dissertation is concluded with a conclusion and perspectives section in Chapter 9.

Chapter 2 Light Scattering Theories

In this Chapter, an introduction of light and Maxwell's equations are given. Then the analytical solution of interaction of light with a particle is introduced, which includes the Lorenz-Mie theory and Debye series. The approximation methods of light scattering from a particle, including geometrical optics approximation and Airy approximation, are then reviewed. Furthermore, the polarization character of light scattered in the rainbow region is studied based on geometrical optics.

2.1 Introduction to light

In physics, the term light refers to electromagnetic radiation of any wavelength, whether visible or not. Commonly, light is referred to electromagnetic radiation that is visible to the human eye and is responsible to the sense of sight. Primary properties of light are intensity, propagation direction, frequency or wavelength spectrum, and polarization, while its speed in vacuum is one of the fundamental constants of nature.

J. C. Maxwell was first to formally postulate electromagnetic waves. Maxwell's equations are a set of partial differential equations that, together with Lorentz force law, form the foundation of classical electrodynamics and classical optics. The electromagnetic field comprises the mutually perpendicular electric field **E** and magnetic field **H**. According to Maxwell's equations, a specially varying electric field causes the magnetic field to change over time. Likewise, a spatially varying magnetic field causes changes over time in the electric field. The electromagnetic field (**E**, **H**) satisfies Maxwell's equations given in the following form (Born, et al., 1999):

$$\nabla \cdot \mathbf{E} = \frac{\rho_f}{\varepsilon}, \qquad \nabla \times \mathbf{E} = -\mu \frac{\partial \mathbf{H}}{\partial t},$$

$$\nabla \cdot \mathbf{H} = 0, \qquad \nabla \times \mathbf{H} = \sigma \mathbf{E} + \varepsilon \frac{\partial \mathbf{E}}{\partial t}. \tag{2.1}$$

Where $\nabla \cdot$ is the divergence operator, $\nabla \times$ is the curl operator, p_f is called free charge density, σ is called the specific conductivity, ε is known as permittivity and μ is the magnetic permeability.

To allow a unique solution of the field vectors from a given distribution of currents and charges, the above equations must be supplemented by relations, which can describe the

behavior of substances under the influence of the field. These relations are known as material equations. Generally, for linear materials the material equations are:

$$\mathbf{D}=\varepsilon\mathbf{E}, \qquad \mathbf{B}=\mu\mathbf{H}, \qquad \mathbf{J}_f=\sigma\mathbf{E}. \tag{2.2}$$

here $\mathbf{D}$ is the electric displacement, $\mathbf{B}$ the magnetic induction and $\mathbf{J}_f$ the electric current density.

To apply the material equation to Eq. (2.1), one can rewrite Maxwell equation in the following form:

$$\nabla\cdot\mathbf{D}=\rho_f, \quad \nabla\times\mathbf{E}=-\frac{\partial\mathbf{B}}{\partial t},$$
$$\nabla\cdot\mathbf{B}=0, \quad \nabla\times\mathbf{H}=\mathbf{J}_f+\frac{\partial\mathbf{D}}{\partial t}. \tag{2.3}$$

In vacuum, the free charge density and electric current density are both zero, and the above equation can be simplified.

To solve Maxwell's equations, one can deduce other differential equations in which each of the vectors separately satisfies. These are called wave equations. For an optically homogeneous medium, the wave equations are given as:

$$\nabla^2\mathbf{E}-\mu\varepsilon\frac{\partial^2\mathbf{E}}{\partial t^2}-\mu\sigma\frac{\partial\mathbf{E}}{\partial t}=0,$$
$$\nabla^2\mathbf{H}-\mu\varepsilon\frac{\partial^2\mathbf{H}}{\partial t^2}-\mu\sigma\frac{\partial\mathbf{H}}{\partial t}=0. \tag{2.4}$$

The wave equations can be written in other forms which depend on the units adopted (Born, et al., 1999). Attention has to be paid to the fact that, while Maxwell's equations are extraordinarily successful at explaining and predicting variety phenomena, they are not exact. In some situations e.g. strong fields and extremely short distances, they are not accurate. For more accurate predictions, Maxwell's equations are superseded by quantum electrodynamics, which is beyond the scope of this dissertation.

On other hand, Maxwell's equations (Eqs. (2.1) and (2.3)) are only stated for regions of space in which the physical properties of the medium are continuous. In most case, one often deals with situations in which the properties change abruptly across one or more surfaces. The electromagnetic vectors $\mathbf{E}$, $\mathbf{D}$, $\mathbf{H}$, and $\mathbf{B}$ may then become discontinuous; however they must obey the boundary conditions at a surface of discontinuity:

$$\mathbf{n}\cdot(\mathbf{D}_2-\mathbf{D}_1)=\tau, \quad \mathbf{n}\times(\mathbf{E}_2-\mathbf{E}_1)=0. \tag{2.5a}$$

$$\mathbf{n}\cdot(\mathbf{B}_2-\mathbf{B}_1)=0, \quad \mathbf{n}\times(\mathbf{H}_2-\mathbf{H}_1)=\alpha. \tag{2.5b}$$

Here **n** is the unit normal pointing from the first medium into the second medium, τ is the charge density on the surface and **α** is the surface current density.

For convenience of operation and theoretical analysis, the field of the light can be represented by the complex amplitude, which is an indispensable tool in the mathematical physics of wave phenomena:

$$U(\mathbf{r},t) = A(\mathbf{r})\exp\left[i(\omega t - \mathbf{k}\cdot\mathbf{r})\right] \tag{2.6}$$

where $A(\mathbf{r})$ is the amplitude function related to the location $\mathbf{r}$, $\mathbf{k}$ the wave number which can be complex in absorbing medium, ω the angular frequency or called circular frequency. The choice of i or $-i$ is arbitrary. The present choice of positive i in the time factor is the classical one and corresponds with the classical form of the complex refractive index (van de Hulst, 1981).

According to the set of $\exp(i\omega t - i\mathbf{k}\cdot\mathbf{r})$, $-i$ is the imaginary unit of $\sqrt{-1}$. Only on this assumption, the transmission wave corresponds to the physical situation, otherwise the amplitude would tend to infinity with increasing distance, under the condition of total reflection occurs (Yu, 2008). Contrary to the present choice, $\sqrt{-1} = i$ is adopted in Born's description (Born, et al., 1999). In the present choice, the phase advances by $\pi/2$ at the passage of any focal point (also called focal line) (van de Hulst, 1981). The complex refractive index for an absorbing medium is defined as $n_2 = n(1-i\eta)$, where n and η are positive, and η is the so-called absorption coefficient. However, if one adopt the other choice of $\exp(-i\omega t + i\mathbf{k}\cdot\mathbf{r})$, $\sqrt{-1}$ equals i, the phase shift is $-\pi/2$ when the light passes the focal point, and the complex refractive index is $n_2 = n(1+i\eta)$. In summary:

$$\begin{cases} \sqrt{-1} = -i, & \phi_{fp} = \pi/2, & n_2 = n(1-i\eta), & for \exp(i\omega t - i\mathbf{k}\cdot\mathbf{r}), \\ \sqrt{-1} = i, & \phi_{fp} = -\pi/2, & n_2 = n(1+i\eta), & for \exp(-i\omega t + i\mathbf{k}\cdot\mathbf{r}). \end{cases} \tag{2.7}$$

here ϕ_{fp} is the phase shift due to the focal point. The present choice is i, which is retained throughout this dissertation. So the time shift is $\pi/2$ at passage of any focal point, and imaginary part of refractive index is negative.

2.2 Rigorous theories of light scattering

Light scattering theory is a framework for studying and understanding the scattering of light by particles. The particles could be atoms, molecules, particulate particle, liquid droplets, etc. One kind of light scattering is inelastic light scattering in which the frequency of scattered

light is shifted. A well-known inelastic light scattering is Raman scattering, which is widely used for material identification and analysis (Kador, et al., 2003), and medicine (Choo-Smith, et al., 2002). The other kind of light scattering is elastic light scattering, such as Rayleigh scattering and Mie scattering, in which the frequency of scattered light is not changed. The present work focuses on elastic light scattering and its application to particle characterization.

Light scattering theory is the solution of Maxwell's equations describing the interaction of electromagnetic field and particles, which are given in Chapter 2.1. The electromagnetic field can be plane wave, Gaussian beam and the particle shape could be arbitrary. However, only for some regular particles including sphere, spheroid, ellipsoid or cylinder, can an analytical solution be obtained. Lorenz-Mie theory is the solution to Maxwell's equations describing the scattering of plane electromagnetic radiation by spherical particle. Generalized Lorenz-Mie theory describes the interaction of a homogeneous sphere and electromagnetic radiation with an arbitrary shaped beam. Debye series expansion is developed for the light scattering by a homogeneous particle to interpret the scattered intensity in terms of various physical processes.

2.2.1 Lorenz-Mie theory
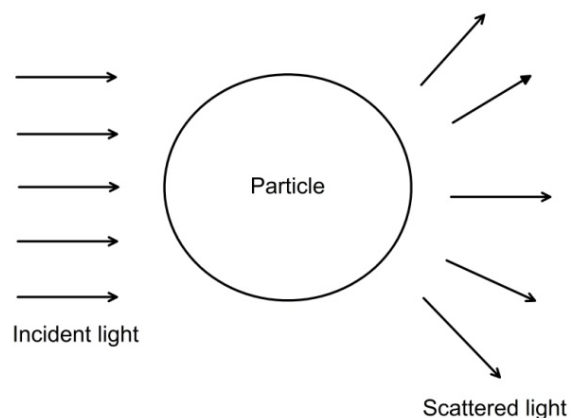

Fig 2.1.   Light scattering model.

In 1908, Gustav Mie published his famous paper for explaining the color effects related with colloidal gold particles (Mie, 1908). In this paper, he gave an outline of how to calculate the light scattering by small spherical particles using Maxwell's electromagnetic theory. Although electromagnetic scattering by a homogeneous, isotropic sphere is commonly

referred to as Mie theory, Gustav Mie was not the first to formulate this electromagnetic scattering problem. Before him, Ludvig Lorenz also contributed to this problem (Lorenz, 1890). Therefore, plane wave scattering by homogeneous spherical particle is also referred to as Lorenz-Mie theory. For more detailed introductions to Lorenz-Mie theory, one can refer to the book (Hergert, et al., 2012).

Lorenz-Mie theory is the solution to Maxwell's equations describing the scattering of electromagnetic radiation by homogeneous spherical particle (see Fig. 2.1). The solution takes form of two amplitude functions $S_1(\alpha,m,\vartheta)$ and $S_2(\alpha,m,\vartheta)$. They are the non-dimensional scattering amplitudes perpendicular and parallel to the scattering plane respectively, and are given as:

$$S_1(\alpha,m,\theta) = \sum_{n=1}^{\infty} \frac{2n+1}{n(n+1)} \left[a_n(\alpha,m)\pi_n(\cos\theta) + b_n(\alpha,m)\tau_n(\cos\theta) \right] \qquad (2.8)$$

$$S_2(\alpha,m,\theta) = \sum_{n=1}^{\infty} \frac{2n+1}{n(n+1)} \left[a_n(\alpha,m)\tau_n(\cos\theta) + b_n(\alpha,m)\pi_n(\cos\theta) \right] \qquad (2.9)$$

Here a_n and b_n are the Mie coefficients, τ_n and π_n are the Legendre functions, which are given by:

$$a_n = \frac{\psi_n(\alpha)\psi_n'(m\alpha) - m\psi_n'(\alpha)\psi_n(m\alpha)}{\xi_n^{(2)}(\alpha)\psi_n'(m\alpha) - m\xi_n^{(2)'}\psi_n(m\alpha)} \qquad (2.10)$$

$$b_n = \frac{m\psi_n(\alpha)\psi_n'(m\alpha) - \psi_n'(\alpha)\psi_n(m\alpha)}{m\xi_n^{(2)}(\alpha)\psi_n'(m\alpha) - \xi_n^{(2)'}\psi_n(m\alpha)} \qquad (2.11)$$

$$\pi_n(\theta) = \frac{P_n^{(1)}(\cos\theta)}{\sin\theta} = \frac{dP_n(\cos\theta)}{d\cos\theta} \qquad (2.12)$$

$$\tau_n(\theta) = \frac{dP_n^{(1)}(\cos\theta)}{d\theta} \qquad (2.13)$$

where the relative refractive index $m = m_2/m_1$ is the ratio of the refractive index of the particle m_2 to the that of ambient medium m_1, and $\alpha = 2\pi a/\lambda$ is the dimensionless particle size parameter (Mie parameter), where a is the radius of spherical particle and λ the wavelength of the incident light in the ambient medium. $P_n^{(1)}(\cos\theta)$ is the associated Legendre function.

$\psi_n(\alpha)$ and $\xi_n^{(2)}(\alpha)$ are the Riccati-Bessel functions given by:

$$\psi_n(\alpha) = \left(\frac{\pi\alpha}{2} \right)^{1/2} J_{n+\frac{1}{2}}(\alpha) \qquad (2.14)$$

$$\xi_n^{(2)}(\alpha) = \left(\frac{\pi\alpha}{2}\right)^{1/2} H_{n+\frac{1}{2}}^{(2)}(\alpha) \tag{2.15}$$

here $J_{n+\frac{1}{2}}(\alpha)$ is the Bessel function of the first kind, and $H_{n+\frac{1}{2}}^{(2)}(\alpha)$ is the Hankel function of the second kind. The Hankel function of the second kind is used, because it makes $\mathbf{E}\exp\left[i(\omega t - \mathbf{k}\cdot\mathbf{r})\right]$ to an outgoing wave at larger distance from the particle, as the scattered wave is supposed to be. The Hankel function of the first kind can be used if one adopt the convention of $\mathbf{E}\exp(-i\omega t + i\mathbf{k}\cdot\mathbf{r})$.

Usually, the detection of the scattered light takes place at a very larger distance from the particle, that is, the far-field approximation (Hergert, et al., 2012). The scattered amplitudes for the two polarized directions are respectively:

$$E_1 = \frac{i\lambda}{2\pi r} S_1(\theta) E_{10} \tag{2.16}$$

$$E_2 = \frac{i\lambda}{2\pi r} S_2(\theta) E_{20} \tag{2.17}$$

Here r is the distance from the particle center to the observer. E_{10} and E_{20} are incident electric field components of two polarized directions, respectively.

Generally, the normalized far-field intensities $i_1(\alpha,m,\theta)$ and $i_2(\alpha,m,\theta)$ are used, which are given by:

$$i_1(\alpha,m,\theta) = \left|S_1(\alpha,m,\theta)\right|^2 \tag{2.18}$$

$$i_2(\alpha,m,\theta) = \left|S_2(\alpha,m,\theta)\right|^2 \tag{2.19}$$

The intensity of un-polarized scattered light $i(\alpha,m,\theta)$ is simply obtained by averaging the intensity due to the two linearly polarized components, i.e.

$$i(\alpha,m,\theta) = \frac{i_1(\alpha,m,\theta) + i_2(\alpha,m,\theta)}{2} \tag{2.20}$$

It can be seen that the scattering amplitudes (S_1 and S_2) given by Eqs. (2.8) and (2.9) are expressed in terms of an analytical infinite series. For simulation, the criterion of the terminating order must be chosen. For $\alpha \in (0,100000)$, a criterion is given by the following equation (Shen, et al., 2005).

$$n_{stop} = \begin{cases} \alpha + 7.5\alpha^{0.34} + 2 & |A_n(\alpha)| < 1e-18, \\ \alpha + 6\alpha^{1/3} + 2 & |A_n(\alpha)| < 1e-12, \\ \alpha + 4.88\alpha^{0.31} & |A_n(\alpha)| < 1e-5. \end{cases}$$
(2.21)

Lorenz-Mie theory gives the analytical solution of the interaction between electromagnetic radiation and the homogeneous spherical particle. Due to the development of computation, it can be used to simulation of the scattered light from larger size particle. However, it does not give insight into either the scattering process, or changes in the pattern resulting from changes in shape, refractive index, or profile of the incident wave fronts.

2.2.2 Debye series expansion

The analytical solution of the interaction between electromagnetic radiation and the homogeneous spherical particle is given by Lorenz-Mie theory. For a homogeneous spheroidal particle, the solution of electromagnetic scattering has also been obtained ((Asano, et al., 1975), (Asano, 1979), and (Asano, et al., 1980)). However, only a plane and linearly polarized monochromatic wave was considered in the above cases. For shaped-beam incidence, the generalized Lorenz-Mie theory (GLMT) was developed ((Gouesbet, et al., 1988), (Gouesbet, 1994), (Barton, 1995), (Han, et al., 2001), (Xu, et al., 2007), and (Lock, et al., 2009)). Alternatively the Fourier-Lorenz Mie Theory (FLMT) can also be used to compute the scattering of shaped beams from spherical particles (Albrecht, et al., 2003).

Although LMT, FLMT and GLMT provide accurate solutions to the Maxwell equations, the drawbacks lie in the fact that they cannot reveal the contribution of different scattering orders to the overall scattering pattern. Debye series provides such information and has been applied to some regular particles (e.g. cylinder (Debye, 1909), sphere (Nussenzveig, 1969), coated sphere (Lock, et al., 1994), and multilayer cylinder (Wu, et al., 2008) etc.). However Debye series has not yet to be applied to spheroidal particles or particles with complex shape. The difficulties in doing so are, on the one hand, that the orthogonality relationship of the spheroidal vector wave functions does not exist, which is a prerequisite for the Debye series in analytical form for each order n. On the other hand, the second kind of spheroidal radial function for spheroids of large size or large axis ratio exhibit numerical divergence.

Recently, the Debye series has been developed for light scattering by spheroidal particles in order to decompose the far-zone fields into various physical processes (Xu, et al., 2010).

Furthermore, the Debye series has been applied to analyze the formation of rainbow caustic, transverse cusp and hyperbolic umbilic caustics for a spheroid, which provides an exact analysis tool for studying the light scattering by a spheroid (Lock, et al., 2010). The Debye series is also generalized to nonspherical particles with complex shape (Xu, et al., 2010) and coated nonspherical particles (Xu, et al., 2010) using the extended boundary condition method (EBCM). The EBCM treats light scattering in spherical coordinates independent of the shape of the particle's surface; no special coordinate system in which the vector wave equation is separable is required to match the boundary conditions of the electromagnetic field at the particle surface

However, Debye series has not been applied to droplet sizes of hundreds of microns because of the numerical problems in computation. Accordingly, further investigations for applying Debye series for large particle needs to be implemented.

2.3 Approximation methods

Although rigorous theories cannot be applied to larger particles, the geometrical optics approximation is a very simple and intuitive method for such cases. The particle shape can be complex, but the size of the particle must be much larger than the wavelength of the light. Moreover, the Airy approximation can be used to calculate the light scattering in the rainbow region.

Other approximation methods for the light scattering problems, such as the complex angular momentum method or the physical-optics approximation are available; however, only the geometrical optics approximation and Airy approximation are introduced and only the basic principles are presented without a detailed derivation.

2.3.1 Geometrical optical approximation

The geometrical optics approximation and its generalizations provide solutions to electromagnetic problems that are valid in the limit of large dimensionless size parameter (i.e. the ratio of particle size to the light wavelength). The most appealing factors of the geometrical optics approximation are their simplicity and intuitive nature. Since many excellent textbooks (van de Hulst, 1981)and articles ((Lock, 1996), (Lock, 1996), (Xu, et al., 2004), (Xu, et al., 2006), (Xu, et al., 2006), (Yu, et al., 2008) and (Yu, et al., 2009) etc.) exist on the subject, the present thesis shall only survey the basic principles, providing the most significant working relations.

From the geometrical optics viewpoint, the amplitude of the scattered light can be calculated by the superposition of reflection, refraction and diffraction rays.

$$S(a,b,\theta,\phi) = S_{diffraction} + S_{reflection} + \sum_{p=1}^{\infty} S_{refraction} \tag{2.22}$$
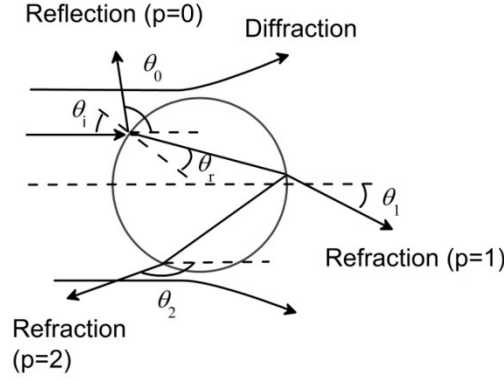

Fig. 2.2. Theoretical model of geometrical optics approximation.

Figure 2.2 shows the light scattered by a sphere in the geometrical optics sense, assuming that all the incident light rays are parallel, that is, the incident light is a plane wave. A light ray impinging on the sphere at an incident angle ϑ_i is partly reflected and partly refracted, with the exception of total reflection. At all subsequent interfaces this process repeats with the result that an infinite number of rays emerge from the scatterer for each particular incident ray. Each emerging ray can be characterized by the incident angle ϑ_i and the integer p, denoting the number of chords each light ray makes inside the sphere. The deflection angle θ'_p between the pth emerging ray which can be reflection ray of refraction ray, and the direction of incident light ray can be expressed as follows (Yu, 2008):

$$\theta'_p(m,\theta_i) = 2p\theta_r - 2\theta_i - (p-1)\pi \quad p = 0,1,2,3 \cdots \tag{2.23}$$

where θ_r the refraction angle. And by the Snell's law $\sin\vartheta_i = m\sin\vartheta_r$. The $p=0$ ray represents the externally reflected light. The $p=1$ ray is directly transmitted through the sphere without any internal reflection and the ray is transmitted with p-1 internal reflections when $p>1$. To simplify the problem, the scattering angle θ is defined, which is related to the deflection angle.

$$\theta'_p(m,\theta_i) = -2\pi l + q\theta \tag{2.24}$$

25

where q=1 or -1, and $\theta \in (0,\pi)$. l is an integer which must be chosen so that the scattering angle θ is on the range of $(0,\pi)$. q=1 indicates that the incident light ray hits the sphere on the top hemisphere and q=-1 for the lower hemisphere (Yu, et al., 2008).

The scattering intensity of a finite emergent pencil of light is given by (van de Hulst, 1981):

$$I_j^{(p)}(p,m,\theta_i) = \frac{\varepsilon_j^2 I_0 a^2 \sin\theta_i \cos\theta_i d\theta_i d\varphi}{r^2 \sin\theta d\theta d\varphi} = \frac{a^2}{r^2} I_0 \varepsilon_j^2 D^{(p)}(p,m,\theta_i), \quad j=1,2 \qquad (2.25)$$

where the subscript j=1 is for the perpendicular polarization component and j=2 for the parallel polarization component of light with respect to the scattering plane, and

$$D^{(p)}(p,m,\theta_i) = \frac{\sin\theta_i \cos\theta_i}{\sin\theta |d\theta_p^{'}(\theta_i)/d\theta_i|} = \frac{\sin\theta_i \cos\theta_i}{\sin\theta} \times \left| \frac{(m^2 - \sin^2\theta_i)^{1/2}}{2\left[p\cos\theta_i - (m^2 - \sin^2\theta_i)^{1/2}\right]} \right| \qquad (2.26)$$

is the so-called divergence or convergence factor.

The divergence given in Eq. (2.26) can be infinite when $d\theta_p^{'}(\theta_i)/d\theta_i = 0$. Combining Eq. (2.23) with the Snell's law, after some algebra, one can obtain:

$$\left| \frac{d\theta_p^{'}(\theta_i)}{d\theta_i} \right| = 2\left| \frac{p\cos\theta_i}{m\cos\theta_r} - 1 \right| = 0 \qquad (2.27)$$

To apply the Snell's law to Eq. (2.27), one can obtain

$$\sin\theta_i = \sqrt{(p^2 - m^2)/(p^2 - 1)}, \qquad \theta_i = \sin^{-1}\sqrt{(p^2 - m^2)/(p^2 - 1)},$$
$$\sin\theta_r = \sqrt{(p^2 - m^2)/m^2(p^2 - 1)}, \qquad \theta_r = \sin^{-1}\sqrt{(p^2 - m^2)/m^2(p^2 - 1)}. \qquad (2.28)$$

By substituting Eq. (2.28) into Eq. (2.23), the scattering angle for the first rainbow (p=2) is given by:

$$\theta_{rg} = \pi + 2\sin^{-1}\sqrt{\frac{4-m^2}{3}} - 4\sin^{-1}\sqrt{\frac{4-m^2}{3m^2}} \qquad (2.29)$$

Therefore in geometrical optics, the rainbow angle is a function of relative refractive index. The relative refractive indices are 1.330 and 1.432 for red light and violet light (for a water scatterer in air) respectively. The rainbow angle is 137.5° for red light, but 139.38° for violet light.

The fraction ε_j in the scattering intensity is given as:

$$\begin{cases} \varepsilon_j = r_j & p = 0 \\ \varepsilon_j = (1 - r_j^2)(-r_j)^{(p-1)} & p = 1,2,3,\cdots \end{cases} \quad j = 1,2 \qquad (2.30)$$

where r_1 and r_2 are the Fresnel reflection coefficients (Born, et al., 1999) given by,

$$r_1 = \frac{\cos\theta_i - m\cos\theta_r}{\cos\theta_i + m\cos\theta_r}, \qquad r_2 = \frac{m\cos\theta_i - \cos\theta_r}{m\cos\theta_i + \cos\theta_r} \qquad (2.31)$$

For computation convenience, one can introduce at this point the dimensionless intensity $i_j^{(p)}(\alpha,m,\theta_i)$ defined as,

$$i_j^{(p)}(\alpha,m,\theta_i) = \alpha^2 \varepsilon_j^{\,2}(m,\theta_i) D^{(p)}(p,m,\theta_i) \qquad j=1,2 \qquad (2.32)$$

One can further define a corresponding amplitude function of scattering light for each polarization component by:

$$S_j^{(p)}(\alpha,m,\theta_i) = \alpha\varepsilon_j \left[D^{(p)}(p,m,\theta_i)\right]^{1/2} \exp\left[i(\delta_i + \zeta_i)\right] \qquad j=1,2 \qquad (2.33)$$

The phase δ_j due to the length of optical path and the phase ζ_j due to focal lines are given by (van de Hulst, 1981):

$$\begin{cases} \delta_j = 2\alpha\left(\cos\theta_i - pm\cos\theta_r\right) \\ \zeta_j = \frac{\pi}{2}\left(1 + p + 2l + \frac{1}{2}s - \frac{1}{2}q\right) \end{cases} \quad j=1,2 \qquad (2.34a)$$

where the integer p, l and q are defined above, and s denotes +1 or -1, on the contrary the sign of $d\theta'_p / d\theta_i$, i.e.

$$s = \begin{cases} 1 & for \quad \dfrac{p\cos\theta_i}{m\cos\theta_r} - 1 > 0, \\ -1 & for \quad \dfrac{p\cos\theta_i}{m\cos\theta_r} - 1 < 0. \end{cases} \qquad (2.34b)$$

To study the phase shift of reflection and refraction, the Fresnel formulae are given as follows:

$$\begin{aligned} r_1 &= \frac{\cos\theta_i - m\cos\theta_r}{\cos\theta_i + m\cos\theta_r}, & t_1 &= \frac{2\cos\theta_i}{\cos\theta_i + m\cos\theta_r} \\ r_2 &= \frac{m\cos\theta_i - \cos\theta_r}{m\cos\theta_i + \cos\theta_r}, & t_2 &= \frac{2\cos\theta_i}{m\cos\theta_i + \cos\theta_r} \end{aligned} \qquad (2.35)$$

The Fresnel coefficients as a function of incident angle are shown in Fig. 2.3. One can see the refraction coefficients t_1 and t_2 are always positive. The reflection coefficient r_1 is always negative, but the sign of reflection coefficient r_2 changes from positive to negative as the incident angle increase. This special angle at which the reflection coefficient r_2 equals zero is called polarizing angle or Brewster angle (Born, et al., 1999). Therefore the reflection may

change the sign of the amplitude of light and introduces a phase shift π. Figure 2.4 shows phase shift of the coefficients as a function of angle of incidence. The possible changes of the sign have already been taken into account in the definition of the factors ε_1 and ε_2.

If the light ray impinges on the boundary at Brewster angle, the reflected light has no component in the plane of incidence, which means the reflected light is perpendicularly polarized. The Brewster angle is given as,

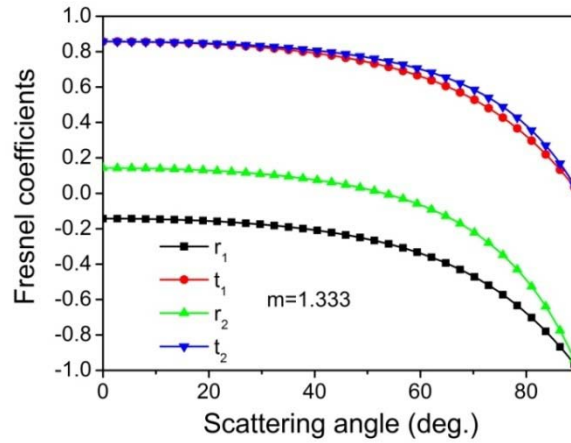$$\theta_b = \tan^{-1}(m) \tag{2.36}$$

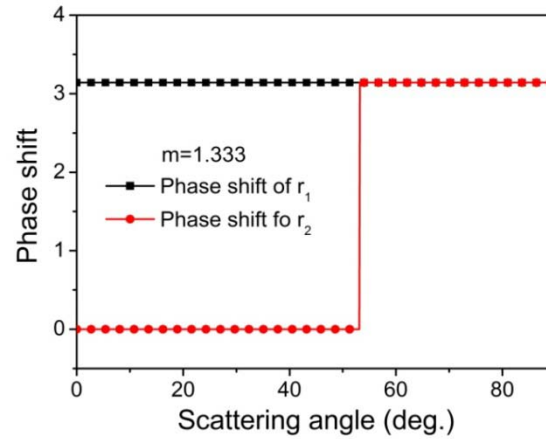Fig. 2.3.   Fresnel coefficients as a function of angle of incidence.

Fig. 2.4.   Phase shift of the coefficients as a function of angle of incidence.

So far the case when the light propagates from an optically denser medium into other one which is optically less dense is excluded, that is, the relative index defined as $m=m_2/m_1$ is smaller than 1. That case is shown in Fig. 2.5. Snell's law is then written in the following form:

$$\sin\theta_t = \sin\theta_i/m \tag{2.37}$$

Provided $\sin\vartheta_i$ equals m, then $\sin\vartheta_t=1$, i.e. $\vartheta_t=90^o$, so that the light emerges in a direction tangent to the boundary. The critical angle is defined as:

$$\theta_c = \sin^{-1}(m) \tag{2.38}$$

For example, if the light propagates from water into air, the relative refractive index is around 0.75. And the critical angle is 48.59^o.

If the incident angle exceeds the limiting angle, no light ray enters the second medium and the incident light ray is totally reflected. More precisely, although there is a field in the second medium, the time average of Poynting vector vanishes which implies the energy flows to and fro, but there is no lasting energy flow into the second medium. The field in the second medium is a kind of evanescent wave.

When $\vartheta_i>\vartheta_c$, the value $\sin\vartheta_r$ is larger than 1. The cosine of the refraction angle is given as:

$$\cos\theta_r = \sqrt{1-\sin^2\theta_r} = \sqrt{-1}\times\sqrt{\frac{\sin^2\theta_i}{m^2}-1} \tag{2.39}$$

and

$$\sqrt{-1} = \pm i \tag{2.40}$$

So

$$\cos\theta_r = i\sqrt{\frac{\sin^2\theta_i}{m^2}-1} \tag{2.41a}$$

or

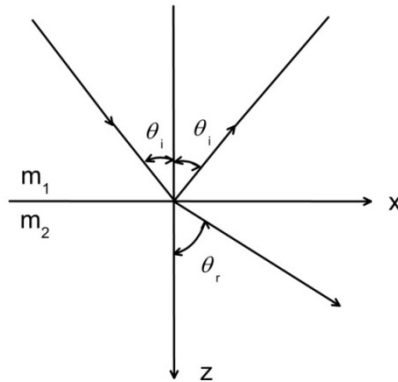$$\cos\theta_r = -i\sqrt{\frac{\sin^2\theta_i}{m^2}-1} \tag{2.41b}$$

Fig. 2.5.   Schematic view of light ray propagating from optically denser medium into optically less dense medium.

As mentioned in Chapter 2, the set of $\exp(i\omega t - i\mathbf{k}\cdot\mathbf{r})$ is adopted. In this adoption, the exponent of the transmission can be written as:

$$\exp\left[i\left(\omega t - \frac{x\sin\theta_r + z\cos\theta_r}{v_2}\right)\right] \tag{2.42}$$

Substituting Eq. (2.41) into Eq. (2.42), one can obtain;

$$\exp\left[i\left(\omega t - \frac{x\sin\theta_i}{mv_2}\right)\right] \times \exp\left(\pm\frac{z}{v_2}\sqrt{\frac{\sin^2\theta_i}{m^2}-1}\right) \tag{2.43}$$

It is obviously that only the negative sign in front of the square root in Eq. (2.43) corresponds to the physical situation. Otherwise the scattering amplitude would tend to infinite as the light propagates. When the sign in Eq. (2.43) is set to negative, Eq. (2.41b) exists and $\sqrt{-1} = -i$. However, in the choice of $\exp(-i\omega t + i\mathbf{k}\cdot\mathbf{r})$, Eq. (2.41a) exists and $\sqrt{-1} = i$.

To apply the Fresnel formulae to the case of total reflection, that is, substituting Eq. (2.41b) into Eq. (2.35), one could rewrite them in the form of;

$$r_1 = \exp(i2\delta_1'), \qquad r_2 = \exp(i2\delta_2'),$$
$$t_1 = \frac{2\cos\theta_i}{\sqrt{1-m^2}}\exp(i\delta_1'), \qquad t_2 = \frac{2m\cos\theta_i}{\sqrt{m^4\cos^2\theta_i + \sin^2\theta_i - m^2}}\exp(i\delta_2'), \tag{2.44}$$

where

$$\delta_1' = 2\tan^{-1}\left(\frac{\sqrt{\sin^2\theta_i - m^2}}{\cos\theta_i}\right), \qquad \delta_2' = 2\tan^{-1}\left(\frac{\sqrt{\sin^2\theta_i - m^2}}{m^2\cos\theta_i}\right) \tag{2.45}$$
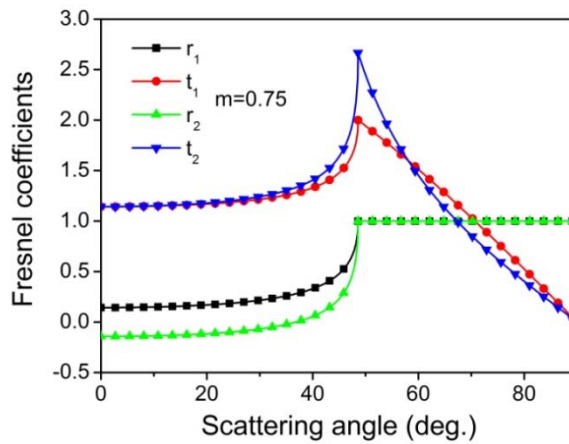

Fig. 2.6. Fresnel coefficients as a function of angle of incidence for *m*=0.75.
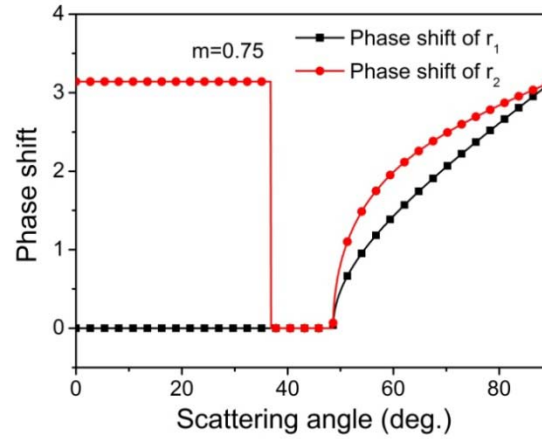
Fig. 2.7. Phase shift of the coefficients as a function of angle of incidence.

The absolute values of Fresnel coefficients as a function of angle of incidence for m=0.75 are shown in Fig. 2.6. Even though the absolute value t_1 and t_2 can be larger than 1, there is no lasting energy flow in the second medium. Most notably, as shown in Fig. 2.7, the phase shifts of the total reflected ray shift continuously from 0 to π when the angle of incidence overruns the critical angle. When the incident angle is less than the critical angle, the phase shift is of 0 or π lying on the sign of reflection coefficients r_1 and r_2.

It can be seen that geometrical optics approximation gives a close form solution for spherical particle. However for non-spherical particle, no close form solution can be given.

2.3.2 Airy approximation

With the Airy approximation (or called Airy theory) (Airy, 1838), the exit wavefront is assumed to be cubic. Applying Huygens's principle, a compact closed form for the scattered light can be obtained. For a more detailed derivation one can refer the book (van de Hulst, 1981) or the dissertation (van Beeck, 1997). The Airy approximation provides the scattering intensity in the region of the rainbow as a function of scattering angle, is valid for a spherical particle, and offers a greatly simplified computation compared with the Lorenz-Mie theory especially for large particles. Nevertheless, Lorenz-Mie computations are nowadays feasible for large spherical particles and offer a method of validation for Airy approximation. In Ref. (Wang, et al., 1991) for instance, agreement between the two approaches had been shown with increasing refractive index, even for very small particles. More explanations also can be found in Ref. (Jackson, 1999) and (Saengkaewa, et al., 2006). The scattering intensity evaluated by Airy approximation is given as (Wang, et al., 1991):

$$I = \varepsilon_j^2 \left[81 \big/ \left(16\pi^2 h^4 \right) \right]^{1/6} \times \sin\left(\theta_{irg} \right) \alpha^{7/3} F^2 \left(z \right) \big/ \cos\left(\theta_{rg} \right) \qquad j = 1, 2 \tag{2.46}$$

here the subscript j=1 is for the perpendicular polarization component and j=2 for the parallel component of the light respect to the scattering plane, and $F(z)$ is the Airy integral also called rainbow integral:

$$F\left(z \right) = \int_0^\infty \cos\left[\pi \left(zt - t^3 \right) \big/ 2 \right] \, dt \tag{2.47}$$

The Airy integral could be related to the Airy function $Ai(x)$:

$$Ai(x) = \frac{1}{\pi} \int_0^\infty \cos\left(xv + \frac{1}{3} v^3 \right) \, dv \tag{2.48}$$

After some algebra operations, one could obtain:

$$F\left(z \right) = a \cdot Ai(\frac{az}{2}) = \frac{a}{\pi} \left(\frac{az}{6} \right)^{1/2} K_{1/3} \left[\frac{2}{3} \left(\frac{az}{2} \right)^{3/2} \right], \quad for \quad z < 0$$

$$F\left(z \right) = a \cdot \frac{1}{3^{2/3} \Gamma\left(\frac{2}{3} \right)}, \qquad\qquad\qquad for \quad z = 0 \tag{2.49}$$

$$F\left(z \right) = a \cdot Ai(-\frac{az}{2}) = \frac{1}{3} a \left(\frac{az}{2} \right)^{1/2} \left[J_{1/3} \left(\frac{2}{3} \left(\frac{az}{2} \right)^{3/2} \right) + J_{-1/3} \left(\frac{2}{3} \left(\frac{az}{2} \right)^{3/2} \right) \right] \quad for \quad z > 0$$

and

$$a = \pi \left(\frac{2}{3\pi} \right)^{1/3} \tag{2.50}$$

where $K_{1/3}$ denotes the modified Bessel function, Γ the Gamma function, and $J_{1/3}$ and $J_{-1/3}$ the Bessel functions.

The variables and parameters in Eqs. (2.46)-(2.49) are defined as follow:

$$\alpha = \pi d \big/ \lambda;$$
$$z = \left(-q \right) \left[12 \big/ \left(h\pi^2 \right) \right]^{1/3} \alpha^{2/3} \left(\theta - \theta_{rg} \right);$$
$$h = \left(p^2 - 1 \right)^2 \left(p^2 - m^2 \right)^{1/2} \big/ \left[p^2 \left(m^2 - 1 \right)^{3/2} \right]; \tag{2.51}$$
$$\varepsilon_j = \left(1 - r_j^2 \right) \left(r_j \right)^{(p-1)}, \quad j = 1, 2 \quad and \quad p \geq 2;$$
$$r_1 = \frac{\cos\theta_{irg} - m\cos\theta_{rrg}}{\cos\theta_{irg} + m\cos\theta_{rrg}}; \quad r_2 = \frac{m\cos\theta_{irg} - \cos\theta_{rrg}}{m\cos\theta_{irg} + \cos\theta_{rrg}}.$$

where α is the dimensionless size parameter, d the diameter of the particle, λ the wavelength of the incident light, q an integral equaling to +1 or -1, whose physical meaning can be found in Ref. (Yu, et al., 2009), ϑ_{irg} the incident angle for rainbow ray, ϑ_{rrg} the

refractive angle for rainbow ray, ϑ_{rg} the rainbow angle and ϑ scattering angle. r_1 and r_2 are the Fresnel coefficients.

According to geometrical optics, the incident angle and refractive angle for rainbow ray are given by:

$$\theta_{irg} = \sin^{-1}\left[\left(p^2 - m^2\right)\big/\left(p^2 - 1\right)\right]^{1/2}, \quad \theta_{rrg} = \sin^{-1}\left[\left(p^2 - m^2\right)\big/ m^2\left(p^2 - 1\right)\right]^{1/2} \tag{2.52}$$

And the rainbow angle is:

$$\theta_{rg} = \pi + 2\sin^{-1}\sqrt{\frac{4 - m^2}{3}} - 4\sin^{-1}\sqrt{\frac{4 - m^2}{3m^2}} \tag{2.53}$$

The parameter z in Eq. (2.51) can be written as other form:

$$z = \left(\frac{16d^2 \cos^3 \theta_{irg}}{\lambda^2 \sin \theta_{irg}}\right)^{1/3} \left(\theta - \theta_{rg}\right) = \left[\frac{16\left(m^2 - 1\right)^{3/2}}{\pi^2 \left(p^2 - m^2\right)^{1/2}\left(p^2 - 1\right)}\right]^{1/3} \alpha^{2/3}\left(\theta - \theta_{rg}\right) \tag{2.54}$$
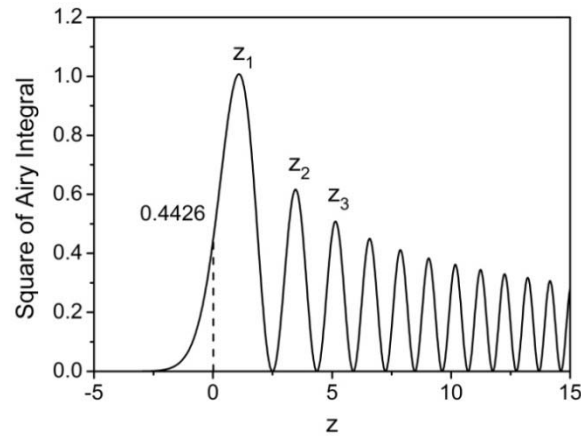

Fig. 2.8.   Distribution of the square of the Airy integral.

According to Eq. (2.46), one can see the intensity of scattered light in the rainbow region is proportional to the square of Airy integral ($F^2(z)$). And the square of Airy integral is plotted in Fig. 2.8. It is evident that there are successive maxima and minima on the curve. The heights of the maxima and the values of z for which the maxima and minima are reached are given in Table 2.1 ((van de Hulst, 1981) and (van Beeck, et al., 1995)).
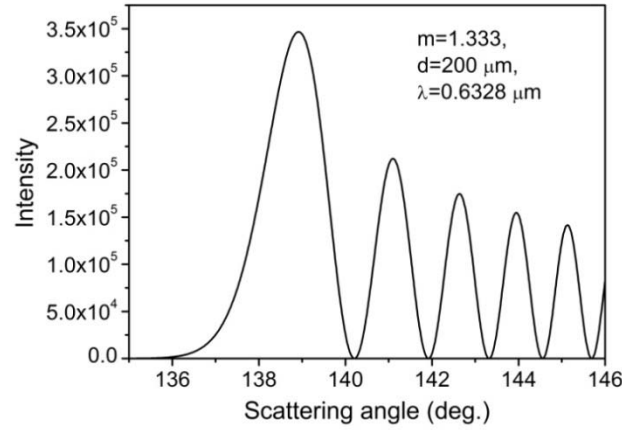
Fig. 2.9. Scattered light intensity distribution calculated using Airy approximation for the perpendicular polarization component.

Table 2.1. Maxima and minima in the square of the Airy integral

	z	$F^2(z)$
Main rainbow	1.0874	1.0075
First minimum	2.4956	0
First subsidiary maximum	3.4668	0.6165
Second minimum	4.3632	0
Second subsidiary maximum	5.1446	0.5081
Third minimum	5.8922	0
Third subsidiary maximum	6.5782	0.4498
Fourth minimum	7.2436	0
Fourth subsidiary maximum	7.8684	0.4114

In Fig. 2.9, the light scattering intensity distribution calculated by Airy approximation for the perpendicular polarization component is shown. ϑ_1, ϑ_2, ϑ_3….. are used to denote the successive scattering angles for which the maximal intensity is observed.

For the first and second maxima of square of Airy integral shown in Table 2.1,

$$z_1 = 1.0874, \qquad z_2 = 3.4668 \tag{2.55}$$

By substituting Eq. (2.55) into Eq. (2.54), one can obtain:

$$\frac{\theta_1 - \theta_{rg}}{\theta_2 - \theta_{rg}} = \frac{1.0874}{3.4668} = C \tag{2.56}$$

So the rainbow angle can be expressed as:

$$\theta_{rg} = \frac{\theta_1 - C\theta_2}{1 - C} \tag{2.57}$$

If one can detect the θ_1 and θ_2 from experiment, then one could obtain the rainbow angle θ_{rg} according to using Eq. (2.57). Finally, one can calculate the refractive index using Eq. (2.53). From Eq. (2.54), the diameter can be expressed by the following formula:

$$d = \frac{\lambda}{4} \left(\frac{z_1 - z_2}{\theta_1 - \theta_2} \right)^{3/2} \left[\frac{3\left(4 - m^2\right)^{1/2}}{\left(m^2 - 1\right)^{3/2}} \right]^{1/2} \tag{2.58}$$

The above equations will be used to calculate the refractive index and diameter in Chapter. 6. In ref. (Roth, et al., 1996), an inversion algorithm based on inflection points was used to calculate the refractive index and size of droplet. Further inversion algorithms can be found in Ref. (van Beeck, et al., 2001).
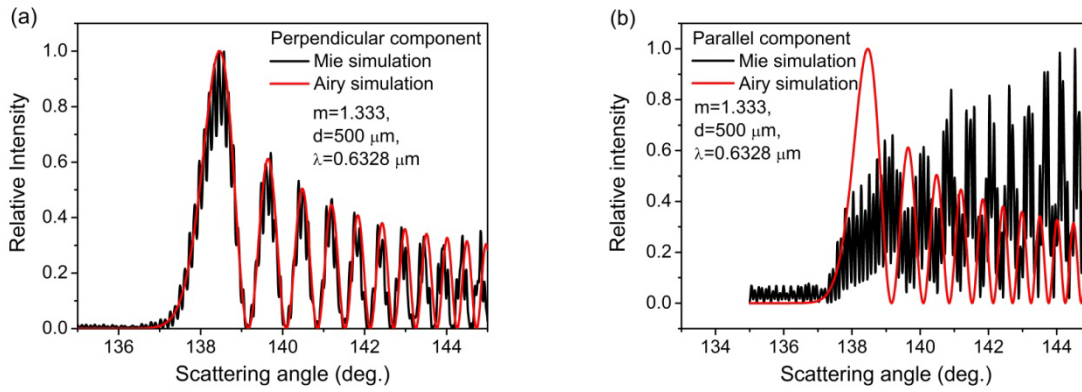

Fig. 2.10.   Comparison of the intensity distribution calculated by Lorenz-Mie theory and Airy approximation for a water droplet in air in the rainbow region: (a) for the perpendicular polarized component and (b) for the parallel polarized component.

In the above discussion, only the perpendicularly polarized component is taken into account. As is well known, rainbow light is strongly polarized (Können, et al., 1979), with the perpendicularly polarized component completely dominating. The polarization character also depends on the material of the droplet, which will be discussed in the following.

In the Airy approximation, the polarization character was not considered. Wang and van de Hulst (1991) generalized the Airy approximation to the two polarization directions. The comparison of intensity distributions calculated by using Lorenz-Mie theory and Airy approximation for water droplet is shown in Fig. 2.10. To facilitate comparing two simulation results, the intensity distributions are normalized by setting the maximum to be 1 for the

two methods respectively. The Airy approximation agrees with Mie theory very well for the perpendicular polarization component as shown in Fig. 2.10a. In the Airy approximation, only the second-order refractions are taken into account. So, only supernumerary arcs can be seen, without ripple structures, which can be observed in the Lorenz-Mie simulation. However, for the parallel component, the deviation of Airy simulation from Lorenz-Mie simulation is obvious, which is evident in Fig. 2.10b. So the Airy approximation cannot be used to calculate the parallelly polarized component of scattered light in the rainbow region. In summary, there remains a feature of the rainbow where Airy's description breaks down. The reason for this is that light rays, responsible for the rainbow, are always at least reflected once inside the water droplet; for the Descartes ray this reflection occurs close to the Brewster angle. As mentioned before, the scattered light in rainbow region is strongly polarized and the perpendicular component dominates strongly. Therefore, Airy approximation is a very good approximation of the rainbow.

2.4 Polarization character of light scattering in rainbow region

Light, being a transverse wave, exhibits an orientation direction perpendicular to the direction of propagation, known as the polarization. The orientation of the transverse oscillation can be resolved into components along two mutually perpendicular axes and any light ray can be described in terms of these two independent states of linear polarization. The polarization character of reflected and transmitted rays at the interface between two media can change. However at some angle of incidence, the reflection is almost completely polarized. The Brewster angle is such an angle.

The Brewster angle, also known as the polarization angle, is an angle of incidence at which light with a particular polarization is perfectly transmitted through a transparent dielectric surface, exhibiting no reflection. The polarization angle is given by (Born, et al., 1999):

$$\theta_b = \tan^{-1}(m) \tag{2.59}$$

As shown by Eq. (2.59), the polarization angle varies with the relative refractive index (m) of medium. Since the relative refractive index for a given medium changes depending on the wavelength of light, the polarization angle will also vary with wavelength. For an air-water interface, the polarization angle is 53.06^o for the light with wavelength of 632.8 nm. For the same interface, it is 53.27^o for the light with wavelength of 400 nm (Bashkatov, et al., 2002).

Consider the polarization character of a light ray that reaches an air-water droplet surface. As shown in Fig. 2.11, the incident ray, the reflective ray and the transmitted (refractive) ray are in the same plane. The polarization states of the incident light can be defined as being parallel to that plane and perpendicular to the plane. For the condition that the angle of incidence is the Brewster angle, the parallel polarized component is entirely transmitted. So, there is no parallel component in the reflected ray ($p=0$), that is, the reflected ray is completely perpendicularly polarized.
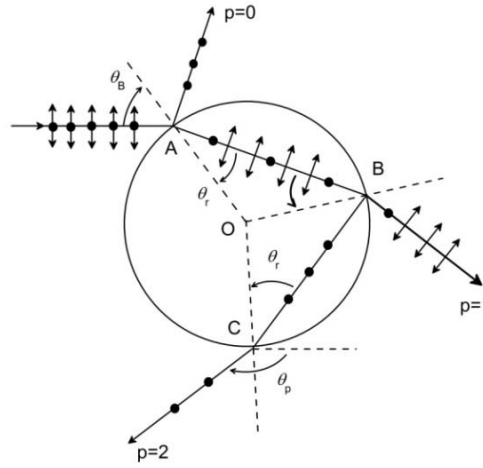

Fig. 2.11.   Illustration of the polarization of light transmission in a sphere with the incident angle impinging at the Brewster angle.

Using Snell's law, the refractive angle is $\vartheta_r = \tan^{-1}(1/m)$ if the incident angle is the Brewster angle. Exploiting the symmetry of the sphere, one can know that the incident angles are also θ_r for the first inner reflection (at point B), for the second inner process (at point C), and for the high order inner processes. When a light ray hits the inner droplet-air surface, the Brewster angle also equals $\tan^{-1}(m)$. So the reflected ray at point B, i.e. the incident ray for the second inner process, is completely polarized (see Fig. 2.11). However, the refracted ray ($p=1$) at point B is partially polarized, in which the parallel component dominates. Because the incident ray is completely polarized, the transmitted ray (at point C) is also completely polarized. According to geometric optics, when the light ray is incident on the droplet at the Brewster angle, the transmission ray ($p=2$) is completely polarized. As for all analysis based on geometric optics, the polarization of scattering orders will not depend on the size of the droplet.

37

From geometrical optics, the angle of deflection $\theta_p(m,\theta_i)$ between the pth emerging ray and the direction of the incident ray is given as (van de Hulst, 1981):

$$\theta_p(m,\theta_i) = (p-1)\pi + 2\theta_i - 2p\theta_r \quad p = 0,1,2,3 \cdots \tag{2.60}$$

using Snell's law $\sin\vartheta_i = m\sin\vartheta_r$, where ϑ_i is the incident angle, ϑ_r the refractive angle, and m the relative refractive index of the particle to the surrounding medium. According to geometrical optics, if the ray is incident at some special angle, the scattering angle given by Eq. (2.60) exhibits a minimal value, which is called the geometrical optics rainbow angle. The rainbow angle is given by:

$$\theta_{rg} = \pi + 2\cos^{-1}\left(\frac{m^2-1}{3}\right)^{\!\!1/2} - 4\cos^{-1}\left(\frac{4(m^2-1)}{3m^2}\right)^{\!\!1/2} \tag{2.61}$$

Suppose the incident angle is the Brewster angle given by Eq. (2.59), one can obtain other special scattering angles. Here it is called as polarization scattering angle ϑ_{psa}. By substituting Eq. (2.59) into Eq. (2.60), one can obtain:

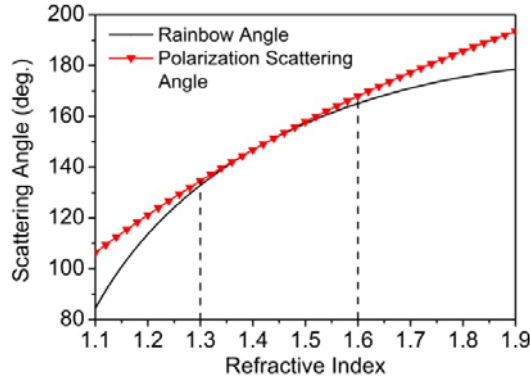$$\theta_{psa} = \pi + 2\tan^{-1}(m) - 4\tan^{-1}(1/m) \tag{2.62}$$

Fig. 2.12. Comparison between the rainbow angle and the polarization scattering angle.

In Fig. 2.12 the relation between the rainbow angle ϑ_{rg} and the relative refractive index is shown by the black curve. For different relative refractive indexes, the polarization scattering angle ϑ_{psa} of a ray whose incidence is the Brewster angle is shown by the red curve. For small relative refractive indexes, the rainbow angle is not close to the polarization scattering angle. However, when the refractive index is larger than 1.30 and smaller than 1.60, the two angles are almost the same. The relative refractive index of the water droplet is 1.333 at a wavelength of 632.8 *nm*, for which the rainbow angle is very close to the

polarization scattering angle. This explains why the rainbow is almost completely polarized. As shown in Fig. 2.11, it is the perpendicular component that strongly dominates.
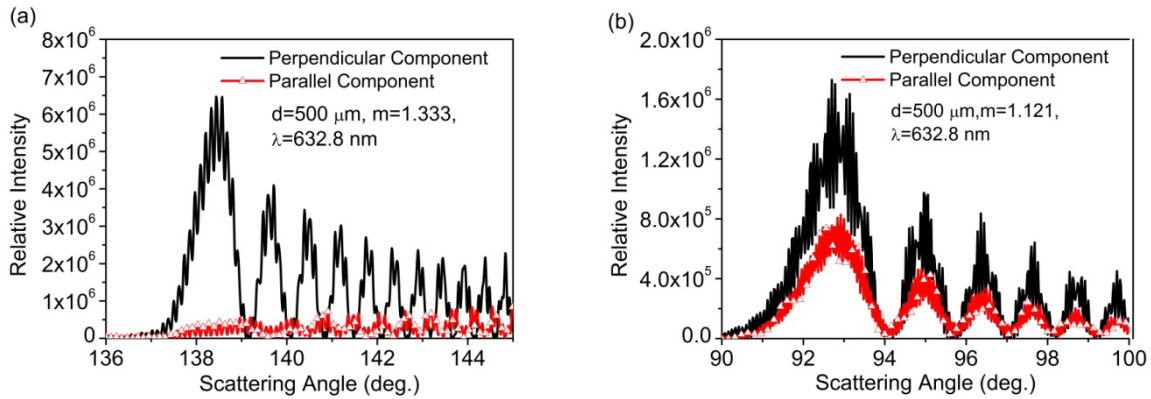

Fig. 2.13. Polarization character of scattering for a spherical particle in the rainbow region. The particle diameter is 500 *µm*; (a) m=1.333 at a wavelength 632.8 *nm;* (b) *m*=1.121 at a wavelength 632.8 *nm*.

Then the intensities of the parallel and perpendicular polarized light for different scattering angles are examined. Figure 2.13a shows the light intensity distribution scattered by a spherical particle having *d*=500 *µm* and *m*=1.333 at a wavelength of 632.8 *nm* in the rainbow region. These distributions were calculated by using Lorenz-Mie theory (Mie, 1908). It can be seen that the perpendicular component is much stronger than the parallel component (more than 10 times). That is consistent with the analysis given in Fig. 2.11. Figure 2.13b shows the intensity distribution for a particle having the same parameters as Fig. 2.13a, but with *m*=1.121. According to geometric optics, the rainbow angle is 91.81^{o} for this refractive index. So, the scattering angle region is between 90° and 100° shown in Fig. 2.13b. It can be seen that the parallel component is not weak compared to the perpendicular component. However for relative refractive indexes larger than 1.30 and smaller than 1.60, the rainbow angle is close to the polarization scattering angle. It means that the perpendicular component of the rainbow completely dominates for 1.30<m<1.60.

Chapter 3   Vector ray tracing model

The vector ray tracing (VRT) model (Yu, et al., 2013) for a spheroid is presented in this chapter, which of course can be used for spheres and particles with complex shape. Firstly, the vector formulation of reflection and refraction are given. Then the light propagation at interfaces is discussed, including propagation of a ray from an optically less dense medium into an optically denser one and vice versa. Then the VRT model is presented. For a given incident light ray, the reflected ray, transmitted rays, and the intersection of the inside ray with the particle are given in detail. Furthermore, results of the vector ray tracing simulation for a sphere and spheroid are given.

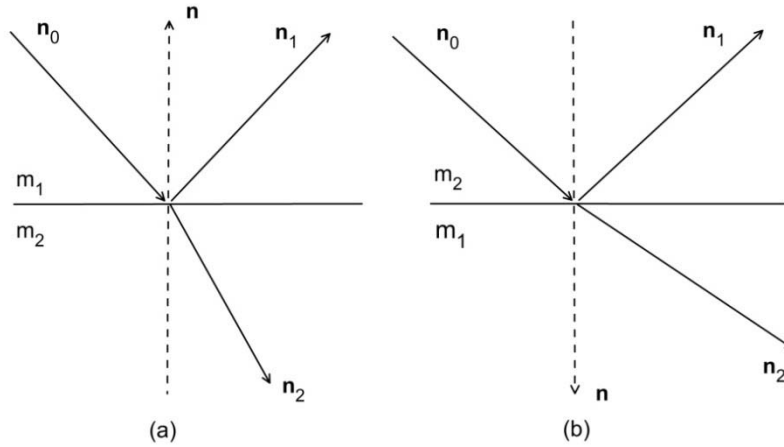## 3.1   The vector formulation of reflection and refraction

Fig. 3.1.   The illustration of light ray propagation in two media.

It is assumed that light propagates from medium 1 to medium 2 (see Fig. 3.1a) or from medium 2 to medium 1, whereby the wavelength dependent refractive indices are given by m_1 and m_2 respectively.

Let $\mathbf{n}_0$ be the unit vector along the direction of the incident ray, $\mathbf{n}_1$ the unit vector along the reflection ray, $\mathbf{n}_2$ the unit vector along the refractive ray, $\mathbf{n}$ the normal at the incident point on the interface between the two media, which points from medium 2 to medium 1. Then the vector formulations for reflection and refraction can be written as:

$$\mathbf{n}_1 = \mathbf{n}_0 - 2(\mathbf{n}_0 \cdot \mathbf{n})\mathbf{n} \tag{3.1}$$

$$\mathbf{n_2} = \frac{1}{m}\left[\mathbf{n_0} - (\mathbf{n_0} \cdot \mathbf{n})\mathbf{n}\right] - \left[1 - \frac{1}{m^2} + \frac{1}{m^2}(\mathbf{n_0} \cdot \mathbf{n})^2\right]^{1/2}\mathbf{n} \qquad (3.2)$$

which is for the case of light rays propagating from medium 1 to medium 2 as shown in Fig. 3.1a. Here m is the relative refractive index defined by the ratio of m_2 to m_1 ($m=m_2/m_1$).

For the second case as shown in Fig. 3.1b, the vector formulations for reflection and refraction ray are:

$$\mathbf{n_1} = \mathbf{n_0} - 2(\mathbf{n_0} \cdot \mathbf{n})\mathbf{n} \qquad (3.3)$$

$$\mathbf{n_2} = m\left[\mathbf{n_0} - (\mathbf{n_0} \cdot \mathbf{n})\mathbf{n}\right] + \left[1 - m^2 + m^2(\mathbf{n_0} \cdot \mathbf{n})^2\right]^{1/2}\mathbf{n} \qquad (3.4)$$

Suppose m_2 is larger than m_1, which means m is smaller than 1. The physical meaning is that the light propagates from an optically denser medium into an optically less dense one. Attention has to be paid to the total reflection. When the incident angle exceeds the critical angle, the square root in Eq. (3.4) is a complex number.

By comparing Eq. (3.1) with Eq. (3.3), one can see that the two vector reflection formulations are same for the two cases. However, for refraction, the two vector formulations for Fig. 3.1a and Fig. 3.1b are different. The two cases correspond to the light ray propagating from outside into a particle, and the light ray propagating from the inner side of a particle to outside respectively. Equations (3.1)-(3.4) will be used to trace the light ray propagation in spheroidal particles in the following section.

3.2   The illustration of vector ray tracing in ellipse
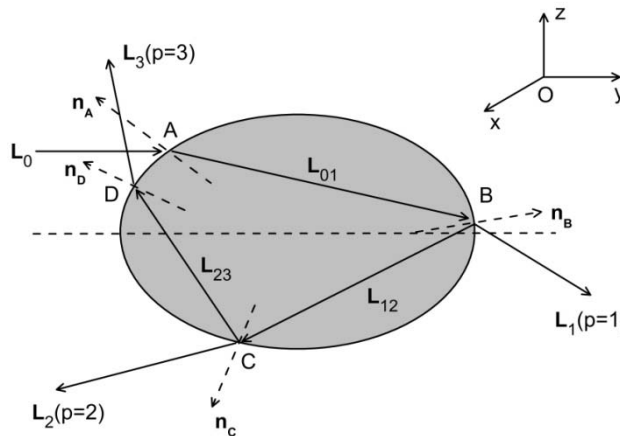

Fig. 3.2.   The illustration of vector ray tracing for ellipse.

Suppose the origin of the coordinate is in the center of the particle and the surface of the particle obeys the following equation:

$$\frac{x^2}{a^2}+\frac{y^2}{a^2}+\frac{z^2}{c^2}=1 \qquad (3.5)$$

where a and c are the long semi-diameter and the short one of the ellipse as shown in Fig. 2. An oblate spheroid can be considered as a quadratic surface obtained by rotating the ellipse about its minor axis.

Consider a light ray $\mathbf{L_0}$ encountering on the surface of the particle at the point A, whose direction can be expressed as a unit vector:

$$\mathbf{L_0}=(0,1,0) \qquad (3.6)$$

If the coordinate of incident point A is (x_0, y_0, z_0), the normal of the surface at point A is given by:

$$\mathbf{n}_A=\left(\frac{c^2 x_0}{\sqrt{c^4 x_0^2+c^4 y_0^2+a^4 z_0^2}},\frac{c^2 y_0}{\sqrt{c^4 x_0^2+c^4 y_0^2+a^4 z_0^2}},\frac{a^2 z_0}{\sqrt{c^4 x_0^2+c^4 y_0^2+a^4 z_0^2}}\right) \qquad (3.7)$$

In a simple case, the incident ray is in the yz plane, that is, the coordinate of A can be $(0, y_0, z_0)$. The normal of the surface at point A is given by:

$$\mathbf{n}_A=\left(0,\frac{c^2 y_0}{\sqrt{c^4 y_0^2+a^4 z_0^2}},\frac{a^2 z_0}{\sqrt{c^4 y_0^2+a^4 z_0^2}}\right) \qquad (3.8)$$

By using the vector reflection formula Eq. (3.1) and refraction formula Eq. (3.2), one can obtain the reflection ray and refraction ray at point A:

$$\mathbf{L_r}=\mathbf{L_0}-2(\mathbf{L_0}\cdot\mathbf{n}_A)\mathbf{n}_A,$$
$$\mathbf{L_{01}}=\frac{1}{m}\left[\mathbf{L_0}-(\mathbf{L_0}\cdot\mathbf{n}_A)\mathbf{n}_A\right]-\sqrt{1-\frac{1}{m^2}+\frac{1}{m^2}\left(\mathbf{L_0}\cdot\mathbf{n}_A\right)^2}\ \mathbf{n}_A. \qquad (3.9)$$

here m is the relative refractive index of particle to that of the surrounding medium. Then, the reflection and refraction rays at point B, C, and D are given as follows:

$$\mathbf{L_{12}}=\mathbf{L_{01}}-2(\mathbf{L_{01}}\cdot\mathbf{n}_B)\mathbf{n}_B,$$
$$\mathbf{L_1}=m\left[\mathbf{L_{01}}-(\mathbf{L_{01}}\cdot\mathbf{n}_B)\mathbf{n}_B\right]+\sqrt{1-m^2+m^2\left(\mathbf{L_{01}}\cdot\mathbf{n}_B\right)^2}\ \mathbf{n}_B, \qquad (3.10)$$

$$\mathbf{L_{23}}=\mathbf{L_{12}}-2(\mathbf{L_{12}}\cdot\mathbf{n}_C)\mathbf{n}_C,$$
$$\mathbf{L_2}=m\left[\mathbf{L_{12}}-(\mathbf{L_{12}}\cdot\mathbf{n}_C)\mathbf{n}_C\right]+\sqrt{1-m^2+m^2\left(\mathbf{L_{12}}\cdot\mathbf{n}_C\right)^2}\ \mathbf{n}_C, \qquad (3.11)$$

$$\mathbf{L_3}=m\left[\mathbf{L_{23}}-(\mathbf{L_{23}}\cdot\mathbf{n}_D)\mathbf{n}_D\right]+\sqrt{1-m^2+m^2\left(\mathbf{L_{23}}\cdot\mathbf{n}_D\right)^2}\ \mathbf{n}_D,$$

here $\mathbf{n}_B$, $\mathbf{n}_C$, and $\mathbf{n}_D$ are the surface normals at point B, C, and D respectively.

To calculate the incident angle ϑ_i at incident point A is to measure the acute angle between the vectors $\mathbf{L_0}$ and $\mathbf{n}_A$. The refractive angle ϑ_r equals the acute angle between $\mathbf{L_0}$ and $\mathbf{n}_A$. The two angles are given as:

$$\theta_i = \cos^{-1}\left(\mathbf{L_0} \cdot \mathbf{n}_A\right),$$
$$\theta_r = \cos^{-1}\left(\mathbf{L_{01}} \cdot \mathbf{n}_A\right). \tag{3.12}$$

where the two angles, which will be used to calculate the reflection and transmission coefficients in Fresnel's formulae, obey Snell's law.
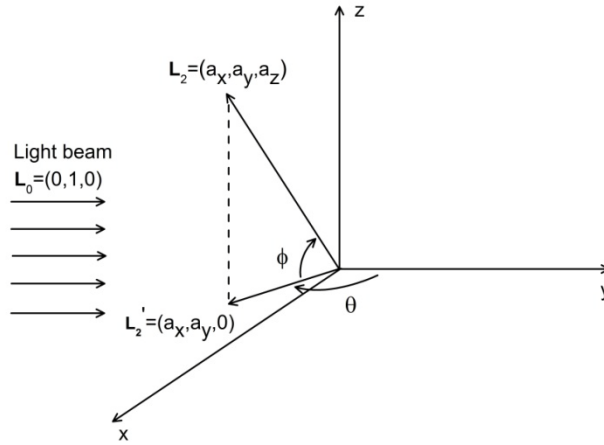

Fig. 3.3. Definition of the scattering angles.

Using Eqs. (3.7)-(3.11), the direction of the second-order refracted ray associated with the primary rainbow can be calculated in for a three-dimensional geometry, yielding $\mathbf{L_2}=(a_x, a_y, a_z)$ (see Fig. 3.3). Projecting $\mathbf{L_2}$ onto the xy-plane yields $\mathbf{L_2}=(a_x, a_y, 0)$. Furthermore, one can define θ as an off-axis angle measured from the y-axis to be:

$$\theta = \cos^{-1}\left[a_y \Big/ \left(a_x^2 + a_y^2\right)^{1/2} \right], \tag{3.13}$$

and ϕ as an elevation angle with respect to the xy plane to be:

$$\phi = \cos^{-1}\left[\left(a_x^2 + a_y^2\right)^{1/2} \Big/ \left(a_x^2 + a_y^2 + a_z^2\right)^{1/2} \right]. \tag{3.14}$$

3.3 Intersection point of a light ray and surface of particle

Suppose the directional vector of a light ray can be described by $\mathbf{n}=(m_0, n_0, p_0)$. And point (x_0, y_0, z_0) is any point on the light ray. The light ray may be an incident ray, reflection ray or refraction ray. The equation of the light ray can be expressed as:

$$\frac{x-x_0}{m_0}=\frac{y-y_0}{n_0}=\frac{z-z_0}{p_0} \tag{3.15}$$

In Eq. (3.15), it is assumed that $m_0 \neq 0$, $n_0 \neq 0$, and $p_0 \neq 0$. If one or two of the three parameters (m_0, n_0, and p_0) equals zero, the physical meaning of the light ray can be explained as follows. Supposing $m_0=0$, $n_0 \neq 0$, and $p_0 \neq 0$, the light ray is perpendicular to the x-axis. If $m_0=0$, $n_0=0$, and $p_0 \neq 0$, the light ray perpendicular to x-axis and y-axis, that is, it is parallel to z-axis.

And suppose the particle is an ellipsoid. Then the surface of the particle is a closed quadric surface and is a three dimensional analogue of an ellipse, i.e. an ellipsoid. The standard equation of an ellipsoid centered at the origin of a Cartesian coordinate system is given as:

$$\frac{x^2}{a^2}+\frac{y^2}{b^2}+\frac{z^2}{c^2}=1 \tag{3.16}$$

where a, b and c are called the semi-principal axes along the coordinate axes. If two of the three parameters equal each other, the ellipsoid reduces to a spheroid. For example, for an oblate spheroid, $a=b$ and $a>c$.

Consider a light ray impinging on the particle surface at the point (x_0, y_0, z_0). The light ray will intersect the particle surface at other points. However when the light ray is tangent to the particle surface, the ray only intersects the particle surface only at one singular point. The other intersection point (x_2, y_2, z_2) can be calculated. The detailed derivations can be found in Appendix A.

In summary, given the direction of the light ray described by the vector (m_0, n_0, p_0), the functional form of the particle surface, and one intersection point (x_0, y_0, z_0) of the light ray and particle surface, the other intersection point can be calculated according to Appendix A.
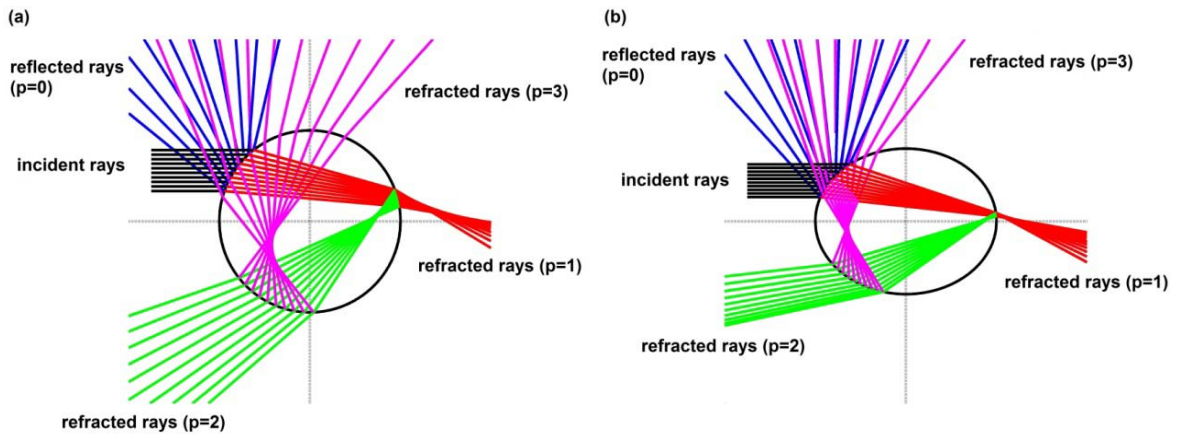
3.4 Vector ray tracing simulation

Fig 3.4.   Vector ray tracing for water droplets: (a) a=100, a/c=1.00; (a) a=100, a/c=1.25.

45

Figure 3.4 displays the vector ray tracing for spherical and spheroidal water droplets (*m*=1.333). For clarity, only rays close to the primary Descartes ray are presented. The reflected rays (*p*=0) and refracted rays (p=1, 2, 3 respectively) for sphere are shown in Fig 3.4a. Figure 3.4b presents the rays for a spheroidal droplet with aspect ratio *a*/*c*=1.25. It can be seen from Fig 3.4 that the second-order refracted rays (green lines) are more tightly focused for a spheroid than that for a sphere. Attention must be paid to the fact that total internal reflection occurs for a spheroid, while not for a sphere.

Based on the vector ray tracing model described above, the optical caustics observed in the light scattering from an oblate spheroidal droplet will be investigated in next chapter.

Chapter 4   Simulation of optical caustic structure for oblate droplets

Optical caustics exist in light scattering from spherical and oblate droplets. The hyperbolic umbilic (HU) diffraction catastrophe in the primary rainbow region of an oblate water droplet was first observed by Marston and Trinh (Marston, et al., 1984). The optical caustic structures, including the location of cusp caustic and opening rate of the cusp diffraction etc., were successfully described by some theoretical approximation models ((Marston, 1985), (Marston, 1987), (Marston, et al., 1989), (Dean, et al., 1991), and (Marston, 1999)). Most notably, Nye studied the landmark features of the far-field caustics including HU foci, lip events and the E_6 catastrophe according to geometrical optics (Nye, 1992). In addition, the optical caustics have also been observed from the light scattering by oblate droplets with white light illumination ((Simpson, et al., 1991) and (Kaduchak, et al., 1994)). Both the primary and higher order rainbow caustics of the scattering of light from oblate water droplets ((Kaduchak, et al., 1994), (Marston, et al., 1994) and (Langley, et al., 1998)) and internal caustic structures of illuminated liquid droplets (Lock, et al., 1991) have been observed and analyzed. Recently, Debye series has been developed to analyze the formation of rainbow caustic, transverse cusp and HU caustics for a spheroid. Compared to the analysis within the framework of diffraction catastrophe and catastrophe optics ((Berry, et al., 1979) and (Berry, et al., 1980)), Debye series is an exact analysis tool for studying Mie scattering by a spheroid. However, it has not been applied to droplet size of hundreds of microns due to the numerical problems in computation.

In this chapter, a vector ray tracing (VRT) model is employed to simulate the optical caustic structures near the primary and the secondary rainbow scattering angles of oblate water droplets. The location of the cusp caustics in the two rainbow regions are calculated from the VRT model and compared with that calculated from analytical solutions and excellent agreement is found. Moreover, in order to apply the optical caustic structures to particle diagnostics, the evolution process of the optical caustic structures in response to shape deformation of the water droplet are discussed in detail.

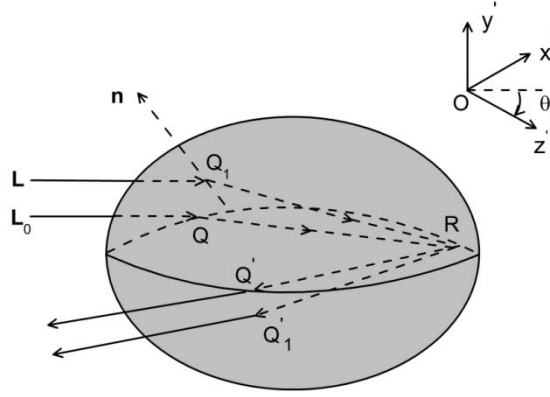## 4.1   Location of cusp caustic of the primary rainbow

Fig. 4.1.   Rays associated with the cusp caustic.

As is well known, the cusp caustic is associated with the contribution from two equatorial rays and two skew rays (Marston, et al., 1984) and the VRT model allows the cusp caustic to be identified (see Fig 4.1). On the other hand, Nye obtained a derivation for calculating the droplet aspect ratio when the hyperbolic umbilici catastrophe can be observed (Nye, 1984). Furthermore, an analytical solution to predict the location of cusp caustic was given based on Herzberger's formalism (Marston, 1985). In the present study the analytical solution for calculating the cusp location is derived based on geometric optics (see Appendix B):

$$a/c = m\left[2\left(m^2 - \sin^2\theta_i\right) - 2\left(m^2 - \sin^2\theta_i\right)^{1/2}\left(1 - \sin^2\theta_i\right)^{1/2}\right]^{-1/2}.$$
(4.1)

Equation (4.1) is as same as that obtained by Marston using Herzberger's formalism (Marston, 1985). For the spheroid with an aspect ratio satisfying the condition Eq. (4.1), the skew rays will focus vertically. The two skew rays are above and below the equatorial plane respectively. Together with the two equatorial rays, they focus in the same direction, giving rise to the cusp caustic. According to geometrical optics, the scattering angle of the cusp ray is given by $\vartheta = \pi + 2\vartheta_i - 4\sin^{-1}(\sin\vartheta_i/m)$ and the primary Descartes ray satisfies $\sin\vartheta_i = (4 - m^2/3)^{1/2}$. Substitution into Eq. (4.1) yields the critical aspect ratio:

$$a/c = \left[3m^2 \big/ \left(4m^2 - 4\right)\right]^{1/2}$$
(4.2)

 i.e. the ratio at which HUFS arises. This result is identical to that given by Nye (Nye, 1984).
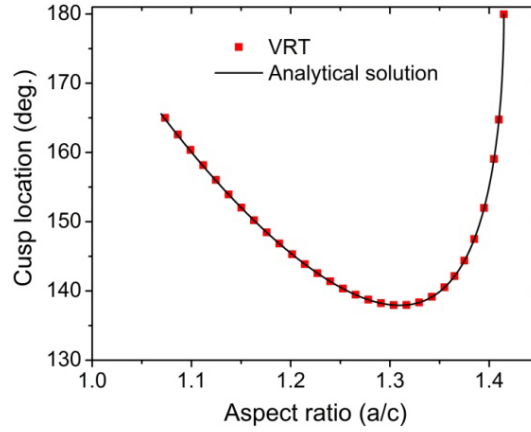
Fig. 4.2.   Comparison of the cusp location calculated by VRT and that by the analytical solution in the primary rainbow region for oblate water droplets with different aspect ratios.

Then the location of cusp caustic is calculated by use of the analytical solution Eq. (4.1) and compared with that calculated by VRT simulations. Figure 4.2 displays such a comparison. The cusp caustic first appears at θ=165.57° for oblate water droplets with aspect ratio a/c=1.069389. When the ratio increases, the cusp moves to smaller scattering angles until it merges with the primary rainbow caustic at θ=137.92° for a/c=1.309779. Then the cusp shifts to larger scattering angles and disappears at θ=179.96° for a/c=1.414742. The agreement between the analytic solution (Marston, 1985) and the VRT simulations is excellent, with only minor deviations due to the finite grid resolution of incident rays.

4.2 Optical caustic structures of the primary rainbow

On the basis of VRT validation in terms of the location of cusp caustic, the shape of the rainbow and HU fringes, referred to as structures of optical caustics are computed. For the second-order refracted rays (p=2 in geometrical optics), there is a revolution (turning point) at the deflection angle of the primary Descartes ray. This angle is where the primary rainbow fringe forms. In VRT model, the rainbow fringe can be identified from infinitively large density of the emergent rays. As the HU caustics are associated with the contribution from skew rays (Nye, 1984), it can be identified by the VRT model. Considering the beam divergence in the droplet, a sufficient number of rays have to be used to ensure the numerical accuracy. To display the extremely high sensitivity of optical caustics on aspect ratio of oblate droplet, the precision of the aspect ratio is given to the sixth decimals in some places of the following studies.

49

For water droplets with the relative refractive index m=1.333 and equatorial radius $100\mu m$, but with different aspect ratios, the rainbow fringe and HU fringe in the primary rainbow region are computed. To fully display the caustic structures, only part of the caustic structure (within $-10^o \leq \varphi \leq 10^o$) is given in the numerical demonstrations. Figure 3a shows the primary rainbow fringe for a spherical droplet (a/c=1). For this aspect ratio the primary rainbow fringe exhibits a weak curvature with respect to the elevation angles and bends towards larger scattering angles (the backward direction). The left-most point (apex point) of this fringe is the rainbow caustic point in the equatorial plane. Its relevant pattern is the fold diffraction catastrophe symbolized by A_2 in catastrophe optics (Berry, et al., 1980). The cusp caustic first appears for a droplet with aspect ratio a/c =1.07 (θ=165.52°), which is consistent with theoretical prediction ((Marston, 1985) and (Nye, 1992)). Four rays are responsible for its formation. Two are in the equatorial plane focusing horizontally whereas the other two are skew rays offset vertically from the equatorial plane but also focusing in the horizontal direction. For a/c =1.07, only a cusp point appears in Fig. 4.3b. When the aspect ratio further increases, the HU fringe unfolds in Fig. 4.3c and the cusp caustic shifts towards smaller scattering angles (the forward direction). Further increment of the ratio makes the HU fringe gradually unfold, as shown in Fig. 4.3d. Together with the unfolding of HU fringe, the rainbow fringe exhibits an increased curvature because the primary Descartes rays off the equatorial plane shift backward more as the aspect ratio increases. For a droplet with a/c=1.27, the rainbow fringe partly overlaps with the HU fringe (Fig. 4.3e) and for a/c=1.31 the cusp caustic merges completely with the primary rainbow caustic (Fig. 4.3f), creating the so-called hyperbolic umbilic focal section (HUFS) symbolized by D_4^+, which is consistent with experiment (Marston, et al., 1984) and theoretical prediction ((Marston, 1985) and (Nye, 1992)). HUFS is described by three control parameters C_1, C_2 and C_3 in catastrophe optics (Berry, et al., 1980) and its apex angle is experimentally measured to be 43.5±1° (Marston, et al., 1984). In VRT simulation the apex angle is 43.42°, which agrees very well with the experimental value, exhibiting only slight differences, all lying within the uncertainty band of the experimental value. An analytic expression for calculating the apex angle was also given by Marston (Marston, 1992), predicting it as 42.1^o. The main reason for this small deviation of the apex angle between VRT simulation and the analytic expression is due to the fact that the two arms of the rainbow fringe are highly curved at the apex and the mesh size in the VRT simulation is not infinitely small. When the ratio further increases, the cusp shifts

50

further backward and the HU fringe gradually degenerates (Fig. 4.3g). For the aspect ratio *a/c*=1.414742 (Fig. 4.3h), the fringe collapses into the cusp caustic point at 179.96° also agreeing with theoretical prediction ((Marston, 1985) and (Nye, 1992)). Then no cusp caustic is observed for 1.414742<*a/c*<1.525000 (Fig. 4.3i). However, it reappears at large ratios such as *a/c* =1.60 (Fig. 4.3j), creating the E_6 diffraction catastrophe also called symbolic umbilic focal section (Berry, et al., 1980). Note that for E_6, the rainbow fringe is bent towards smaller scattering angles. The progression of optical caustic structures in response to the change of aspect ratio of oblate droplet is consistent with change of the first and HU bows of the generalized rainbow patterns observed in experiment (Marston, et al., 1984) and Nye's simulation based on geometrical optics (Nye, 1992).
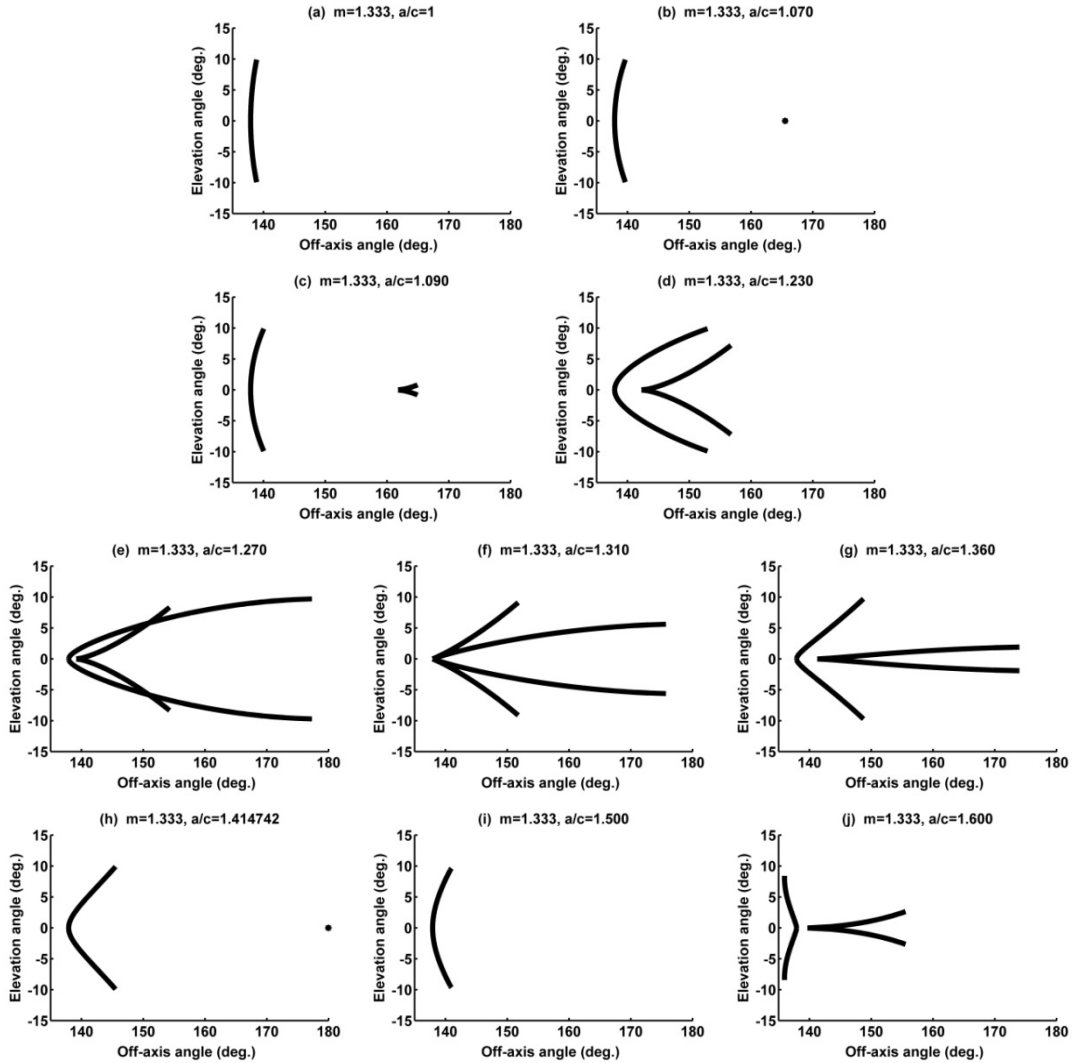

Fig. 4.3.   Evolution of the primary rainbow fringe and the HU fringe as the aspect ratio of an oblate water droplet increases.

Then Fig. 4.4 displays the primary rainbow fringes for oblate droplets with the same refractive index (*m*=1.333) and aspect ratio (*a/c*=1.21) but different equatorial radii (100µm, 500µm, and 1000µm respectively) (Yu, et al., 2013). All rainbow fringes present the same concave shape (bending towards larger scattering angles), symmetric about horizontal plane and overlapping completely due to the independence of rainbow fringe on droplet size. However simulations for other types of liquid droplets show that the rainbow fringe shape is dependent on the refractive index of droplet. The comparison of the rainbow fringes for oblate droplets with the same aspect ratio and equatorial radius but different refractive indices are shown in Fig. 4.5. The rainbow fringe for a silicone oil droplet (*m*=1.400) is bent much more than that for water droplet (*m*=1.333). The rainbow caustic appears at 146.75^o for a silicone oil droplet in the equatorial plane and at 137.92^o for a water droplet.
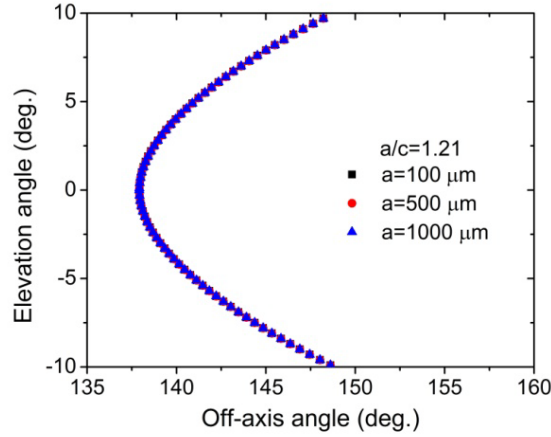

Fig. 4.4.   Primary rainbow fringes for oblate droplets with the same refractive index and aspect ratio but different equatorial radii.
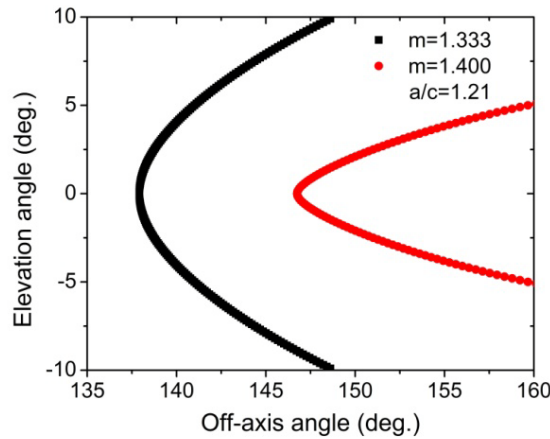

Fig. 4.5.   Primary rainbow fringes for oblate droplets with the same aspect ratio and equatorial radius but different relative refractive indices.
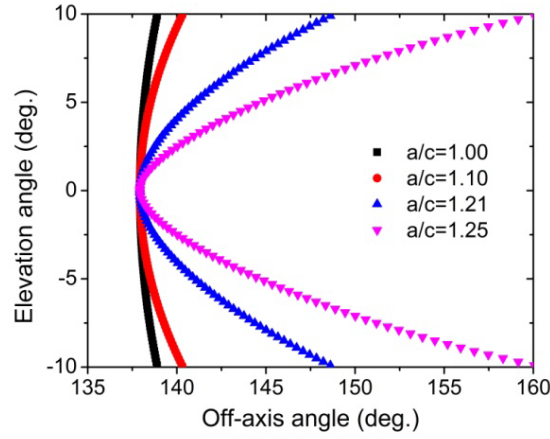
Fig. 4.6.   Primary rainbow fringes for oblate water droplets with different aspect ratios.
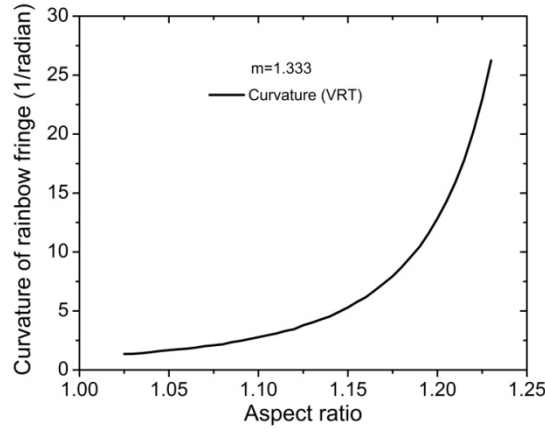

Fig. 4.7.   Curvature of the primary rainbow fringe calculated from VRT simulations for oblate water droplets with different aspect ratios.

In addition, Figure 4.6 shows the primary rainbow fringes for oblate water droplets with aspect ratios 1.00, 1.10, 1.21 and 1.25 respectively. As the aspect ratio increases, the rainbow fringe exhibits an increase of curvature at the apex and a decrease of the opening rate of the rainbow fringe. For all these aspect ratios, a prominent feature is that the location of the rainbow caustic remains unchanged. This is because the cross-section of the oblate droplet remains circular in the equatorial plane so that the second-order refracted rays always exit at the same angular direction in the equatorial plane of the droplet. Further increasing the aspect ratio brings in the rainbow fringe, firstly unfolding and then folding and the appearance of HU fringe as shown in Fig. 4.3. It is demonstrated from the VRT simulations that the rainbow fringe is dependent on the refractive index and aspect ratio but independent on the equatorial radius of an oblate droplet.

Furthermore, the curvatures of the simulated rainbow fringe for oblate water droplets are given in Fig. 4.7. As is the convention for comparison, only the curvature at the apex point of the rainbow fringe is calculated. It can be seen that the curvature increases gradually as the aspect ratio increases. Here, the curvature of the rainbow fringe is shown only for an oblate water droplet with aspect ratio $a/c \leq 1.23$. The curvature of the rainbow fringe provides an avenue to measure the oblateness of droplet according to the relation between the rainbow fringe curvature and the aspect ratio of oblate droplet as shown in Fig. 4.7. To validate the simulations, the curvature of the rainbow fringe obtained from VRT simulation will be compared with that from experiment in Chapter 6.

4.3   Location of cusp caustic of the secondary rainbow

For the secondary rainbow, the location of the cusp caustic can be calculated from the VRT simulation of caustic structures. In addition, the analytical solutions to the cusp location were also given by Marston and Kaduchak (Marston, et al., 1994) based on generalized ray tracing and the symmetry condition that the vertical wave front curvature is infinite at the midpoint of the second chord of the rainbow ray. They are given as:

$$a/c = \left[\left(1 + 2\rho/y\right) \middle/ \left(4\rho^2\right) \right]^{-1/2},$$
(4.3)

$$a/c = \left\{ \left(3y + 2\rho\right) + \left[\left(3y + 2\rho\right)^2 - 16y\rho \right]^{1/2} \right\}^{1/2} \middle/ \left(8y\rho^2\right)^{1/2}.$$
(4.4)

here

$$y = \cos\theta_r - \cos\theta_i / m,$$
(4.5)

and

$$\rho = \cos\theta_r.$$
(4.6)

where ϑ_i and ϑ_r are the incident angle and refractive angle respectively, m the refractive index of the droplet.
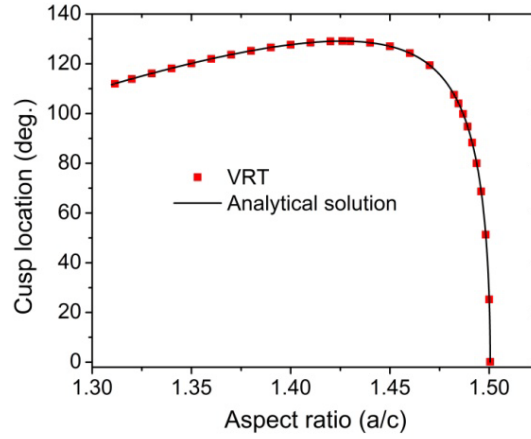
Fig 4.8.   Comparison of the cusp location calculated by VRT simulation and that by the analytical solution in the secondary rainbow region for oblate water droplets with different aspect ratios.
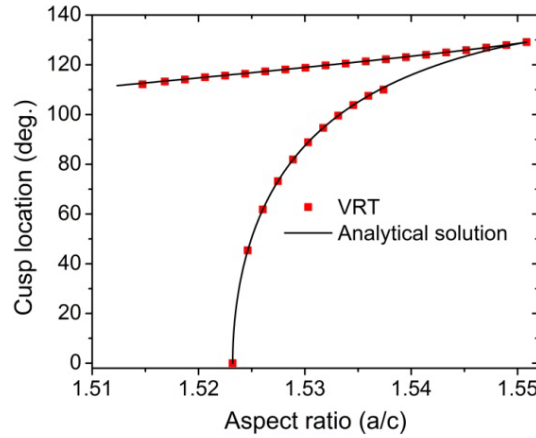

Fig 4.9.   Same parameters as Fig. 4.8, but with different aspect ratio range.

A comparison of the cusp location calculated by the VRT simulation and Marston's analytical solutions Eqs. (4.3)-(4.4) are shown in Figs. 4.8 and 4.9. Figure 4.8 shows the cusp location for $1.311450 \leq a/c \leq 1.500499$. The cusp caustic appears at $\vartheta=111.983^\circ$ for a water droplet having $a/c=1.311450$. As the aspect ratio increases, it shifts to larger scattering angles until it merges with the secondary rainbow caustic at $\vartheta=129.109^\circ$. Then the cusp caustic shifts back to smaller scattering angles and disappears at $\vartheta=0^\circ$ for $a/c=1.500499$. It can be seen from the comparison that the agreement between VRT and the analytical solution is excellent. Figure 4.9 displays the location of two kinds of cusp caustics. For $a/c=1.514736$, the first kind of cusp caustic appears at $\vartheta=112.144^\circ$. For higher aspect ratios, it shifts into larger scattering angles until it merges with the secondary rainbow caustic at $\vartheta=129.109^\circ$ for $a/c=1.551039$.

For *a*/*c*=1.523214 the second kind of cusp caustic appears, which corresponds to the lip event and also merges with the secondary rainbow caustic for *a*/*c*=1.551039 related to the E_6 diffraction catastrophe. As shown by Fig. 4.9, the VRT also agrees with the analytical solution (Marston, et al., 1994) very well.

4.4 Optical caustic structures of the secondary rainbow

Furthermore, the VRT model is used to compute the shape of the rainbow and HU fringes of the secondary rainbow, which are termed structures of optical caustics, because they do not represent interference patterns/fringes. For the third-order rays associated with the secondary rainbow, there is also a revolution (turning point) at the deflection angle of the secondary Descartes ray as with the second-order refracted rays (Yu, et al., 2013). This angle is where the secondary-rainbow fringe forms. The secondary rainbow fringe can be identified from the emergent rays. As with the primary rainbow, the HU caustics are associated with the contribution from skew rays (Kaduchak, et al., 1994), which can also be identified by the VRT model. Considering the beam divergence in the droplet, a sufficient number of rays have to be used to ensure the numerical accuracy. To display the extremely high sensitivity of optical caustics on aspect ratio, the precision of the aspect ratio is given to six decimals. In order to investigate the progression of caustic structures in response to the shape deformation of oblate water droplet in detail, and to apply this information to particle diagnostics, only part of the caustic structure is monitored, i.e. $-10^o \leq \varphi \leq 10^o$. Moreover, total internal reflection, which does not exist for ray tracing in a sphere, has to be accounted for in the VRT model for a spheroid. For example, 72.90% of the incident light rays exit an oblate water droplet with a/c=1.55 while the remaining are totally reflected within the droplet for the order p=3.
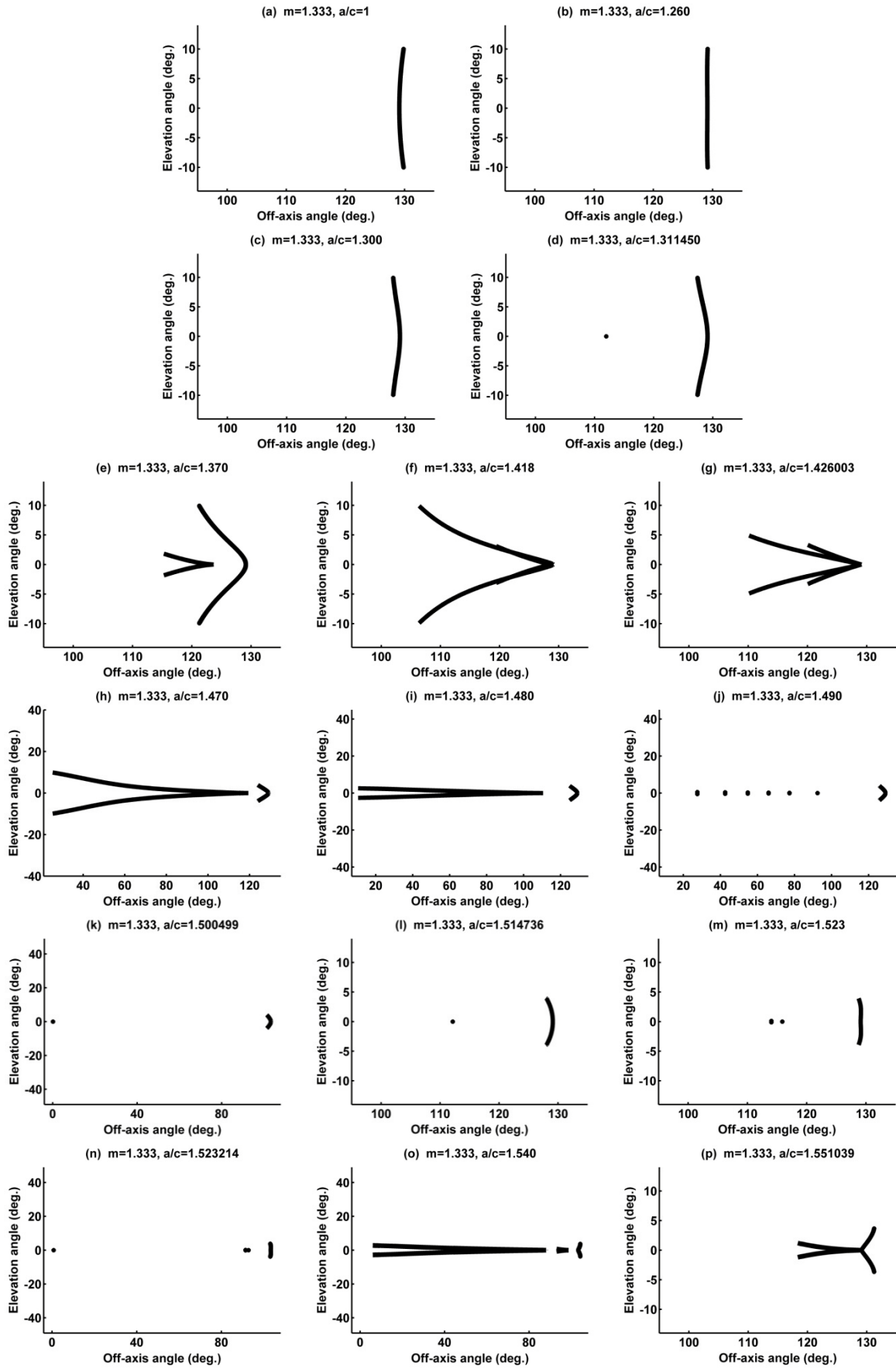
Fig. 4.10.   Evolution of the secondary rainbow fringe and HU fringe as the aspect ratio of an oblate water droplet increases.

In the secondary rainbow region, a sequence of optical caustic structures are first simulated and analyzed systematically for a number of oblate water droplets with refractive index m=1.333, equatorial radius a=100μm, and different aspect ratios (Yu, et al., 2013). Not surprisingly, the evolution of the caustic structures is similar to that observed in the primary rainbow region. Figure 4.10a displays the secondary rainbow fringe for a spherical droplet (a/c=1), which arises due to the fact that the horizontal curvature of outgoing virtual wave front vanishes along the secondary Descartes ray (Kaduchak, et al., 1994). The secondary rainbow fringe exhibits a weak curvature with respect to elevation angle, as with the primary rainbow fringes (see Fig. 4.3). The fringe presents a concave shape bending towards larger scattering angles. Compared to the caustic structures for the primary rainbow (see Figs. 4.3a-4.3e), the secondary rainbow fringe undergoes a gradual change as the aspect ratio increases. For a droplet with aspect ratio a/c=1.260, a prominent fringe is shown in Fig. 4.10b, in which the fringe is almost a straight line vertical to horizontal plane. However this salient fringe is not observed in the primary rainbow region (Yu, et al., 2013). The fringe is similar to the structure of the bows in generalized rainbow pattern observed in experiment (see Fig. 2b in Ref. (Kaduchak, et al., 1994)). However, only the rainbow fringe is shown here without the interference pattern.

As the aspect ratio further increases to a/c=1.300, the secondary rainbow fringe undergoes a curvature reversal (Fig. 4.10c). In contrast to the fringe in Fig. 4.10a, the secondary rainbow fringe takes on a convex shape bending toward smaller scattering angles. As predicted by Marston (Marston, et al., 1994), a cusp caustic appears at ϑ=111.983^o for a/c=1.311450 (Fig. 4.10d). When the aspect ratio increases, the HU fringe unfolds (Fig. 4.10e) and the cusp caustic shifts towards larger scattering angles. For a/c=1.418, the HU fringe overlaps with the secondary rainbow fringe (Fig. 4.10f). For a/c=1.426003, the cusp caustic merges completely with the secondary rainbow caustic at ϑ=129.109^o (Fig. 4.10g) creating the hyperbolic umbilic focal section (HUFS) in the language of catastrophe optics (Berry, et al., 1980), which agrees with experimental observation (Kaduchak, et al., 1994) and theoretical prediction (Marston, et al., 1994). This cusp caustic is due to the vanishing of horizontal and vertical curvatures of wave front at the secondary rainbow angle.

A further increase of the aspect ratio leads to a separation of the secondary rainbow fringe and the HU fringe. The cusp caustic shifts back towards smaller scattering angles and the HU

fringe degenerates gradually. The fringes for a/c=1.470 and a/c=1.480 are shown in Figs. 4.10h and 4.10i respectively. For a/c= 1.490, the HU fringe degenerates more (Fig. 4.10j). Then the cusp caustic disappears at ϑ=0° for a/c=1.500499 (Fig. 4.10k), which also agrees with the theoretical prediction (Marston, et al., 1994). The progression of secondary rainbow fringes and HU fringes are consistent with the shape of the first bow and HU bow of the generalized rainbow patterns observed in experiment (see Fig. 2 in Ref. (Kaduchak, et al., 1994)).

On further increasing the aspect ratio, the caustic structures undergo rapid transitions between events and they are highly sensitive to changes in the aspect ratio. The cusp caustic reappears at ϑ=112.144^o for a/c=1.514736 (Fig. 4.10l) and then shifts into the larger scattering angles, which also agrees with theoretical prediction (Marston, et al., 1994). For a/c=1.523, the major of the secondary rainbow fringe around 129.109° is close to a straight line (Fig. 4.10m). Then the secondary rainbow fringe undergoes a curvature reversal, that is, the convex shape is changed into a concave shape again. For a/c=1.523214, the second kind of cusp caustic occurs at the extreme left of Fig. 4.10n, which corresponds to a lip event (Kaduchak, et al., 1994). For a/c=1.540, the secondary rainbow fringe takes on a concave shape, bending towards larger scattering angles (Fig. 4.10o). And the two HU fringes gradually unfold as shown in Figs. 4.10n and 4.10o. The first HU fringe intersects with the secondary rainbow fringe at the secondary rainbow angle for a/c=1.551039 (Fig. 4.10p), in which the two fringes take on two V shapes. It corresponds to the E_6 diffraction catastrophe ((Kaduchak, et al., 1994) and (Marston, et al., 1994)). Note that the secondary HU fringe is not shown in Fig. 4.10p as it overlaps with the first HU fringe.

It can be seen from VRT simulation that the secondary rainbow fringes become highly sensitive to changes of the aspect ratio of oblate droplet. That is the reason why the precision of the aspect ratio is given to six decimals for some particular ranges. For an oblate droplet with aspect ratio a/c=1.49, the primary and secondary generalized rainbow patterns were shown in Fig. 3a in Ref. (Kaduchak, et al., 1994), in which the secondary rainbow exhibits a concave shape. However, the simulation also shows that the secondary rainbow should take on a convex shape for a/c=1.49 (Fig. 4.10j). This apparent contradiction is simply a manifestation of the very high sensitivity of the caustic structure on the aspect ratio. These measurements were obtained by suspending oblate droplets in an acoustic levitator. Due to the instability of the droplet in the levitator, especially for large aspect ratios, the

experimental uncertainty in aspect ratio is ±0.05 (Kaduchak, et al., 1994), making 1.44≤*a/c*≤1.54. It can be seen from the VRT simulation that the caustic structures for *a/c*=1.44, *a/c*=1.49, and 1.54 are totally different. Even though there are some differences between simulation and observation due to experimental uncertainty, the progression of optical caustic structures in response to the change of droplet aspect ratio is consistent with the change of the first bow and HU bow of the generalized rainbow patterns observed in experiment.
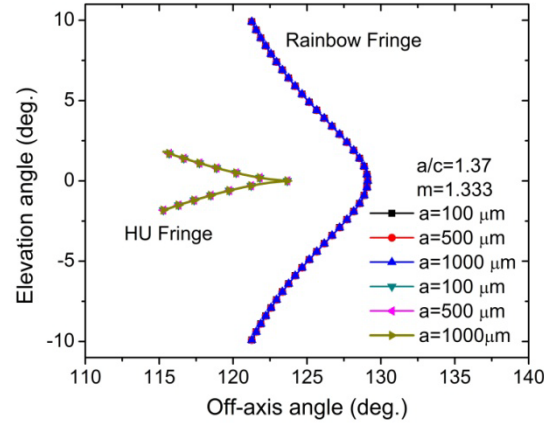

Fig. 4.11.   Secondary rainbow fringes and HU fringes for oblate droplets with the same refractive index and aspect ratio but different equatorial radii.
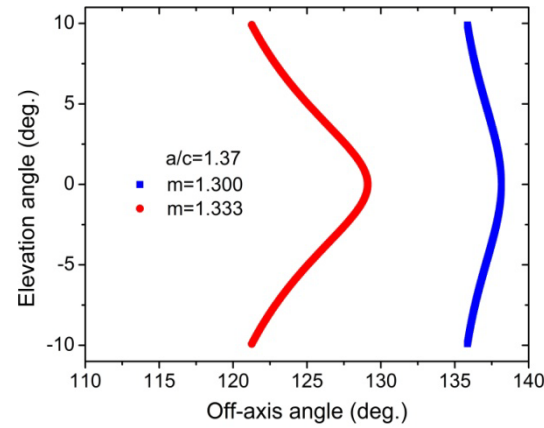

Fig. 4.12.   Secondary rainbow fringes for oblate droplets with the same aspect ratio and equatorial radius but different relative refractive indices.
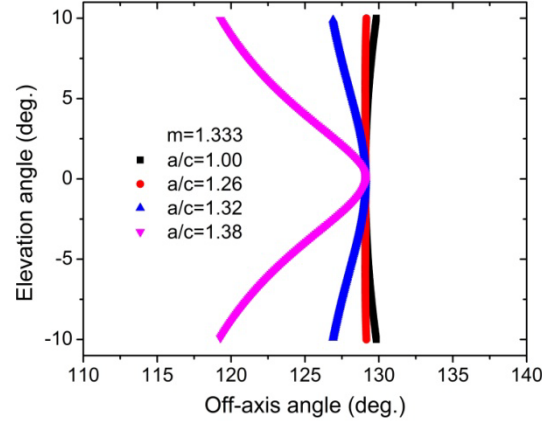
Fig. 4.13.   Secondary rainbow fringes for oblate water droplets with different aspect ratios.
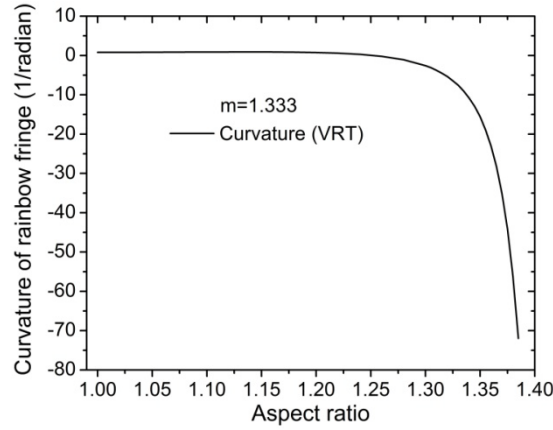

Fig. 4.14.   Curvature of the secondary rainbow fringe calculated from VRT simulations for oblate water droplets with different aspect ratios.

Then Fig. 4.11 shows the secondary rainbow fringes and HU fringes for oblate droplets with the same refractive index (m=1.333) and aspect ratio (a/c=1.37) but different equatorial radii (100μm, 500μm, and 1000μm respectively). As well as the primary rainbow fringe, all the secondary rainbow fringes exhibit the same shape, symmetric about horizontal plane and overlapping completely due to the independence of rainbow fringe on droplet size. Also the HU fringes overlap with each other. The simulations for other types of liquid droplets show that the rainbow fringe shape is dependent on the refractive index of droplet. A comparison of the secondary rainbow fringes for oblate droplets with the same aspect ratio and equatorial radius but different refractive indices is shown in Fig. 4.12. The secondary rainbow fringe for a droplet with m=1.333 is bent much more than that for droplet with

m=1.300. The secondary rainbow caustic appears at 129.11^o for a droplet having *m*=1.333 in the equatorial plane and at 138.16^o for a droplet having *m*=1.300.

Figure 4.13 shows the secondary rainbow fringes for oblate water droplets with aspect ratios 1.00, 1.26, 1.32 and 1.38 respectively. For small aspect ratios, the secondary rainbow fringe takes on a concave shape. As the aspect ratio increases, it exhibits a convex shape and a decrease of the opening rate of the rainbow fringe. However, for all these aspect ratios, a prominent feature is that the location of the secondary rainbow caustic remains unchanged. This is because the cross-section of the oblate droplet remains circular in the equatorial plane so that the third-order refracted rays always exit at the same angular direction in the equatorial plane of the droplet. As well as the primary rainbow fringes, it is shown from the VRT simulations that the secondary rainbow fringe is dependent on the refractive index and aspect ratio but independent on the equatorial radius of an oblate droplet.

Furthermore, the curvature of the secondary rainbow fringe for oblate water droplets is shown in Fig. 4.14. As is the convention for comparison, only the curvature at the apex point of the secondary rainbow fringe is calculated. The curvature is defined as positive for concave shape and as negative for convex shape. It can be seen that the curvature almost keeps the same value for *a/c*≤1.20. As the aspect ratio increases, the curvature deceases rapidly. The curvature of the rainbow fringe also reveals the possibility of measuring the oblateness of droplet according to the relation between the curvature of the rainbow fringe and the aspect ratio of oblate droplet as shown in Fig. 4.14.

4.5 Conclusion

By developing the VRT model, optical caustic structures including the rainbow and HU fringes in the primary rainbow region of light scattering from oblate water droplets are simulated. As a validation of VRT model, the location of cusp caustics are calculated by the VRT model and compared with the analytic solution, by which good agreement is found. Then the evolution of the optical caustic structures (in terms of rainbow fringe and HU fringe) in response to shape deformation of oblate water droplets is investigated by VRT simulations and is found to be consistent with experimental observation. The dependence of the primary rainbow fringe on the refractive index and equatorial radius and the curvature of the rainbow fringe are shown.

Then the VRT model is employed to simulate the optical caustic structures in the secondary rainbow region of oblate droplets. The location of cusp caustic is calculated by use of the VRT simulation and compared with that calculated using analytic solutions, again leading to excellent agreement. For the secondary rainbow, optical caustic structures are first simulated and analyzed systematically according to the VRT model and the evolution process of the optical caustic structures is consistent with the change observed in experiments. The dependence of the secondary rainbow fringe on the refractive index and equatorial radius and the curvature of the rainbow fringe are also shown. It reveals that the optical caustic structures in the secondary rainbow region also can be used to measure the non-sphericity of oblate droplets.

Although the computational efficiency of VRT model is not as high as that of analytical solutions, the VRT model provides a more straightforward and intuitive view of optical caustic structures from oblate droplets. The VRT model can also be used to simulate and predict the optical caustic structures observed in higher-order rainbows. The secondary rainbow fringe, the location and opening rate of the cusp caustic also provide an avenue for non-sphericity measurement of oblate droplets.

Chapter 5   Experimental measurement of light scattering by oblate spheroidal particle in the primary rainbow region

In this chapter, the experimental investigation of light scattering by oblate spheroidal particle in primary rainbow region is shown. The generalized rainbow patterns are shown and discussed in detail. By comparison of experimental result with Airy approximation, the validity of Airy approximation for spheroidal droplets is confirmed.
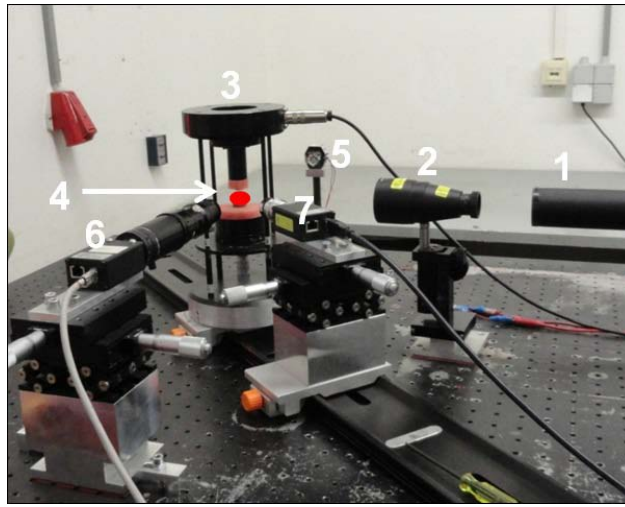
5.1   Experimental setup

Fig. 5.1.   Experimental setup used for the generalized rainbow measurement: (1) He-Ne laser, (2) beam expander, (3) ultrasonic acoustic levitator, (4) suspended droplet, (5) background light, (6) camera 1 focused on the droplet and (7) camera 2 focused at infinity.

The experimental setup used for the generalized rainbow measurement is shown in Fig. 5.1. A linearly polarized Helium-Neon laser beam with wavelength of 632.8 *nm* illuminates a droplet. The typical laser power is 18 mW and the beam diameter ($1/e^2$) is 1mm. The laser beam is expanded by a beam expander so that the light beam is large compared to the droplet size. The degree of linear polarization of the laser is larger than 500:1. An ultrasonic acoustic levitator working at a frequency of 58 kHz is used to suspend the droplet. For taking a photograph of the droplet, a background light (LED) is also used. An image of the droplet is obtained from camera 1 which is focused on the droplet. Camera 2, focused at infinity, is used to record the generalized rainbow patterns. Both cameras are CCD cameras. The sensor size and sensor type of the camera are 1392x1040 pixels and Sony ICX267/AK, progressive

scan CCD respectively. The pixel size of the camera is 4.65x4.65 microns. The ambient temperature is about 296 K.

A standing acoustic wave is generated between a piezoelectrically driven transducer and a curved reflector, resulting in alternate high and low pressure nodes, shown pictorially in Fig. 5.2. The distance between the transducer and the reflector, which can be adjusted by a micrometer screw below the reflector, should equal some multiple half-wavelength of the acoustic wave. Droplets can be levitated in this field and reside just above pressure nodes; the operating principle of the levitator can be found elsewhere ((Tian, et al., 1993) and (Yarin, et al., 1998)). Fig. 5.3 illustrates a levitated water droplet imaged by camera 1. The oblate shape arises from the balance of the gravitational force on the droplet with the radiation pressure exerted by the ultrasonic field. Although the vertical force acting on the droplet is sufficient to carry its weight, the lateral force is typically much weaker and minute movement of the droplet can be observed. This could effectively smooth some features of the rainbow, in particular the ripple structure arising from the interference between reflection (p=0) and second-order refraction (p=2). However, in the present work only the supernumerary bows are utilized and the ripple structure is of secondary importance (Marston, et al., 1984).
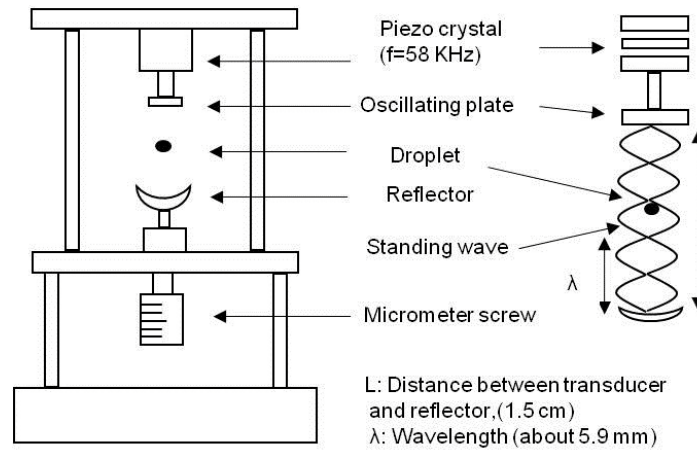

Fig. 5.2.   Ultrasonic acoustic levitator and the standing pressure wave distribution in the resonator.
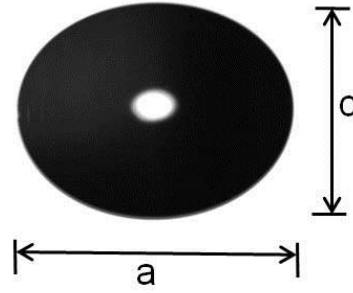
Fig. 5.3.   Photograph of an acoustically levitated droplet.

The droplet diameters will be denoted by a in the horizontal equatorial plane, and by c along the vertical axis of the rotational symmetry as shown in Fig. 5.3. The aspect ratio (defined by a/c) can be varied by adjusting the sound pressure level of the levitator and/or the distance between the transducer and the reflector, which effectively changes the pressure exerted on the droplet surface. To calibrate the magnification factor of the lens system, one records an image of a grid positioned between the transducer and reflector. The diameter of the grid is 21 mm. The smallest square of the grid is 0.1 *mm* X *0.1 mm*. Subsequently, the relation between the pixel number and the droplet size is found.

5.2 Generalized rainbow patterns from water droplets

The generalized rainbow patterns including the fold rainbow, transverse cusp caustics and the hyperbolic umbilic catastrophe for water droplets are shown in following. The scattering patterns were taken by camera 2 for randomly and linearly polarized illumination from a He-Ne laser with a wavelength of 632.8 *nm*. A receiving lens with the focal length 60 *mm* is used. This camera was focused at infinity so that the pattern recorded was equivalent to that in the far field (Marston, et al., 1984), that is, the CCD sensor is placed at the position of the focal plane of the receiving lens. Horizontal and vertical coordinates in each photograph are more or less linearly related to the horizontal and vertical scattering angles ϑ and ϕ, respectively. The field of view of the camera is approximately $137.3^{\circ}<\vartheta<143.5^{\circ}$ and $2.3^{\circ}<\phi<2.3^{\circ}$.
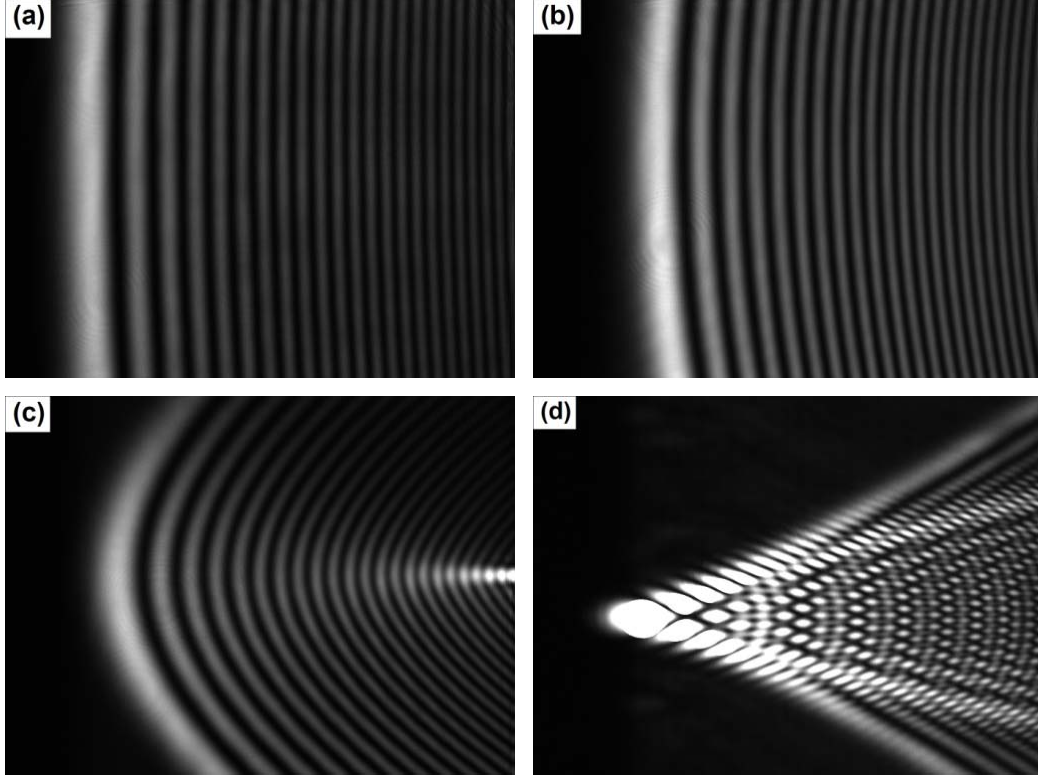
Fig. 5.4.   Generalized rainbow patterns from spheroidal water droplets in order of increasing aspect ratio: (a) *a/c*=1.02; (b) *a/c*=1.15; (c) *a/c*=1.21 and (d) *a/c*=1.32.

Light scattered from the water droplet in the vicinity of the primary rainbow region has been observed to contain a varity of characteristic diffraction patterns. Figure 5.4a shows the scattering pattern from a slightly non-spherical droplet having *a*=1.58*mm* and *a/c*=1.02. The fringes are almost straight in the viewed region. Figures 5.4b-c are patterns from spheroidal droplets, which are a generalization of primary rainbow formed by a spherical droplet. These generalized rainbow patterns include transverse cusp caustic, hyperbolic umbilic, and other catastrophes in the language of catastrophe optics (Berry, et al., 1980). Figure 5.4b shows the generalized pattern for spheroidal droplet with *a*=1.77 *mm* and *a/c*=1.15. Comparing with Fig. 5.4a, an obvious phenomenon is that the fringes are curved, arising from the non-sphericity of droplet. The pattern from a spheroidal droplet having *a*=1.76 *mm* and *a/c*=1.21 is shown in Fig. 5.4c. The fringes are curved even stronger and a distinct cusp point arises on the right side of the pattern. The cusp point arises from the interference of the two light rays in the horizontal (equatorial) plane and two skew light rays which do not lie in the horizontal plane on entering the droplet, but are confined to the horizontal direction upon exiting the droplet (Marston, et al., 1984). As the ratio is further increased, the cusp shifts to the left

68

towards the smaller θ until it merges with the rainbow caustic. The resulting pattern is that of a hyperbolic umbilic focal section, which means the four light rays come out with the same angle, i.e. at the rainbow angle. Nye gave the critical ratio value for such hyperbolic umbilic section as a/c=[3m^2/(m^2-1)]$^{1/2}$ (Nye, 1984). It is approximately 1.310 for the refractive index m=1.333. Figure 5.4d shows the D_4^+ pattern from a droplet having a=1.71 mm and a/c=1.318. It can be seen that the observed value of a/c agrees with the theoretical prediction very well. When the ratio is further increased, other characteristic catastrosphe diffraction patterns can be also obtained. It is noticed that the cusp reappears and shifts back towards larger ϑ. Here attention has only been paid to droplets with small aspect ratios, because the generalized patterns for small aspect ratios can be used to measure the refractive index and the equatorial diameter as shown in the following sections.

5.3   Validation of Airy approximation for spheroidal droplet

The Airy approximation of the rainbow (Airy, 1838) provides the scattering intensity in the areas of the rainbow as a function of scattering angle, is valid for a spherical particle, and offers a greatly simplified computation compared with the Lorenz-Mie theory, especially for large particles. Nevertheless, Lorenz-Mie computations are nowadays feasible for large spherical particles and offer a method of validation of the Airy approximation. In Ref. (Wang, et al., 1991) for instance, agreement between the two approaches had been shown with increasing refractive index, even for very small particles.

For non-spherical particles, rigorous theories and most numerical approaches are feasible only for small sizes, i.e. several tens of wavelengths (Ren, et al., 2011). Thus, a comparison between Airy approximation and rigorous computations are no longer available for large non-spherical particles. On the other hand, one can compare experimental results with Airy predications to explore to what extent the Airy approximation is valid for large spheroidal particles.

In a gravitational field, and taking into account the surface tension, a droplet suspended in an acoustic levitator can be approximated by an oblate spheroid if the size parameter is not too large (Yarin, et al., 1998). Therefore, attention is henceforth focused on an oblate spheroidal droplet. An oblate spheroid is a surface of revolution obtained by rotating an ellipse about its minor axis. In the horizontal equatorial plane the section of the oblate spheroid is a circle. So, the rays transmitting on the equatorial plane will be confined to this

same plane. One can imagine the intensity distribution in this plane could be described by Airy approximation. As shown in Section 2.3.2, it is the perpendicular polarized component which dominates in the pattern and our calculations are restricted to this component. The scattering intensity evaluated by Airy approximation is given by ((van de Hulst, 1981) (Wang, et al., 1991)):

$$I = \varepsilon_1^2 \left[81 \big/ \left(16\pi^2 h^4 \right) \right]^{1/6} \times \sin\left(\theta_{irg} \right) \alpha^{7/3} f^2(z) \big/ \cos\left(\theta_{rg} \right) \tag{5.1}$$

here $f(z)$ is the Airy integral:

$$f(z) = \int_0^\infty \cos\left[\pi\left(zt - t^3 \right) \big/ 2 \right] \ dt \tag{5.2}$$

The variables and parameters in Eqs. (5.1) and (5.2) are defined by:

$$\alpha = \pi a / \lambda; \quad z = (-q)\left[12 \big/ \left(h\pi^2 \right) \right]^{1/3} \alpha^{2/3} \left(\theta - \theta_{rg} \right);$$
$$h = 3\left(p^2 - m^2 \right)\left(p^2 - 1 \right) \big/ \left(m^2 - 1 \right);$$
$$\varepsilon_1 = \left(1 - r_1^2 \right)\left(r_1 \right)^{(p-1)}, \quad p \geq 2; \tag{5.3}$$
$$r_1 = \frac{\cos\theta_{irg} - m\cos\theta_{rrg}}{\cos\theta_{irg} + m\cos\theta_{rrg}}.$$

where α is the dimensionless size parameter, q an integral equaling to +1 or -1, whose physical meaning can be found in Ref. (Yu, et al., 2009), ϑ_{irg} the incident angle for rainbow ray, ϑ_{rrg} the refractive angle for rainbow ray. ϑ_{rg} and ϑ are the rainbow angle and scattering angle respectively.

To simulate the intensity distribution using Airy approximation, one only need to know the size parameter a in the equatorial plane and the relative refractive index m of the droplet. Figure 5.5a shows the comparison of intensity distribution calculated by Airy approximation and that by experiment for a nearly spherical water droplet with a=1.58 *mm* and a/c=1.02. The intensity distribution shown in this figure is that obtained on the equatorial plane. For comparison purposes, the two results have been normalized to the same maximum value. The Airy approximation agrees well with the experimental result in the scattering angle region 137.5°<ϑ<140°. Figure 5.5b shows the comparison for an oblate spheroidal having *a*=1.76 *mm* and *a/c*=1.21. Good agreement is also found.
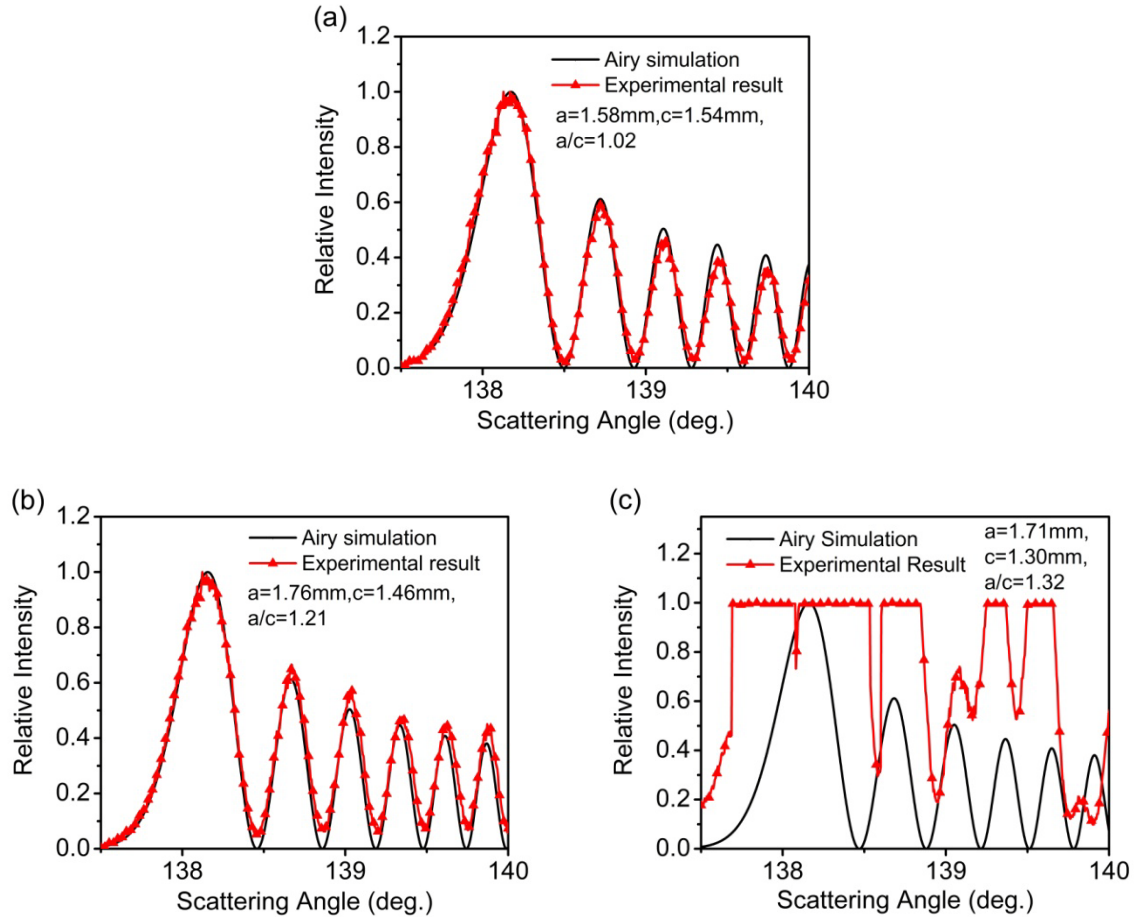
Fig. 5.5. Comparison of the intensity distribution calculated by Airy approximation and that by experiment for water droplet: (a) *a*=1.58*mm* and *a/c*=1.02; (b) *a*=1.76 *mm* and *a/c*=1.21 and (c) *a*=1.71 *mm* and *a/c*=1.32.

However, for large aspect ratios, other skew rays enter the rainbow region, the hyperbolic umblic arises, as shown in Fig. 5.4d. Figure 5.5c shows the comparison for an oblate spheroidal droplet with *a*=1.71 *mm* and *a/c*=1.32. The Airy approximation no longer compares well with experimental results. The additional caustic structures lead to a saturation of measured intensity from the camera. In summary, comparison of the experimental data of spheroidal droplet scattering with Airy approximation reveals that in many respects the near-spherical particles behave like spheres when the measurements are performed in the horizontal scattering plane in which the drops display circular cross sections. So, the Airy approximation appears to offer a reliable avenue for characterising spheroidal particles with smaller aspect ratios.

5.4 Conclusion

In an experiment, an ultrasonic acoustic levitator was used to levitate a water droplet whose shape could be varied between spherical and spheroidal. The light scattering patterns (generalized rainbow patterns) in the primary rainbow region from spheroidal water droplets are detected. The recorded generalized rainbow patterns include transverse cusp caustic, hyperbolic umbilic, and other catastrophes. The intensity distribution of the generalized rainbow patterns in the horizontal equatorial plane has been compared with the Airy simulation. For spheroidal water droplets having 0.80 *mm<a<*2.00 *mm,* and *a/c<*1.28, the experimental result matches the Airy approximation very well, at least in the scattering angle range 137.5^{o} to 140°. This suggests that the rainbow patterns generated from those droplets can be used for characterizing particle, which will be shown in Chapter 6.

Chapter 6   Spheroidal droplet measurement from generalized rainbow patterns

Based on the generalized rainbow patterns and Airy approximation, the refractive index and equatorial diameter of spheroidal water droplets can be determined. It is shown that absolute error of the refractive index is less than 0.5×10^{-4} and of the droplet diameter 5%. Furthermore, the relation between the curvature of the rainbow fringes and the aspect ratio of spheroidal water droplets is shown. Therefore, the aspect ratio of spheroidal droplets can be inferred from the corresponding generalized rainbow patterns with relative errors lying between -1% and 1%.

6.1   Inversion of refractive index of droplet

The first extreme value of the Airy approximation is denoted ϑ_1. The angle for the second maximum in the Airy approximation is denoted ϑ_2. In order to obtain the value ϑ_1 and ϑ_2 from the experimental data, the intensity curve is filtered to remove the ripple structure. A Gaussian low-pass filter was used for this purpose. The filtered experimental result is shown in Fig. 6.1. It is obvious that the angular positions of first two extreme values agree very well. The values of ϑ_1 and ϑ_2 found experimentally can then be used to calculate the relative refractive index and size parameter.
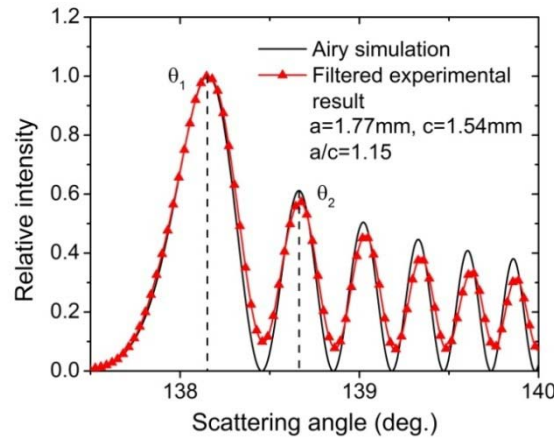

Fig. 6.1.   Comparison of intensity distribution calculated by Airy approximation with the filtered experimental result for a water droplet: *a*=1.77 *mm* and *a/c*=1.15.

According to Airy approximation given in Chapter 2, the relation between the rainbow angles, ϑ_1, and ϑ_2 is given by:

$$\theta_{rg} = \left(\theta_1 - C\theta_2\right)/(1-C) \tag{6.1}$$

where C is a constant defined by $C = \alpha_1/\alpha_2$, ($\alpha_1 = 1.0874$, $\alpha_2 = 3.4668$). The parameters α_1 and α_2 can be calculated from the Airy integral (van de Hulst, 1981). After knowing ϑ_1 and ϑ_2, the rainbow angle can be calculated and then the refractive index can be inferred. Based on geometric optics, the relation between the rainbow angle and the refractive index is given as (Yu, et al., 2013):

$$\theta_{rg} = \pi + 2\cos^{-1}\left(\frac{m_{GRP}^2 - 1}{3}\right)^{\frac{1}{2}} - 4\cos^{-1}\left(\frac{4\left(m_{GRP}^2 - 1\right)}{3m_{GRP}^2}\right)^{\frac{1}{2}} \tag{6.2}$$

To differentiate the relative refractive index of a pure water droplet and that calculated from the rainbow pattern, they are denoted as m and m_{GRP} respectively. Then the error Δ_m of refractive index is defined as:
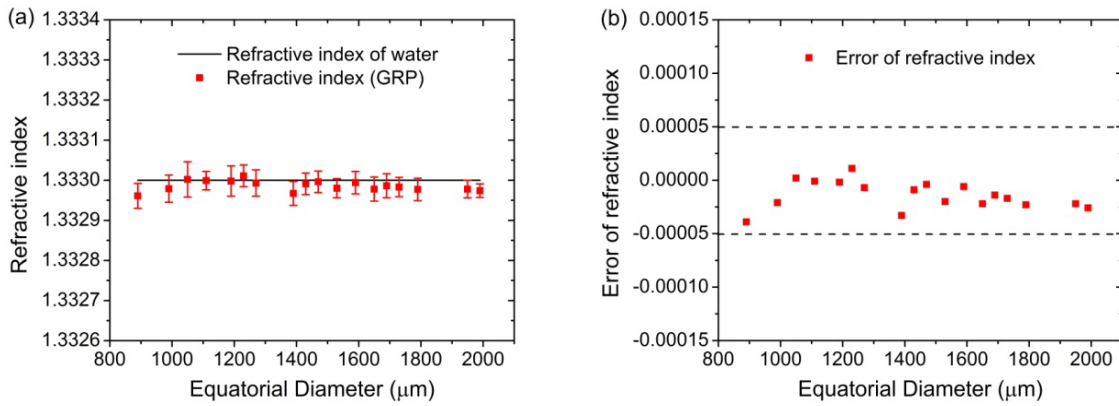
$$\Delta_m = m_{GRP} - m \tag{6.3}$$

Fig. 6.2:   (a) Refractive index of pure water droplet and that calculated from the corresponding generalized rainbow patterns. (b) Errors of refractive indices inverted from the corresponding generalized rainbow patterns.

Based on Eqs. (6.1)-(6.2), the relative refractive indices calculated from the relevant generalized rainbow patterns are shown in Fig. 6.2a, in which the refractive indices are shown with error bars corresponding to one standard deviation. It can be seen that the inversion results of refractive index are consistent with that of pure water (m=1.333 at 632.8 nm). Water droplets have been studied only in the range 0.80-2.00 mm and aspect ratios

smaller than 1.28, since larger and smaller droplets are not held stable in the acoustic levitator. Figure 6.2b shows the error of relative refractive index inverted from the corresponding generalized rainbow patterns. It can be seen that absolute error is smaller than 0.5×10^{-4} (Yu, et al., 2013).

6.2   Inversion of droplet size

The diameter a_{GRP} in the equatorial plane can be calculated by (Yu, et al., 2013):

$$a_{GRP} = \frac{\lambda}{4} \left[\left(\frac{3\left(4 - m_{GRP}^2\right)^{1/2}}{\left(m_{GRP}^2 - 1\right)^{3/2}} \right)^{1/2} \left(\frac{\alpha_1 - \alpha_2}{\theta_1 - \theta_2} \right)^{3/2} \right] \tag{6.4}$$

For evaluating the precision of a_{GRP}, the relative error Δ_a of diameter is also defined:

$$\Delta_a = \left(a_{GRP} - a\right) \times 100 / a \tag{6.5}$$

where α_1, α_1, ϑ_1, ϑ_2, and λ have been defined above. a is the diameter of droplet in the equatorial plane, which for purposes of evaluating the precision is measured by direct imaging with camera 1. The uncertainty of this diameter estimation is about four pixels, which for the current measurements corresponds to approximately 9.81 μm.
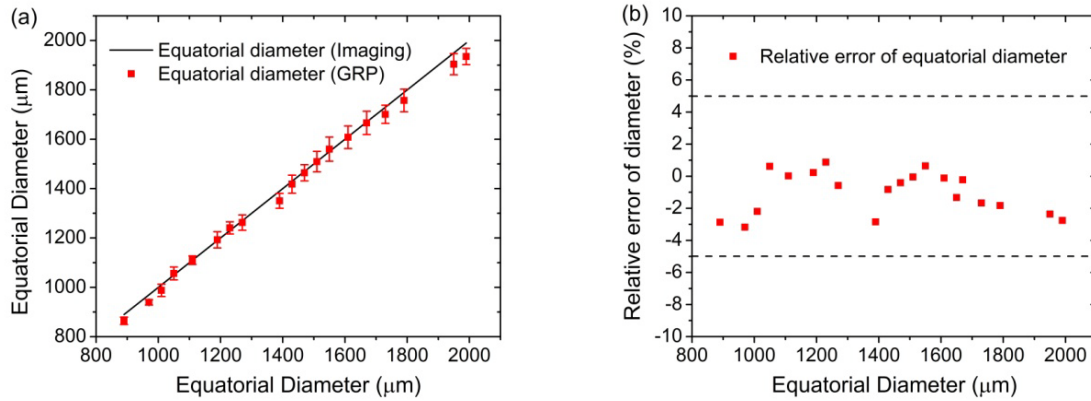

Fig. 6.3:   (a) Water droplet diameters in the equatorial plane measured by imaging and that calculated from the corresponding generalized rainbow patterns. (b) Relative errors of droplet diameters inverted from the corresponding generalized rainbow patterns.

Figure 6.3a shows the water droplet diameters in the equatorial plane calculated by Eq. (6.4), in which the droplet diameters are also shown with error bars relevant to one standard deviation. The equatorial diameter calculated from the corresponding rainbow pattern matches well the values obtained by imaging with the camera. The relative error calculated

by Eq. (6.5) for equatorial diameter associated with the rainbow is shown in Fig. 6.3b. It can be seen that the absolute relative error is less than 5%; hence very reliable droplet diameter estimation can be obtained from the corresponding generalized rainbow patterns.

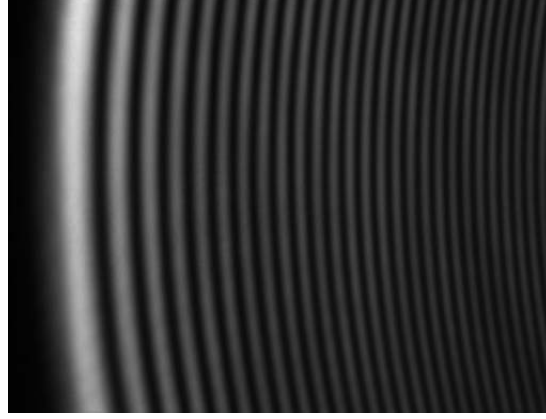## 6.3 Relationship between droplet aspect ratio and rainbow pattern and inversion of droplet aspect ratio

Fig. 6.4.   A generalized rainbow pattern for a spheroidal water droplet with a=1.79mm, c=1.61mm, a/c=1.11.
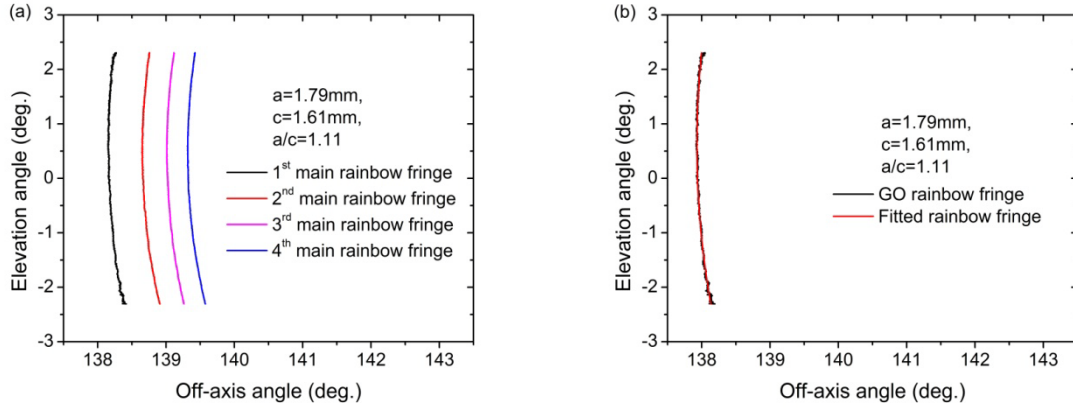
Fig. 6.5.   Rainbow fringes for the generalized rainbow pattern as shown in Fig. 6.4.

A generalized rainbow pattern for a spheroidal water droplet with a/c=1.11 is shown in Fig. 6.4. The change of the bows' shape of the generalized rainbow pattern in response to the droplet deformation reveals the possibility of measuring the oblateness of the droplets from the curvature of the corresponding rainbow fringes as shown in Fig. 5.4. Then the bow's shape (in terms of main rainbow fringe) is calculated for the generalized rainbow pattern. Figure 6.5a shows the first four main rainbow fringes for the generalized rainbow pattern as shown in Fig. 6.4. Then the geometrical optical (GO) rainbow fringe can be calculated

according to Eq. (6.1). It can be seen from Fig. 6.5b that the GO rainbow fringe is not smooth due to the minute movement of the droplet. To calculate the curvature of the GO rainbow fringe, the curvature is fitted using the third-order polynomial. A smooth GO rainbow fringe is given in Fig. 6.5b. For consistency with Chapter 4, the GO rainbow fringe calculated from the generalized rainbow pattern is also called the rainbow fringe in the following discussion.
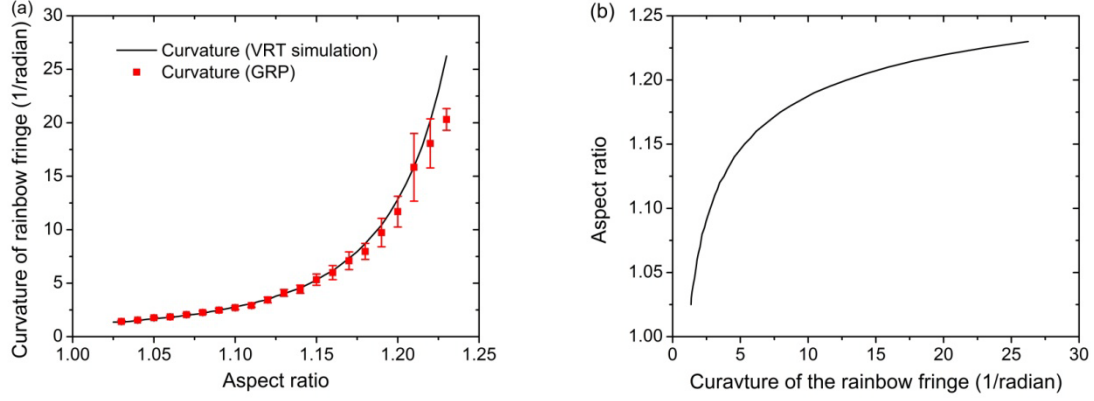

Fig. 6.6:   (a) Comparison the curvatures of the rainbow fringes calculated from VRT simulations and that from generalized rainbow patterns for water droplets. (b) The relation between aspect ratios of water droplets and curvatures of the corresponding rainbow fringes calculated from VRT simulations.
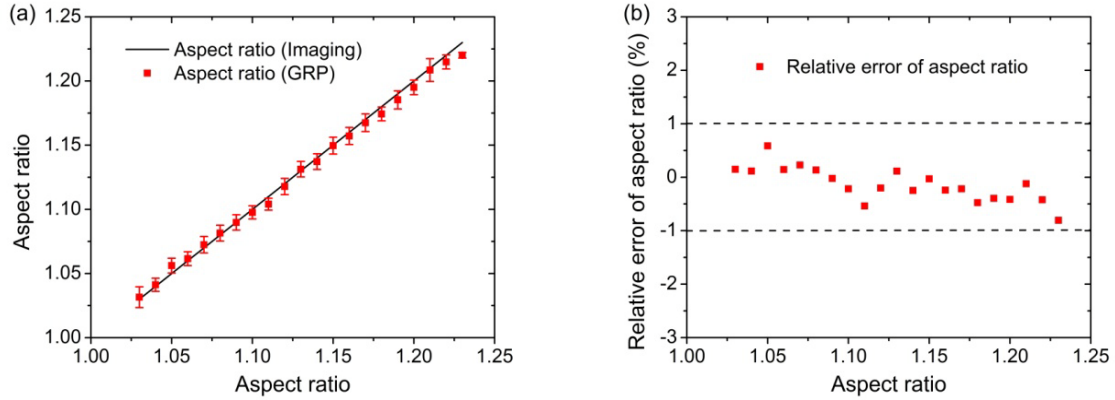
Fig. 6.7:   (a) Comparison of water droplet aspect ratios observed from direct imaging and that inverted from the corresponding generalized rainbow patterns. (b) Relative errors of inverted aspect ratios from the corresponding generalized rainbow patterns.

Then, the curvature of the rainbow fringe can be calculated. On the other hand, the curvature of the rainbow fringe from the VRT simulation is shown in Fig. 4.7. Therefore, a comparison of the curvature of rainbow fringes obtained from a vector ray tracing (VRT)

simulation and that from experiments for water droplets is shown in Fig. 6.6a. As is the convention for comparison, only the curvature at the apex point of the rainbow fringe is calculated. The curvatures calculated from the experimental rainbow patterns are shown with error bars corresponding to one standard deviation. It can be seen that the agreement between the VRT model and measurement is excellent at most aspect ratios: most deviations are within the experimental uncertainty. Attention has to be paid to the fact that, for large aspect ratio (e.g. $a/c>1.23$), the droplet vibrates significantly in the levitator and the relevant generalized rainbow pattern becomes highly instable and blurry. It is difficult to distinguish the rainbow fringe without using a high- speed camera. For this reason the curvature of the rainbow fringes are shown only for droplets with aspect ratio $a/c\leq1.23$.

Figure 6.6b plots the droplet aspect ratio against the curvature of the corresponding rainbow fringes simulated by VRT model, which reveals that the aspect ratio of droplet can be calculated based on the curvature of the rainbow fringe measured from experiment and relation between the aspect ratio and curvature shown in Fig. 6.6b. For a measured generalized rainbow pattern, the corresponding rainbow fringe can be calculated; then the curvature of the rainbow fringe can be obtained; finally the aspect ratio of the relevant water droplet can be inverted according to Fig. 6.6b.

Based on the relation between the aspect ratio and the curvature of rainbow fringe (Fig. 6.6b), the aspect ratio (r_{GRP}) of the water droplet can be inverted from the corresponding generalized rainbow patterns and is compared with observed value ($r_{Imaging}$) from the directly recorded droplet image. Figure 6.7a gives such a comparison. The aspect ratios inverted from the generalized rainbow patterns are also shown with error bars relevant to one standard deviation. It reveals that the inverted droplet aspect ratios agree well with that from direct imaging. To evaluate the accuracy of inverted aspect ratio, the relative errors in percentage (($\Delta=(\ r_{GRP}-r_{Imaging})\times100/\ r_{Imaging}$) are shown in Fig. 6.7b. The relative errors lie between -1% and 1%, which indicates good measurement accuracy of droplet non-sphericity (in terms of aspect ratio) from the corresponding generalized rainbow patterns.

6.4 Conclusion

According to the generalized rainbow patterns and Airy approximation, the refractive index and equatorial diameter of water droplets can be inverted from the corresponding generalized rainbow patterns. Comparison of the refractive indices inverted from the

generalized rainbow patterns with that of pure water shows good agreement with absolute errors less than 0.5×10^{-4}. The water droplet diameters in the horizontal equatorial plane are calculated from the corresponding generalized rainbow patterns and compared to that measured by direct imaging. It is shown that the relative errors of droplet diameters associated with the generalized rainbow patterns lie between -5% and 5%; hence reliable diameter estimations of droplets can be obtained from the relevant generalized rainbow patterns. The curvatures of simulated rainbow fringes are compared with observed ones from the corresponding generalized rainbow patterns, in which good agreement is also shown. Since for a given type of droplet, the curvatures of the rainbow fringes are only a function of the aspect ratios, the non-sphericity (in terms of aspect ratio) of water droplets are inferred from the relevant generalized rainbow patterns. The relative errors of aspect ratios calculated from the generalized rainbow pattern lie between -1% and 1%. Accordingly, the complete information of a spheroidal water droplet in terms of geometric and optical properties are obtained.

Chapter 7   Preliminary investigation of tilted spheroidal droplet

In the following chapter, the evolution of the optical caustic structures (in terms of rainbow fringe) in response to the change of tilt angle is studied based on vector ray tracing. The generalized rainbow pattern for a tilted spheroidal droplet is shown.

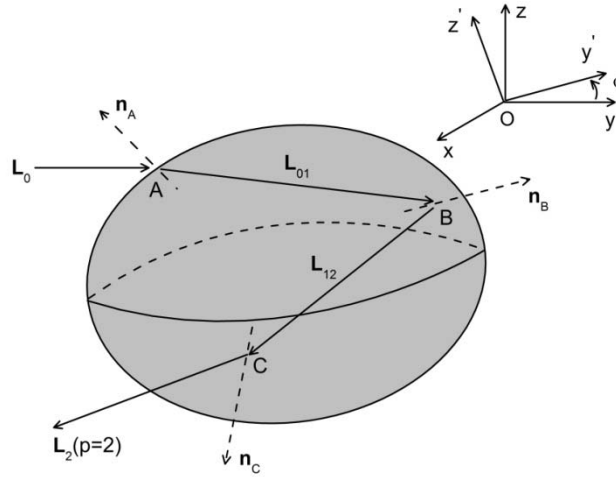## 7.1 Vector ray tracing model for a tilted spheroidal droplet

Fig. 7.1.   VRT model for tilted a spheroidal droplet.

The surface of a spheroidal particle is a closed quadric surface that is a three dimensional analogue of an ellipse. The standard equation of an ellipsoid centered at the origin of $x^{'} y^{'} z^{'}$ coordinate system (see Fig. 7.1) is given by:

$$\frac{\left(x^{'}\right)^2}{a^2} + \frac{\left(y^{'}\right)^2}{b^2} + \frac{\left(z^{'}\right)^2}{c^2} = 1. \tag{7.1}$$

where a, b and c are called the semi-principal axes aligned along the coordinate axes.

Suppose the spheroid is tilted relative to light beam direction, that is, the spheroid is rotated counterclockwise by an angle φ around the x-axis (see Fig. 7.1). The transform of $x^{'} y^{'} z^{'}$ and xyz coordinates is given as:

$$\begin{bmatrix} x^{'} \\ y^{'} \\ z^{'} \end{bmatrix} = \begin{bmatrix} 1 & 0 & 0 \\ 0 & \cos\varphi & \sin\varphi \\ 0 & -\sin\varphi & \cos\varphi \end{bmatrix} \begin{bmatrix} x \\ y \\ z \end{bmatrix} \tag{7.2}$$

Combining Eqs. (B2) and (B1), one can obtain the function for the tilted spheroid in xyz coordinates:

$$Ax^2 + By^2 + Cz^2 + Dyz - 1 = 0, \tag{7.3}$$

here

$$A = \frac{1}{a^2}, \qquad\qquad B = \frac{\cos^2 \varphi}{b^2} + \frac{\sin^2 \varphi}{c^2},$$

$$C = \frac{\sin^2 \varphi}{b^2} + \frac{\cos^2 \varphi}{c^2}, \quad D = 2\sin\varphi\cos\varphi\left(\frac{1}{b^2} - \frac{1}{c^2}\right). \tag{7.4}$$

Equations (7.3)-(7.4) can be used for a spheroid which is rotated about the x-axis clockwise. In that case, the angle φ is set to negative.

Suppose the directional vector of incident light ray is parallel to the x-axis (see Fig. 7.1). Then the refracted ray (L_{01}) at point A, the reflection ray (L_{12}) at point B, and the refracted ray (L_2) at point C can be calculated according to Eqs. (3.9)-(3.11). The definition of the scattering angles θ and φ remain the same as in Eqs. (3.13) and (3.14). The calculation of the intersection points of the light ray inside the spheroid and the spheroidal surface is given in Appendix A. According to the vector ray tracing formula and intersection of a light ray with the surface of a tilted spheroid, one can trace the light ray transmission from the spheroid.

7.2   Optical caustic structures for tilted spheroidal droplet

The rainbow fringe and HU fringe for an aligned spheroidal droplet have been given in Chapter 4 based on VRT. The principle of computing the fringes for a tilted spheroidal droplet is the same as that for a spheroidal droplet aligned with the *xyz* coordinate system. Again it must be emphasized that the term fringe will refer to structures of optical caustics, not to interference patterns/phenomena.

A comparison of the fringes for the aligned spheroidal droplets with refractive index *m*=1.333 and that for tilted spheroidal droplets with different tilt angles are shown in Figs. 7.2-7.4. For small tilt angles (φ=2°), the rainbow fringes for different droplets and aspect ratios (1.05, 1.10, 1.15, and 1.23) are all very similar (see Fig 7.2). For φ=5° and an aspect ratio a/c≲1.10 (see Fig. 7.3a and 3b), the fringes for the aligned droplet and tilted droplet almost overlap. However, for larger aspect ratios, the fringes for tilted spheroidal droplets deviate significantly from that for the aligned spheroidal droplets, as shown in Fig. 7.3c and 7.3d. As the tilt angle increases, the rainbow fringe for tilted droplets also rotates in the same direction. In contrast to the symmetry of fringes for aligned spheroidal droplets, the rainbow fringes for tilted spheroidal droplets become asymmetrical about the horizontal plane (see Fig. 7.4). Furthermore, the geometrical rainbow angle, i.e. the most left point of

82

the rainbow fringe, shifts to the left side as the tilt angle increases (see Fig. 7.4). However, for droplets with small aspect ratios, the difference of rainbow fringes for tilted droplet to those for aligned droplets is not large (see Figs. 7.2a, 7.3a, and 7.4a). This is because the spheroid with small aspect ratio is close to a spherical shape.

In summary, the rainbow fringes are tilted counterclockwise as the spheroidal droplet is tilted counterclockwise and vice versa. And the geometrical rainbow angle shifts to the left side when the spheroidal droplet is tilted counterclockwise. The changes of the fringes depend on the aspect ratio and tilt angle.
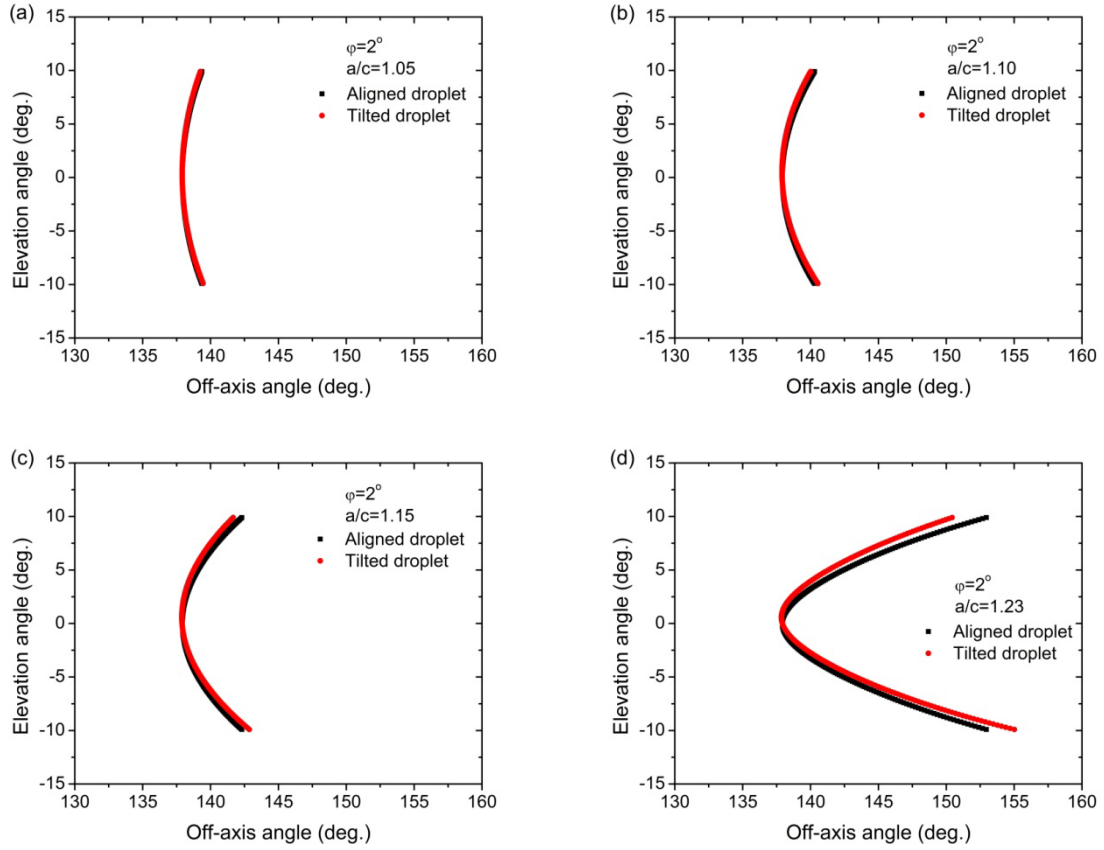

Fig. 7.2.   Comparison of the rainbow fringe for aligned droplets and tilted droplets with $\varphi=2^{o}$: (a) a/c=1.05, (b) a/c=1.10, (c) a/c=1.15, and (d) a/c=1.23.
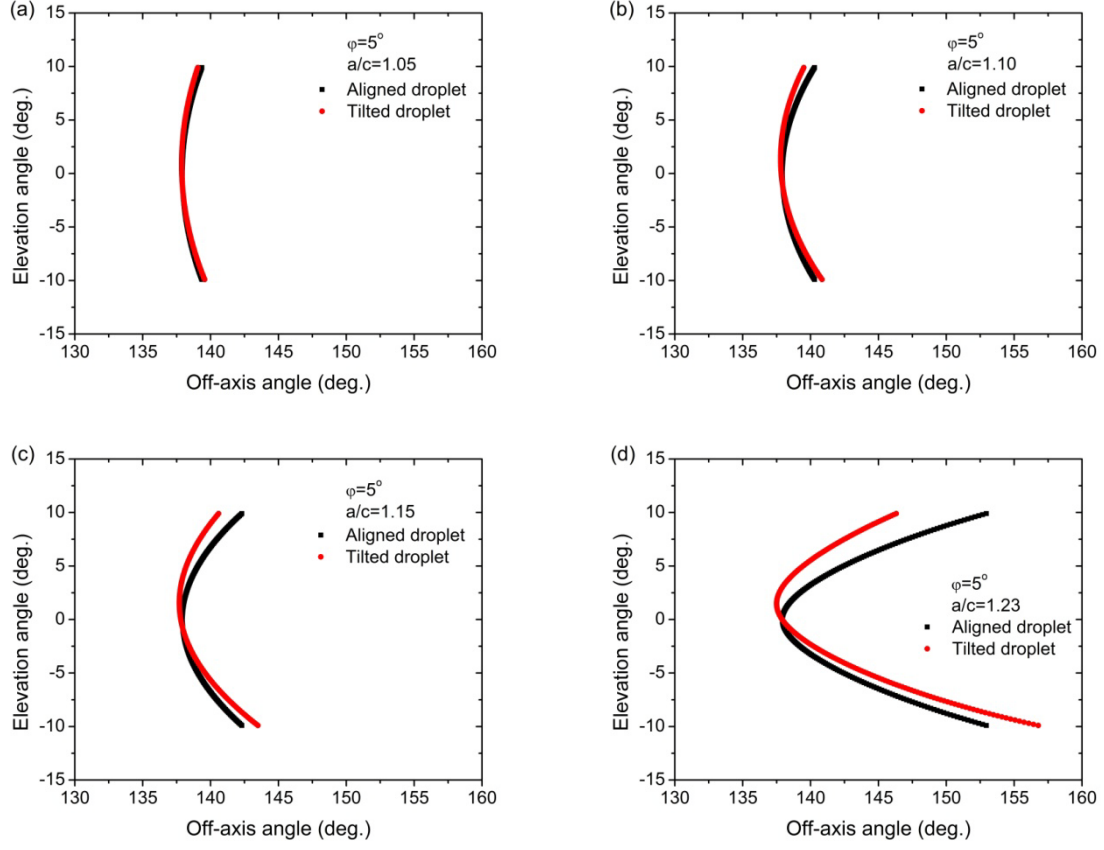
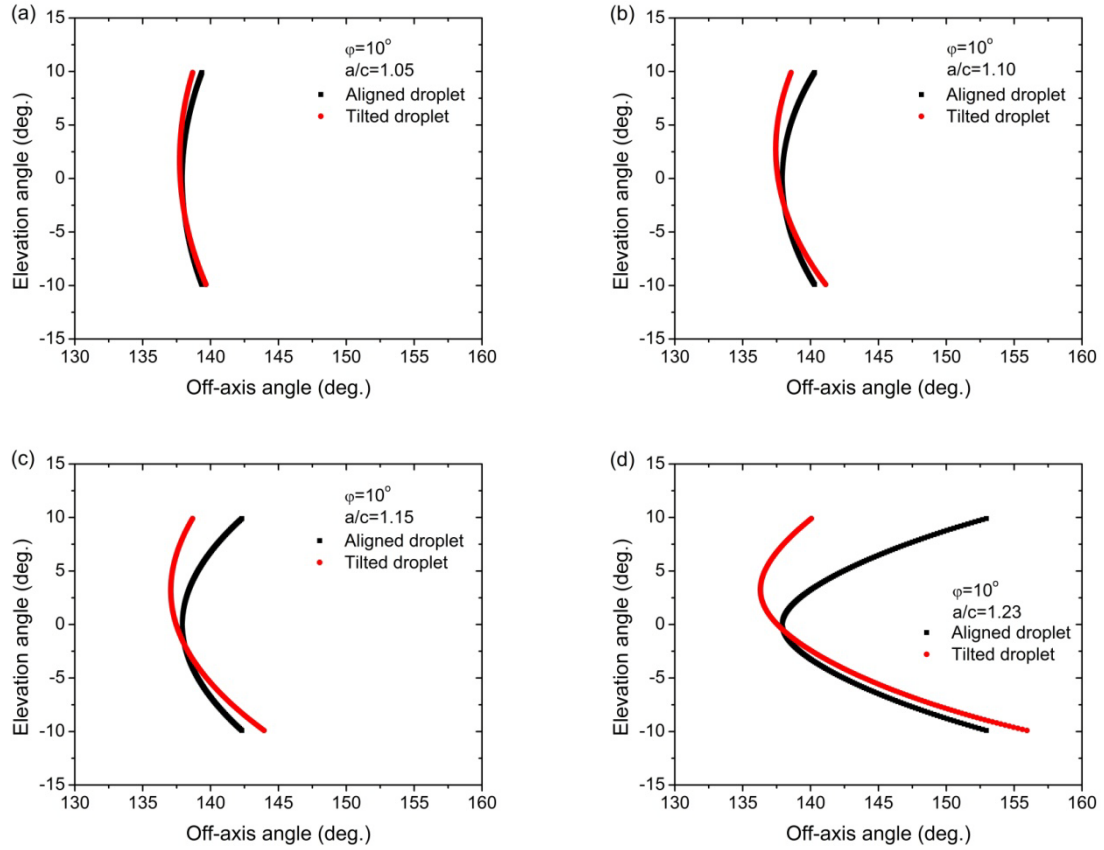Fig. 7.3.   Same parameters as Fig. 7.2, but with φ=5°.

Fig. 7.4.   Same parameters as Fig. 7.2, but with φ=10°.
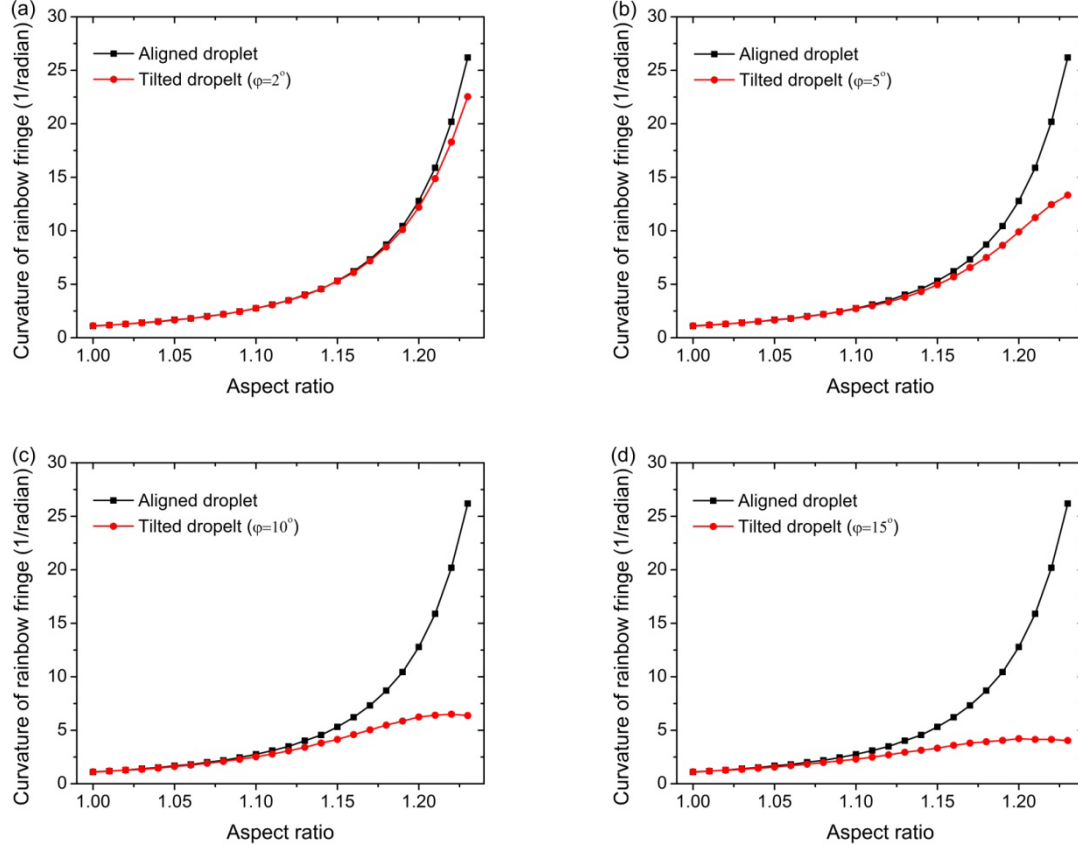
Fig. 7.5.   Comparison of the curvature of rainbow fringe for aligned droplets and tilted droplets: (a) φ=2°, (b) φ=5°, (c) φ=10°, and (d) φ=15°.

The purpose of computing the rainbow fringes is to check if the rainbow fringe can be used to measure the aspect ratio and tilt angle for tilted spheroidal droplets. Therefore, the curvature of the rainbow fringe for tilted spheroidal droplets is calculated using the VRT simulation and is compared with that for aligned spheroidal droplets. For comparison, only the curvature at the apex point in the equatorial plane of the rainbow fringe is calculated. Such a comparison is given in Fig. 7.5. It can be seen that for spheroidal droplets with small tilt angles, the curvature is in close agreement with that for aligned spheroidal droplets (see Fig. 7.5a and 7.5b). As the tilt angle increases, the difference of the curvatures becomes more pronounced (see Fig. 7.5c and 7.5d). For $1.15 \leq a/c \leq 1.23$ the curvature differ ence increases as aspect ratio increases. However, for small aspect ratios, the curvature for tilted droplets still agrees with that for aligned spheroidal droplets. It can be seen that, for spheroidal droplets with small tilt angle, the rainbow fringe can still be used to calculate the aspect ratio.

7.3   Preliminay experiment investigation for tilted spheroidal droplet
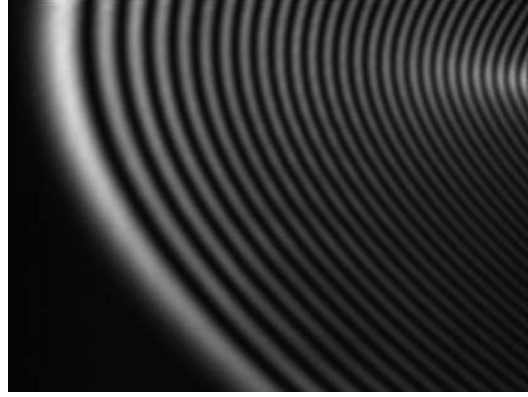
Fig. 7.6.   A generalized rainbow pattern for a spheroidal water droplet with φ=-5.21^o, *D*=1.79*mm*, *H*=1.61*mm*, *D/H*=1.11.
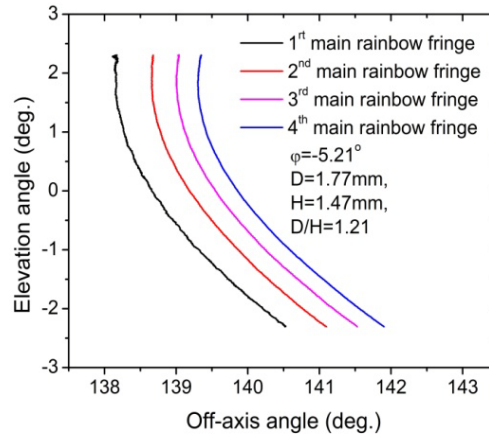
Fig. 7.7.   Main rainbow fringes for the generalized rainbow pattern as shown in Fig. 7.6.

The generalized rainbow pattern for tilted spheroidal droplets has also been experimentally investigated. In experiment, the acoustic levitator is tilted in order to obtain a tilted droplet. The levitator is rotated clockwise about an axis perpendicular to the light beam. In this case, the droplet is not stably positioned in the levitator, since the lateral forces are quite weak. Therefore, only small tilt angles can be realized.

The parameters of the tilted droplet are as follows: *D* is the droplet diameter in the horizontal equatorial plane and *H* is the diameter along the vertical axis of the rotational symmetry. Figure 7.6 shows the generalized rainbow pattern for a tilted spheroidal droplet with φ=-5.21^o, *D*=1.79*mm*, *H*=1.61*mm*, *D/H*=1.11. As the droplet is tilted clockwise, the generalized rainbow pattern is rotated clockwise and the pattern no longer exhibits

86

symmetrical about the horizontal plane. However, the generalized pattern is symmetrical about the horizontal plane for an aligned droplet (see Fig. 5.4). The main rainbow fringe of generalized rainbow pattern is calculated and shown in Fig.7.7. From VRT simulations, it is known that the rainbow fringe is tilted clockwise for the clockwise tilted droplet and vice verse. In this respect, the experiment agrees with the VRT simulation.

In summary, the changes of the optical caustic structures in response to the tilt angle are studied based on vector ray tracing. The rainbow fringes are tilted counterclockwise as the spheroidal droplet is tilted counterclockwise and vice versa. The changes of the fringes depend on the aspect ratio and tilt angle. The generalized rainbow pattern for a tilted spheroidal droplet has also been measured experimentally, exhibiting good agreement with simulations.

Chapter 8   Deviation between geometrical rainbow position of an ellipse and that of a sphere

Möbius's approximation (Möbius, 1910) has been used to calculate the deviation between the geometrical rainbow angle for an ellipse and that for a sphere ((van Beeck, et al., 1995) and (Lohner, et al., 1999)). However, there was some misuse of Möbius's approximation as will be shown in this chapter. Here the modified Möbius equation is given and the vector ray tracing model is used to compute the rainbow angle deviation for an ellipse, which agrees with the modified Möbius equation for small eccentricity. Moreover, the application range of Möbius's approximation is also investigated.

8.1   Modification of Möbius's approximation
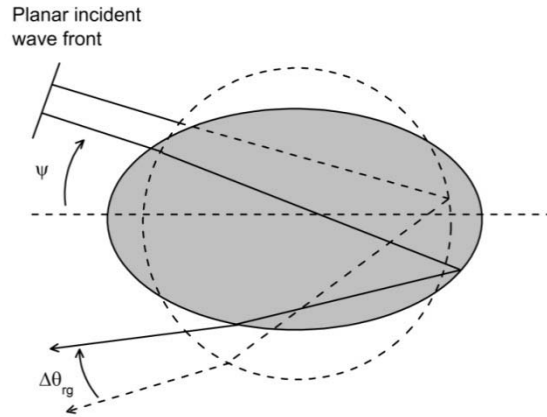
Fig. 8.1.   Schematic of the deviation between rainbow angle of an ellipse and that of a sphere.

The deviation $\Delta\vartheta_{rg}$ (see Fig. 8.1) between the geometrical rainbow angle for an ellipse and that for a sphere can be written as (Möbius, 1910):

$$\Delta\theta_{rg} = \theta_{gn} - \theta_{rg} = -16\rho\sin\theta_{r0}\cos^3\theta_{r0}\cos\left(-2\psi + \theta_{rg}\right) \tag{8.1}$$

Here ϑ_{gn} and ϑ_{rg} are the rainbow angle for an ellipse and that for a sphere in the sense of geometric optics respectively. ϑ_{r0} is the corresponding incident angle of the rainbow angle for a sphere and ψ the oblique angle of incident light ray with respect to the major axis. And ρ is the eccentricity of the elliptical profile defined by:

$$\rho = \frac{a-c}{a+c} = \frac{a/c-1}{a/c+1}$$

(8.2)

here a and c are major and minor semi-axes of the elliptical profile respectively and a/c the aspect ratio of the ellipse.

Based on Eqs. (8.1) and (8.2), the angular difference between rainbow position of an ellipse and that of a sphere (refractive index m=1.333) is shown in Fig. 8.2. For an ellipse with a/c=1.002, the rainbow angle of ellipse deviate 0.195^o from that of a sphere. However the deviation angle increase to 0.973^o for an ellipse with for a/c=1.010. As shown in Fig. 8.1, the ellipse is symmetrical about the major axis. Thereby the deviation curve should be symmetrical around $\psi=0^o$. However the deviation curve in Fig. 8.2 is not this case. The results similar to Fig. 8.2 were shown in several references, which were not symmetrical about the around $\psi=0^o$. That is because the misunderstanding of oblique angle in Eq. (8.1). The value of oblique angle in Eq. (8.1) should be kept positive. That is Eq. (8.1) is modified as:

$$\Delta\theta_{rg} = \theta_{gn} - \theta_{rg} = -16\rho\sin\theta_{r0}\cos^3\theta_{r0}\cos\left(-2|\psi|+\theta_{rg}\right) \quad for \quad a/c \geq 1.0,$$
$$\Delta\theta_{rg} = \theta_{gn} - \theta_{rg} = -16\rho\sin\theta_{r0}\cos^3\theta_{r0}\cos\left(2|\psi|+\theta_{rg}\right) \quad for \quad a/c < 1.0.$$

(8.3)

On the other hand, the rainbow angle for an ellipse also can be calculated according to vector ray tracing (VRT). Then the above argument can be validated.
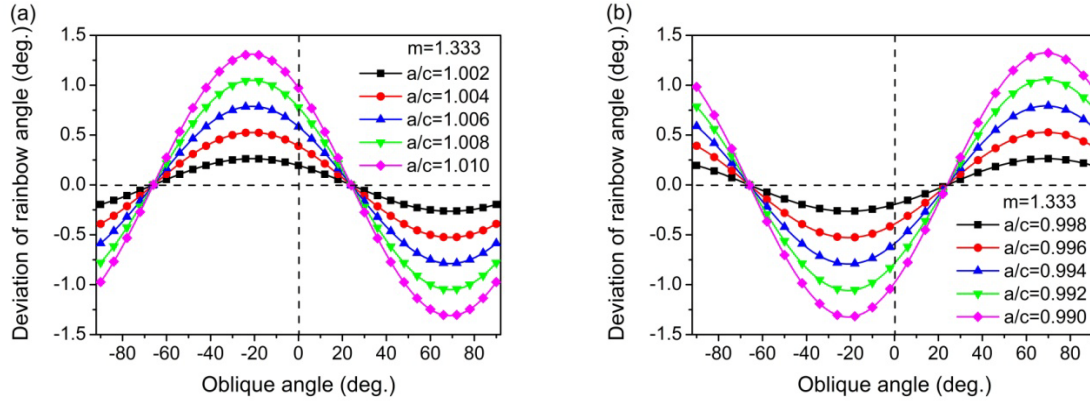

Fig. 8.2.   Angular difference between the geometric rainbow position of an ellipse and a sphere.

8.2 Comparison of modified Möbius's approximation and VRT simulation

Then the difference between the geometric rainbow angles of an ellipse and a sphere are calculated by Eq. (8.3) and by vector ray tracing. Figure 8.3 shows the angular difference for

ellipses with aspect ratios a/c=1.002, 1.010, 1.020, and 1.050 respectively. It can be seen that the angular difference calculated by the modified Möbius equation agrees well with that by vector ray tracing for small aspect ratios (see Figs. 8.3a-3c). Furthermore, the deviation curve are symmetrical around $\psi=0^o$, which demonstrates that the modified equation is correct. However, for an aspect ratio of a/c=1.050, the larger differences between the modified equation and vector ray tracing are observed, as shown in Fig. 8.3d. That is because the Möbius equation is only available for an ellipse with small eccentricity (Marston, 1980). For an aspect ratio a/c=1.002, the angular difference of the geometric rainbow angle for an ellipse and sphere is less than 0.5^o. As the aspect ratio increases, the corresponding angular difference becomes larger. However, the shapes of the curve are similar in Figs. 8.3a-8.3d. That is because for different ellipses, only the eccentricity ρ is changed, leaving other parameters unchanged in Eq. (8.3).
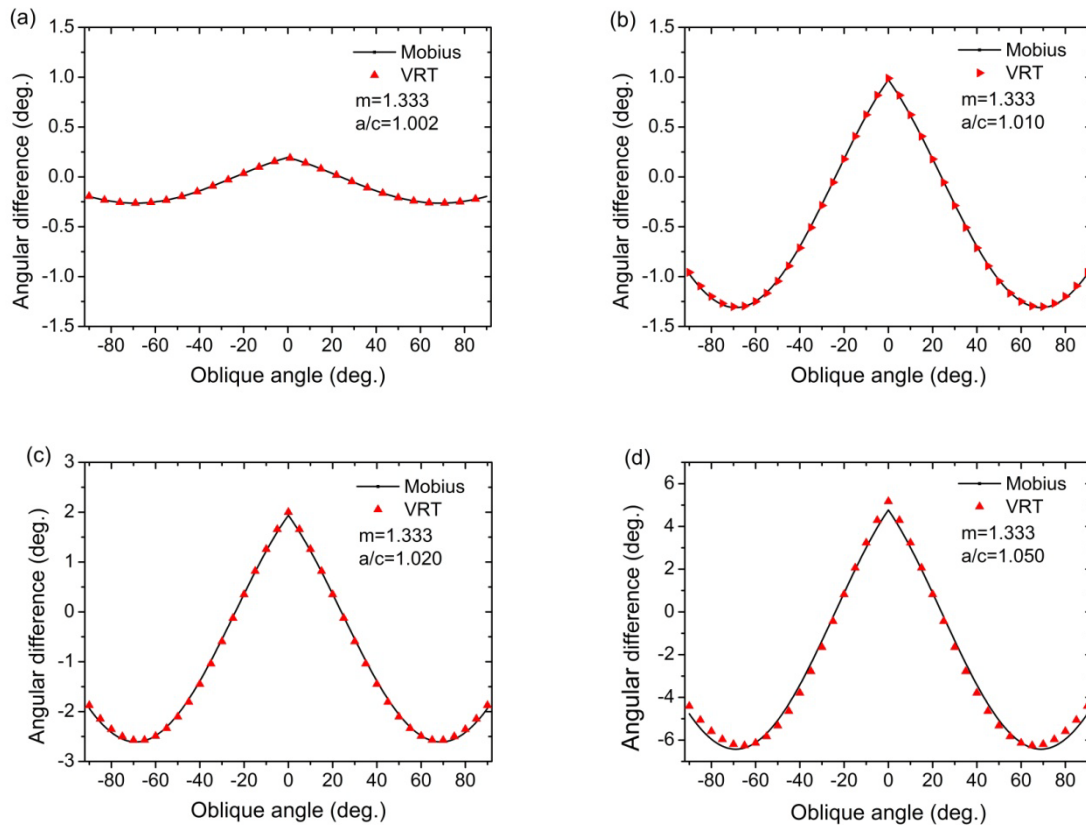
Fig. 8.3.   Comparison the angular difference between the geometric rainbow position of an ellipse and a sphere calculated from Eq. (8.3) and that by vector ray tracing.
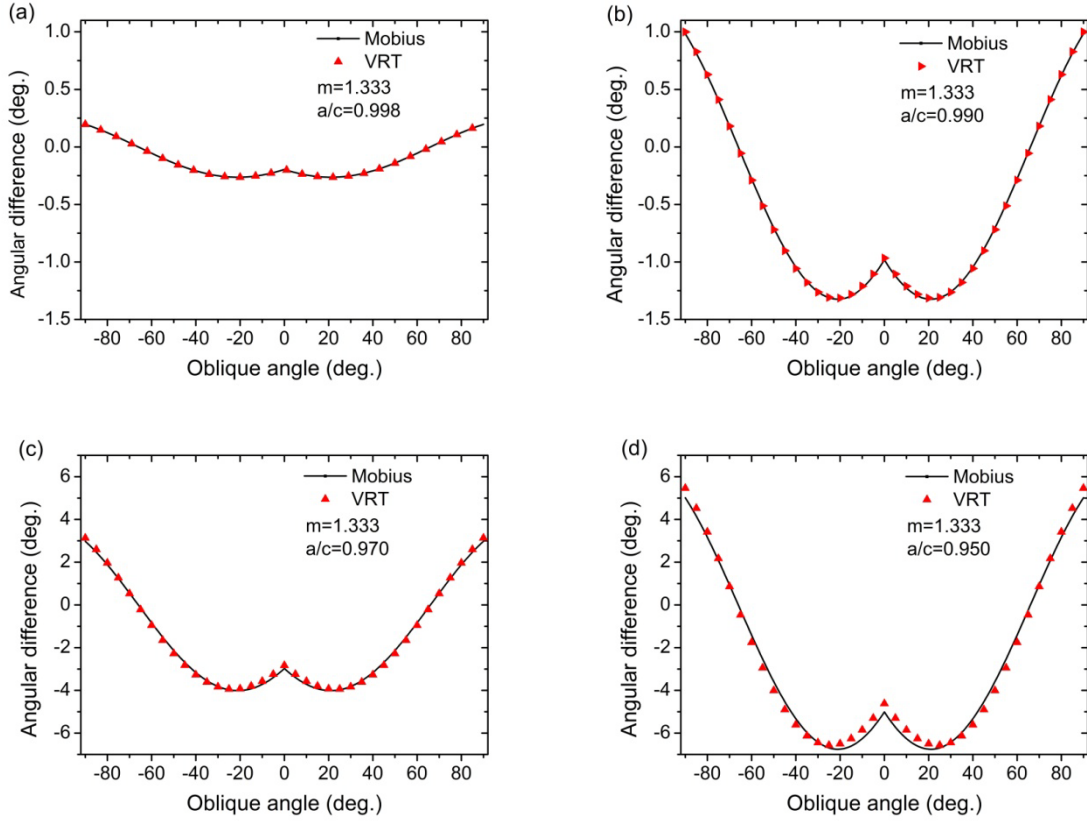
Fig. 8.4.   Same parameters as Fig 8.3, but with different aspect ratios.

Figure 8.4 shows the comparison of the modified equation and vector ray tracing for an ellipse with varying aspect ratio a/c=0.998, 0.990, 0.97, and 0.95. Similar to Fig 8.3, modified equation is consistent with vector ray tracing for small eccentricity. For a/c=0.95, that is the absolute eccentricity equals 0.026, the difference between the two methods are observed in Fig. 8.4d.

Furthermore, the application range of the Möbius's approximation is investigated. For aspect ratios between 0.95 (ρ=0.026) and 1.05 (ρ=0.024), vector ray tracing agrees with the Möbius's approximation, as shown in Fig. 8.5a. The difference between the two methods is around 0.4^{o} for a/c=0.95. However for large eccentricities, the differences observed increase (Fig. 8.6a). For a/c=0.5 (ρ=0.333), a difference up to 25.71^{o} (see Fig. 8.6b) is observed, while for small eccentricity, that is 0.95≤a/c≤1.05, the Möbius's approximation can predict the rainbow angular difference of ellipses.
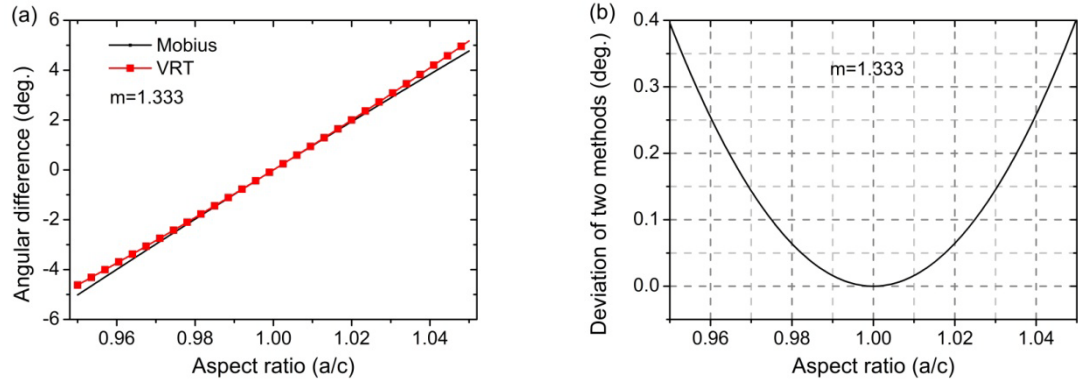
Fig 8.5.   Comparison of the rainbow angular difference calculate by Möbius's approximation and that by vector ray tracing.
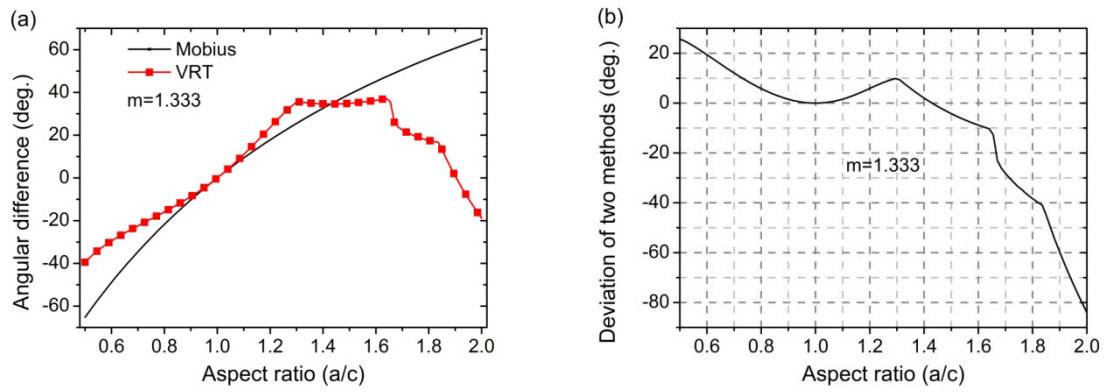
Fig 8.6.   Same parameters as Fig 8.5, but with different aspect ratio range.

8.3 Conclusion

In summary, Möbius's approximation is modified to calculate the deviation between the geometrical rainbow angle for an ellipse and that for a sphere. The vector ray tracing model is also used to compute the rainbow angle deviation for an ellipse, which agrees with modified Möbius equation for small eccentricity. Moreover, the application range of Möbius's approximation is also investigated. It is demonstrated that for small eccentricity, that is $0.95 \leq a/c \leq 1.05$, the Möbius's approximation can predict the rainbow angle difference of ellipse.

Chapter 9   Conclusion and perspectives

9.1 Conclusion

In summary, the VRT model is employed to simulate optical caustic structures including the rainbow and hyperbolic umbilic (HU) fringes in the primary rainbow region of light scattering from oblate water droplets. The location of cusp caustics are calculated by VRT simulation and compared with that by analytic solution, for which good agreement is found. The evolution of the optical caustic structures in response to shape deformation of oblate water droplets is investigated by VRT simulation and is found to be consistent with experimental observation. For the secondary rainbow, the location of cusp caustic is also calculated by use of the VRT simulation and compared with that calculated using analytic solutions: excellent agreement is also found. The optical caustic structures for the secondary rainbow are first simulated and analyzed systematically according to VRT model and the evolution process of the optical caustic structures is consistent with experimental observation.

The generalized rainbow patterns from spheroidal water droplets are measured in an experiment. According to the generalized rainbow patterns and Airy approximation, the refractive index and equatorial diameter of water droplets can be inverted from the corresponding generalized rainbow patterns. Comparison of the refractive indices inverted from the generalized rainbow patterns with that of pure water shows good agreement, with absolute errors less than 0.5×10^{-4}. The water droplet diameters in the horizontal equatorial plane are calculated from the generalized rainbow patterns and compared to that measured by direct imaging. It is shown that the relative errors of droplet diameters associated with the corresponding generalized rainbow patterns lie between -5% and 5%; hence reliable diameter estimations of droplets can be obtained from the generalized rainbow patterns. The curvatures of simulated rainbow fringes are compared with observed ones from the generalized rainbow patterns, in which good agreement is also shown. Since for a given type of droplet, the curvatures of the rainbow fringes are only a function of the aspect ratios, the non-sphericity (in terms of aspect ratio) of water droplets are inferred from the relevant generalized rainbow patterns. The relative errors of aspect ratios calculated from the generalized rainbow pattern lie between -1% and 1%. Accordingly, the complete information of a spheroidal water droplet in terms of geometric and optical properties are obtained.

And then, the changes of the optical caustic structures in response to the tilted angle are studied based on vector ray tracing. The rainbow fringes are counterclockwise tilted as the spheroidal droplet is counterclockwise tilted and vice versa. The changes of the fringes depend on the aspect ratio and tilted angle. And a generalized rainbow pattern for a tilted spheroidal droplet is investigated.

Furthermore, Möbius's approximation is modified to calculate the deviation between the geometrical rainbow angle for an ellipse and that for a sphere. The vector ray tracing model is also used to compute the rainbow angle deviation for an ellipse, which agrees with modified Möbius equation for small eccentricity. It is demonstrates that, for small eccentricity, that is, 0.95≤a/c ≤1.05, the Möbius's approximation can predict the rainbow angle difference of ellipse.

9.2 Perspectives

The VRT model has been employed for the first time to investigate the optical caustic structures, whereby the generalized rainbow pattern is used for measuring the refractive index, size, and shape (in terms aspect ratio) of a spheroidal water droplet. Nevertheless, there are several interesting investigations that still need to be carried out.

1. Whole optical caustic structure

 VRT model is used to study the optical caustic structure in primary and secondary rainbow regions of oblate spheroid. And the rainbow and HU fringes are analyzed and good consistence with experiment is found. However only partly of the caustic structures are shown and investigated. The whole optical caustic structure for oblate and prolate spheroids should be investigated;

2. Application range of generalized rainbow technique

Because of smaller or larger droplets or droplets with larger ratios are unstable in the levitator, only water droplets in the size range of 0.80-2.00 *mm* and aspect ratios smaller than 1.23 are investigated. And the refractive index, size, and shape (in terms aspect ratio) of spheroidal water droplets are inverted from the corresponding generalized rainbow patterns. The application range of the generalized rainbow pattern on size measurement of particle needs further study;

3. Application of secondary rainbow pattern on droplet measurement

For water droplet with aspect ratio around 1.31, the hyperbolic umblic diffraction catastrophe appears and make it is difficult to measure the droplet. However, it can be seen from VRT simulation that the secondary rainbow pattern can be used for droplet measurement in this aspect ratio range. That need be investigated in experiment;

4. Analytical solution of the relation between rainbow fringe curvature and aspect ratio of spheroid

The relation between rainbow fringe curvature and aspect ratio of spheroid has been established by simulation and experiment. However the analytical simulation need to pursuit;

5. Investigation of tilted droplet

Due to the droplet orientation are arbitrary in many industrial processes, further experimental investigations of abnormally oriented droplet also are is worthy carrying out;

6. Application of generalized rainbow technique

Furthermore, because of the high measurement accuracy, the generalized rainbow technique perhaps can be used for designing an optical instrument for particle characterization including the refractive index, temperature, size, and shape.

Appendices

Appendix A   Intersection point of a light ray and surface of a spheroidal particle

In this appendix, the calculation of the intersection point of a light ray and surface of a spheroidal particle is summarized. The functions of a straight line and a spheroid and the solutions of a quadratic equation are recalled.

Suppose the directional vector of a light ray can be described by (m_0, n_0, p_0). And point (x_0, y_0, z_0) is any point on the light ray (see Fig. A1). The light ray may be an incident ray, reflection ray or refraction ray. In each case, the vector (m_0, n_0, p_0) is parallel to the direction of the light ray. The equation of the light ray can be expressed as:

$$\frac{x - x_0}{m_0} = \frac{y - y_0}{n_0} = \frac{z - z_0}{p_0} \tag{A1}$$

It is assumed that $m_0 \neq 0$, $n_0 \neq 0$, and $p_0 \neq 0$ in Eq. (A1). However, one or two of the three parameters (m_0, n_0, p_0) can be zero. The meaning of these light rays will be given in detail in the following.

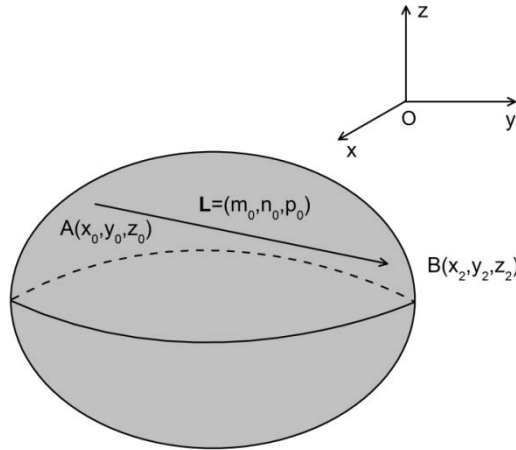Fig. A1. Schematics of intersection points of light ray and particle surface.

Suppose the particle is an ellipsoid. Then the surface of the particle is a closed quadric surface and is a three dimensional analogue of an ellipse. The standard equation of an ellipsoid centered at the origin of a Cartesian coordinate system is given as:

$$\frac{x^2}{a^2} + \frac{y^2}{b^2} + \frac{z^2}{c^2} = 1 \tag{A2}$$

where a, b and c are called the semi-principal axes aligned along the coordinate axes. If two of the three parameters equal each other, the ellipsoid reduces to a spheroid. For example, for an oblate spheroid, $a=b$ and $a>c$.

Consider a light ray impinging on the particle surface at the point (x_0, y_0, z_0). The light ray will intersect the particle surface at other point. However when the light ray is tangent to the particle surface, the ray intersects the particle surface only at one singular point. Since the point (x_0, y_0, z_0) is on the surface of the ellipsoid, the following equation exists:

$$\frac{x_0^2}{a^2} + \frac{y_0^2}{b^2} + \frac{z_0^2}{c^2} = 1 \tag{A3}$$

The point (x_0, y_0, z_0) is the given intersection point of the light ray and the particle surface. To look for the other intersection point is to solve Eqs. (A1)-(A3). The derivations are given as follows.

(I) Case 1: $m_0 \neq 0$, $n_0 \neq 0$, and $p_0 \neq 0$

In this case, the light ray does not parallel to any axis of the coordinate.

By using Eq. (A1), one can get:

$$y = y_0 + \frac{n_0}{m_0}(x - x_0) \tag{A4}$$

$$z = z_0 + \frac{p_0}{m_0}(x - x_0) \tag{A5}$$

Substituting Eqs. (A4) and (A5) into Eq. (A3), one could obtain:

$$\frac{x^2}{a^2} + \frac{1}{b^2}\left[y_0 + \frac{n_0}{m_0}(x - x_0)\right]^2 + \frac{1}{c^2}\left[z_0 + \frac{p_0}{m_0}(x - x_0)\right]^2 = 1 \tag{A6}$$

Combining Eq. (A6) with Eq. (A3), after some algebra, Eq. (A6) could be written as:

$$\left(\frac{1}{a^2} + \frac{n_0^2}{m_0^2}\frac{1}{b^2} + \frac{p_0^2}{m_0^2}\frac{1}{c^2}\right)x^2 + 2\left(-\frac{n_0^2}{m_0^2}\frac{x_0}{b^2} + \frac{n_0}{m_0}\frac{y_0}{b^2} - \frac{p_0^2}{m_0^2}\frac{x_0}{c^2} + \frac{p_0}{m_0}\frac{z_0}{c^2}\right)x$$

$$+ \frac{n_0^2}{m_0^2}\frac{x_0^2}{b^2} - 2\frac{n_0}{m_0}\frac{x_0 y_0}{b^2} + \frac{p_0^2}{m_0^2}\frac{x_0^2}{c^2} - 2\frac{p_0}{m_0}\frac{x_0 z_0}{c^2} - \frac{x_0^2}{a^2} = 0 \tag{A7}$$

In a simple form, Eq. (A7) could be rewritten as:

$$a_1 x^2 + b_1 x + c_1 = 0 \tag{A8}$$

where

$$a_1 = \frac{1}{a^2} + \frac{n_0^2}{m_0^2}\frac{1}{b^2} + \frac{p_0^2}{m_0^2}\frac{1}{c^2},$$

$$b_1 = 2\left(-\frac{n_0^2}{m_0^2}\frac{x_0}{b^2} + \frac{n_0}{m_0}\frac{y_0}{b^2} - \frac{p_0^2}{m_0^2}\frac{x_0}{c^2} + \frac{p_0}{m_0}\frac{z_0}{c^2}\right), \tag{A9}$$

$$c_1 = \frac{n_0^2}{m_0^2}\frac{x_0^2}{b^2} - 2\frac{n_0}{m_0}\frac{x_0 y_0}{b^2} + \frac{p_0^2}{m_0^2}\frac{x_0^2}{c^2} - 2\frac{p_0}{m_0}\frac{x_0 z_0}{c^2} - \frac{x_0^2}{a^2}.$$

The roots of Eq. (A8) are given by:

$$x = \frac{-b_1 \pm \sqrt{b_1^2 - 4a_1 c_1}}{2a_1} \tag{A10}$$

From Eq. (A9), one can obtain:

$$\begin{aligned}
b_1^2 = 4\Bigg(&\frac{n_0^4}{m_0^4}\frac{x_0^2}{b^4} + \frac{n_0^2}{m_0^2}\frac{y_0^2}{b^4} + \frac{p_0^4}{m_0^4}\frac{x_0^2}{c^4} + \frac{p_0^2}{m_0^2}\frac{z_0^2}{c^4} - 2\frac{n_0^3}{m_0^3}\frac{x_0 y_0}{b^4} + 2\frac{n_0^2 p_0^2}{m_0^4}\frac{x_0^2}{b^2 c^2} \\
&- 2\frac{n_0^2 p_0}{m_0^3}\frac{x_0 z_0}{b^2 c^2} - 2\frac{n_0 p_0^2}{m_0^3}\frac{x_0 y_0}{b^2 c^2} + 2\frac{n_0 p_0}{m_0^2}\frac{y_0 z_0}{b^2 c^2} - 2\frac{p_0^3}{m_0^3}\frac{x_0 z_0}{c^4}\Bigg)
\end{aligned} \tag{A11}$$

$$\begin{aligned}
4a_1 c_1 = 4\Bigg(&\frac{n_0^4}{m_0^4}\frac{x_0^2}{b^4} + \frac{p_0^4}{m_0^4}\frac{x_0^2}{c^4} + 2\frac{n_0^2 p_0^2}{m_0^4}\frac{x_0^2}{b^2 c^2} - \frac{x_0^2}{a^4} - 2\frac{n_0}{m_0}\frac{x_0 y_0}{a^2 b^2} - 2\frac{p_0}{m_0}\frac{x_0 z_0}{a^2 c^2} \\
&- 2\frac{n_0^3}{m_0^3}\frac{x_0 y_0}{b^4} - 2\frac{n_0^2 p_0}{m_0^3}\frac{x_0 z_0}{b^2 c^2} - 2\frac{n_0 p_0^2}{m_0^3}\frac{x_0 y_0}{b^2 c^2} - 2\frac{p_0^3}{m_0^3}\frac{x_0 z_0}{c^4}\Bigg)
\end{aligned} \tag{A12}$$

and

$$b_1^2 - 4a_1 c_1 = 4\left(\frac{x_0}{a^2} + \frac{n_0}{m_0}\frac{y_0}{b^2} + \frac{p_0}{m_0}\frac{z_0}{c^2}\right)^2 \tag{A13}$$

So the roots of Eq. (A7) are:

$$x_1 = x_0 \tag{A14}$$

$$x_2 = x_0 - 2M_1 \tag{A15}$$

where

$$M_1 = \frac{\dfrac{x_0}{a^2} + \dfrac{n_0}{m_0}\dfrac{y_0}{b^2} + \dfrac{p_0}{m_0}\dfrac{z_0}{c^2}}{\dfrac{1}{a^2} + \dfrac{n_0^2}{m_0^2}\dfrac{1}{b^2} + \dfrac{p_0^2}{m_0^2}\dfrac{1}{c^2}} \tag{A16}$$

Combining Eqs. (A4) and (A5) with Eqs. (A14) and (A15), the solutions for Eqs. (A1)-(A3) are given by:

$$\begin{cases} x_1 = x_0, \\ y_1 = y_0, \\ z_1 = z_0. \end{cases} \tag{A17}$$

and

$$\begin{cases} x_2 = x_0 - 2M_1, \\ y_2 = y_0 - 2M_1 \dfrac{n_0}{m_0}, \\ z_2 = z_0 - 2M_1 \dfrac{p_0}{m_0}. \end{cases} \tag{A18}$$

here the intersection point (x_0, y_0, z_0) of the light ray and the particle surface has been given. So the point (x_2, y_2, z_2) is other intersection point of the light ray and the particle surface.

In summary, if the direction of the light ray described by the vector (m_0, n_0, p_0), the function of particle surface and one intersection point (x_0, y_0, z_0) of the light ray and particle surface are given, the other intersection point can be calculated according to Eq. (A18). The above derivations are valid for $m_0 \neq 0$, $n_0 \neq 0$, and $p_0 \neq 0$. The other cases are given in the following.

(II) Case 2: $m_0 = 0$, $n_0 \neq 0$, and $p_0 \neq 0$

If $m_0 = 0$, $n_0 \neq 0$, and $p_0 \neq 0$, the light ray can be expressed as:

$$\begin{aligned} & x = x_0, \\ & \frac{y - y_0}{n_0} = \frac{z - z_0}{p_0}. \end{aligned} \tag{A19}$$

The physical meaning is that the light ray is perpendicular to the x-axis.

The particle surface still satisfies the Eqs. (A2) and (A3). Here it is assumed that the light ray impinges on the particle surface at the point (x_0, y_0, z_0). To look for the other intersection point of the light ray and particle surface is to solve the equations (A2), (A3) and (A19). Following the steps as given in case 1, we can obtain the coordinates of other intersection point:

$$\begin{cases} x_2 = x_0, \\ y_2 = y_0 - 2M_2, \\ z_2 = z_0 - 2M_2 \dfrac{p_0}{n_0}. \end{cases} \tag{A20}$$

where

$$M_2 = \frac{\dfrac{y_0}{b^2} + \dfrac{p_0}{n_0}\dfrac{z_0}{c^2}}{\dfrac{1}{b^2} + \dfrac{p_0^2}{n_0^2}\dfrac{1}{c^2}}$$

(A21)

(III) Case 3: $m_0 \neq 0$, $n_0 = 0$, and $p_0 \neq 0$

If $m_0 \neq 0$, $n_0 = 0$, and $p_0 \neq 0$, the light ray can be given as:

$$y = y_0,$$
$$\frac{x - x_0}{m_0} = \frac{z - z_0}{p_0}.$$

(A22)

here (x_0, y_0, z_0) are defined as above. The physical meaning of the light ray is that it is perpendicular to the y-axis.

By solving the equations (A2), (A3) and (A22), we could find the other intersection point of the light ray and particle surface. So the coordinates of the other intersection point are given as:

$$\begin{cases} x_2 = x_0 - 2M_3, \\ y_2 = y_0, \\ z_2 = z_0 - 2M_3\dfrac{p_0}{m_0}. \end{cases}$$

(A23)

where

$$M_3 = \frac{\dfrac{x_0}{a^2} + \dfrac{p_0}{m_0}\dfrac{z_0}{c^2}}{\dfrac{1}{a^2} + \dfrac{p_0^2}{m_0^2}\dfrac{1}{c^2}}$$

(A24)

(IV) Case 4: $m_0 \neq 0$, $n_0 \neq 0$, and $p_0 = 0$

If $m_0 \neq 0$, $n_0 \neq 0$, and $p_0 = 0$, the light ray can be expressed as:

$$z = z_0,$$
$$\frac{x - x_0}{m_0} = \frac{y - y_0}{n_0}.$$

(A25)

here (x_0, y_0, z_0) are defined as above. The physical meaning is the light ray is perpendicular to the z-axis.

To look for the other intersection point of the light ray and particle surface is to solve the equations (A2), (A3) and (A25). So the coordinates of the other intersection point are given as follows:

103

$$\begin{cases} x_2 = x_0 - 2M_4, \\ y_2 = y_0 - 2M_4 \dfrac{n_0}{m_0}, \\ z_2 = z_0. \end{cases} \tag{A26}$$

where

$$M_3 = \frac{\dfrac{x_0}{a^2} + \dfrac{n_0}{m_0} \dfrac{y_0}{b^2}}{\dfrac{1}{a^2} + \dfrac{n_0^2}{m_0^2} \dfrac{1}{b^2}} \tag{A27}$$

(V) Case 5: $m_0 \neq 0$, $n_0 = 0$, and $p_0 = 0$

If $m_0 \neq 0$, $n_0 = 0$, and $p_0 = 0$, the light ray can be expressed as:

$$\begin{aligned} y &= y_0, \\ z &= z_0. \end{aligned} \tag{A28}$$

The physical meaning of the light ray is that it is perpendicular to the y-axis and z-axis, that is, it is parallel to x-axis.

By solving the equations (A2), (A3) and (A28), we could find the other intersection point of the light ray and particle surface. The coordinates of other intersection point are given by:

$$\begin{cases} x_2 = -x_0, \\ y_2 = y_0, \\ z_2 = z_0. \end{cases} \tag{A29}$$

(VI) Case 6: $m_0 = 0$, $n_0 \neq 0$, and $p_0 = 0$

If $m_0 = 0$, $n_0 \neq 0$, and $p_0 = 0$, the light ray can be expressed as:

$$\begin{aligned} x &= x_0, \\ z &= z_0. \end{aligned} \tag{A30}$$

The physical meaning is that the light ray is parallel to y-axis.

To look for the other intersection point of the light ray and particle surface is to solve the equations (A2), (A3) and (A30). The coordinates of the other intersection point are expressed as follows:

$$\begin{cases} x_2 = x_0, \\ y_2 = -y_0, \\ z_2 = z_0. \end{cases} \tag{A31}$$

(VII) Case 7: $m_0 = 0$, $n_0 = 0$, and $p_0 \neq 0$

If $m_0 = 0$, $n_0 = 0$, and $p_0 \neq 0$, the light ray can be expressed as:

$$x = x_0,$$
$$y = y_0.$$

(A32)

That means the light ray is parallel to z-axis.

By solving the equations (A2), (A3) and (A32), we could find the other intersection point of the light ray and particle surface. The coordinates of the other intersection point are given as:

$$\begin{cases} x_2 = x_0, \\ y_2 = y_0, \\ z_2 = -z_0. \end{cases}$$

(A33)

(VIII) Case 8: m_0=0, n_0=0, and p_0=0

Mathematically, this represents a point in at the coordinate. So there is no physical meaning for this light ray.

In summary, given the direction of the light ray described by the vector (m_0, n_0, p_0), the functional form of the particle surface and one intersection point (x_0, y_0, z_0) of the light ray and particle surface, the other intersection point can be calculated according to the above derivations.
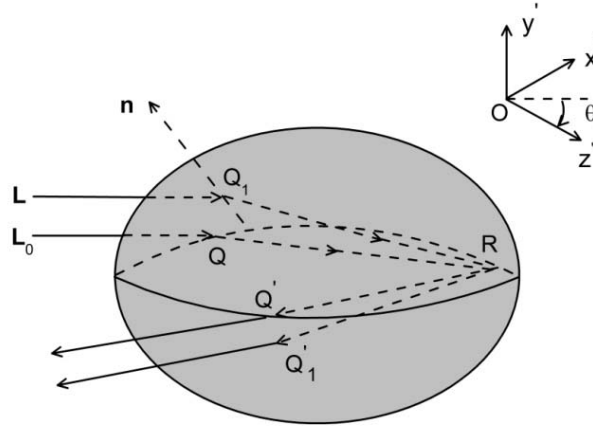
Appendix B   Location of cusp caustic

Fig. B1.   Rays associated with the cusp caustic.

As is well known, the cusp caustic is associated with the contribution from two equatorial rays and two skew rays (Marston, et al., 1984) and the VRT model allows the cusp caustic to be identified. On the other hand, Nye obtained a derivation for calculating the droplet aspect ratio when the hyperbolic umbilici catastrophe can be observed (Nye, 1984). Furthermore, an analytical solution to predict the location of cusp caustic was given based on Herzberger's formalism (Marston, 1985). In the present study the analytical solution for calculating the cusp location is derived based on geometric optics. In order to compare with Nye's derivation (Nye, 1984), an $O\text{-}x'y'z'$ coordinate system is used as shown in Fig. B1. The spheroidal surface satisfies $x'^2/a^2 + y'^2/c^2 + z'^2/a^2 = 1$. Associated with the incident direction $\mathbf{L}_0$, the Descartes rainbow ray impacts the droplet at the point $Q(0, 0, a)$ in the equatorial plane of the droplet. After being refracted into the droplet it intersects the surface at $R(a\sin 2\vartheta_r, 0, a\cos 2\vartheta_r)$, where ϑ_r is the angle of refraction at the entry point Q. Letting the Q shift by an infinitesimal amount ε_1 and ε_2 in x' and y' directions respectively and keeping the incident direction fixed, the entry point moves to $Q_1(\varepsilon_1, \varepsilon_2, -a(1-\varepsilon_1^2/a^2 - \varepsilon_2^2/c^2)^{1/2})$, which is off the equatorial plane. Generally, the refraction of the skew ray passes above or below the point R. If the skew ray also passes R, the exiting ray will remain parallel to the equatorial plane to first order according to the symmetry of the oblate spheroid. It means that the skew rays focus in the vertical direction as well as that in the horizontal plane.

The direction of the incident ray in the $O\text{-}x'y'z'$ coordinate system is given by $\mathbf{L}=(\sin\vartheta_i, 0, \cos\vartheta_i)$, where ϑ_i is the angle of incidence at point Q. To the first order, the normal to the

droplet surface at Q_1 is $\mathbf{n}_1=(\varepsilon_1/a^2, \varepsilon_2/c^2, -1/a)$. Provided that the skew ray passes through R, the ray of refraction is $\mathbf{L}'=(a\sin 2\vartheta_r - \varepsilon_1, -\varepsilon_2, a\cos 2\vartheta_r + a)$. The ray of incident direction $\mathbf{L}$, the normal $\mathbf{n}_1$ at the incident point and the refracted ray direction $\mathbf{L}'$ should be coplanar. It means that the vector triple product is zero ($\mathbf{L} \times \mathbf{n}_1 \times \mathbf{L}' \equiv 0$), namely:

$$
\begin{vmatrix}
\sin\theta_i & 0 & \cos\theta_i \\
\varepsilon_1/a^2 & \varepsilon_2/c^2 & -1/a \\
a\sin 2\theta_r - \varepsilon_1 & -\varepsilon_2 & a\cos 2\theta_r + a
\end{vmatrix} \equiv 0,
\tag{B1}
$$

After some algebra, one obtains:

$$
a\sin\theta_i \left(\frac{2\cos^2\theta_r}{c^2} - \frac{\sin 2\theta_r \cos\theta_i}{c^2 \sin\theta_i} - \frac{1}{a^2} \right)\varepsilon_2 + \cos\theta_i \left(\frac{1}{c^2} - \frac{1}{a^2} \right)\varepsilon_1\varepsilon_2 = 0.
\tag{B2}
$$

To the first order, the first term of Eq. (B2) must be zero. Then applying Snell's law, one obtains:

$$
a/c = m \left[2\left(m^2 - \sin^2\theta_i\right) - 2\left(m^2 - \sin^2\theta_i\right)^{1/2}\left(1 - \sin^2\theta_i\right)^{1/2} \right]^{-1/2}.
\tag{B3}
$$

Equation (B3) is as same as that obtained by Marston using Herzberger's formalism (Marston, 1985). For the spheroid with an aspect ratio satisfying the condition Eq. (B3), the skew rays will focus vertically. The two skew rays are above and below the equatorial plane respectively. Together with the two equatorial rays, they focus in the same direction, giving rise to the cusp caustic. According to geometrical optics, the scattering angle of the cusp ray is given by $\vartheta = \pi + 2\vartheta_i - 4\sin^{-1}(\sin\vartheta_i/m)$ and the primary Descartes ray satisfies $\sin\vartheta_i = (4-m^2/3)^{1/2}$. Substitution into Eq. (B3) yields the critical aspect ratio $a/c = [3m^2/(4m^2-4)]^{1/2}$, i.e. the ratio at which HUFS arises. This result is identical to that given by Nye (Nye, 1992).

References

1. **Airy, G. B.** On the intensity of light in the neighborhood of a caustic. *Trans. Cambridge Philos. Soc.* 6, 379–402 (1838).

2. **Albrecht, H.-E.; Borys, M.; Damaschke, N.; and Tropea, C.** *Laser Doppler and Phase Doppler Measurement Techniques.* Heidelberg : Springer-Verlag (2003).

3. **Asano, S. and Sato, M.** Light scattering by randomly oriented spheroidal particles. *Appl. Opt.* 19, 962–974 (1980).

4. **Asano, S. and Yamamoto, G.** Light scattering by a spheroidal particle. *Appl. Opt.* 14, 29–49 (1975).

5. **Asano, S.** Light scattering properties of spheroidal particles. *Appl. Opt.* 18, 712–723 (1979).

6. **Barton, J. P.** Internal and near-surface electromagnetic fields for a spheroidal particle with arbitrary illumination. *Appl. Opt.* 34, 5542–5551 (1995).

7. **Bashkatov, A. N. and Genina, E. A.** *Water refractive index in dependence on temperature and wavelength: a simple approximation.* Optical Technologies in Biophysics and Medicine IV, Proc. SPIE 5068 (2002).

8. **Berry, M. V and Upstill, C.** Catastrophe optics: morphologies of caustics and their diffraction patterns. *Prog. Opt.* 18, 257–346 (1980).

9. **Berry, M. V., Nye, J. F. and Wright, F. J.** The elliptic umbilic diffraction catastrophe. *Phil. Trans. R. Soc. Lond.* 291, 453–484 (1979).

10. **Born, M. and Wolf, E.** Principles of Optics. *University of Cambridge press* (1999).

11. **Choo-Smith, L.-P; Edwards, H. G. M.; Endtz, H. P.; Kros, J. M.; Heule, F.; Barr, H.; Robinson Jr, J. S.; Bruining, H. A.; and Puppels, G. J.** Medical applications of Raman spectroscopy: from proof of principle to clinical implementation. *Biopolymers,* 67, 1–9 (2002).

12. **Damaschke, N.; Nobach, H.; Semidetnov, and N.; Tropea, C.** Optical particle sizing in backscatter. *Appl*. *Opt*. 41, 5713–5727 (2002).

13. **Damaschke, N.; Gouesbet, G.; Gréhan, G.; and Tropea, C.** Optical techniques for the characterization of non-spherical and non-homogeneous particles. *Meas. Sci. Technol.* 9, 137–140 (1998).

14. **Damaschke, N.; Gouesbet, G.; Gréhan, G.; Mignon, H.; and Tropea, C.** Response of phase Doppler anemometer systems to nonspherical droplets. *Appl. Opt.* 37, 1752–1761 (1998).

15. **Dean, C. E. and Marston, P. L.** Opening rate of the cusp diffraction catastrophe in light scattered by oblate spheroidal drops. *Appl. Opt.* 30, 3443–3451 (1991).

16. **Debye, P.** Der Lichtdruck auf Kugeln von beliebigem Material. *Annalen der Physik,* 30, 57–136 (1909).

17. **Edward, G.** *A source book in medieval science.* Harvard University Press (1974).

18. **Glantschnig, W. J. and Chen, S. H.** Light scattering from water droplets in the geometrical optics approximation. *Appl. Opt.* 20, 2499–2509 (1981).

19. **Gouesbet, G.** Generalized Lorenz-Mie theory and applications. *Part. Part. Syst. Charact.* 11, 22–34 (1994).

20. **Gouesbet, G., Maheu, B. and Gréhan, G.** Light scattering from a sphere arbitrarily located in a Gaussian beam, using a Bromwich formulation. *J. Opt. Soc. Am.* A5, 1427–1443 (1988).

21. **Han, X. E.** Study of refractometry of rainbow and applications to the measurement of instability and temperature gradient of a liquid jet. *Doctoral Dissertation.* Rouen University (2000).

22. **Han, Y. P. and Wu, Z. S.** Scattering of a spheroidal particle illuminated by a Gaussian beam. *Appl. Opt.* 40, 2501–2509 (2001).

23. **Hergert, W. and Wriedt, T.** *The Mie Theory: Basics and Applications.* Springer (2012).

24. **Jackson, J. D.** From Alexander of Aphrodisias to Young and Airy. *Phys. Rep.* 320, 27–36 (1999).

25. **Kador, L.; Schittkowski, T.; Bauer, M.; and Fan, Y. W.** Three dimensional material analysis by confocal Raman microspectroscopy. *Appl. Opt.* 40, 4965–4970 (2003).

26. **Kaduchak, G. and Marston, P. L.** Hyperbolic umbilic and E6 diffraction catastrophes associated with the secondary rainbow of oblate water drops: observations with laser illumination. *Appl. Opt.* 33, 4697–4701 (1994).

27. **Kaduchak, G., Marston, P. L. and Simpson, H. J.** E6 diffraction catastrophe of the primary rainbow of oblate water drops: observations with white-light and laser illumination. *Appl. Opt.* 33, 4691–4696 (1994).

28. **Khare, V. and Nussenzveig, H.** Theory of the Rainbow. *Phys. Rev. Lett.* 33, 976–980 (1974).

29. **Können, G. P. and de Boer, J. H.** Polarized rainbow. *Appl. Opt.* 18, 1961–1965 (1979).

30. **Langley, D. S. and Marston, P. L.** Generalized tertiary rainbow of slightly oblate drops: observations with laser illumination. *Appl. Opt.* 37, 1520–1526 (1998).

31. **Lee, R. L.** Mie theory, Airy theory, and the natural rainbow. *Appl. Opt.* 37, 1506–1519 (1998).

32. **Lock, J. A. and Gouesbet, G.** Generalized Lorenz–Mie theory and applications. *J. Quant. Spectosc. Radiat. Transfer,* 110, 800–807 (2009).

33. **Lock, J. A. and Hovenac, E. A.** Internal caustic structure of illuminated liquid droplets. *J. Opt. Soc. Am.* A8, 1541–1552 (1991).

34. **Lock, J. A. and Xu, F.** Optical Caustics observed in light scattering by an oblate spheroid. *Appl. Opt.* 49, 1288–1304 (2010).

35. **Lock, J. A.** Contribution of high-order rainbows to the scattering of a Gaussian laser beam by a spherical particle. *J. Opt. Soc.Am.* 10, 693–706 (1993).

36. **Lock, J. A.** Ray scattering by an arbitrarily oriented spheroid. I. Diffraction and specular reflection. *App. Opt.* 35, 500–514 (1996).

37. **Lock, J. A.** Ray scattering by an arbitrarily oriented spheroid. II. Transmission and cross-polarization effects. *App. Opt.* 35, 515–531 (1996).

38. **Lock, J. A.** Theory of the observations made of high-order rainbows from a single water droplet. *Appl. Opt.* 26, 5291–5298 (1987).

39. **Lock, J. A., Jamison, J. M. and Lin, C. Y.** Rainbow scattering by a coated sphere. *Appl. Opt.* 33, 4677–4690 (1994).

40. **Lohner, H., Lehmann, P. and Bauckhage, K.** Detection Based on Rainbow Refractometry of Droplet Sphericity in Liquid–Liquid Systems. *Appl. Opt.* 38, 1127–1132 (1999).

41. **Lorenz, L. V.** Upon the light reflected and refracted by a transparent sphere. *Vidensk. Sel'sk Schrifter,* 6, 1–62 (1890).

42. **Lugovtsov, A. E., Priezzhev, A. V. and Nikitin, S. Yu.** Light scattering by arbitrarily oriented optically soft spheroidal particles: calculation in geometric optics approximation. *J. Quant. Spectosc. Radiat. Transfer,* 106, 285–296 (2007).

43. **Maeda, M., Kawaguchi, M. and Hishida, K.** Novel interferometric measurement of size and velocity distributions of spherical particles in fluid flows. *Meas. Sci. Technol.* 11, L13–L18 (2000).

44. **Marston, P. L and Kaduchak, G.** Generalized rainbows and unfolded glories of oblate drops: organization for multiple internal reflections and extension of cusps into Alexander's dark band. *Appl. Opt.* 33, 4702–4713 (1994).

45. **Marston, P. L.** Rainbow phenomena and the detection of nonsphericity in drops. *Appl. Opt.* 19, 680–685 (1980).

46. **Marston, P. L, Dean, C. E and Simpson, H. J.** Light scattering from spheroidal drops: exploring optical catastrophes and generalized rainbows. *AIP Conf. Proc.* 197, 275–285 (1989).

47. **Marston, P. L, Langley, D. S and Kingsbury, D. L.** Light scattering by bubbles in liquids: Mie theory, physical-optics approximation, and experiments. *Appl. Sci. Res.* 38, 373–383 (1982).

48. **Marston, P. L. and Trinh, E. H.** Hyperbolic umbilic diffraction catastrophe and rainbow scattering from spheroidal drops. *Nature,* 312, 529–531 (1984).

49. **Marston, P. L.** Catastrophe optics of spheroidal drops and generalized rainbows. *J. Quant. Spectosc. Radiat. Transfer,* 63, 341–351 (1999).

50. **Marston, P. L.** Cusp diffraction catastrophe from spheroids: generalized rainbows and inverse scattering. *Opt. Lett.* 10, 588–590 (1985).

51. **Marston, P. L.** Geometrical and catastrophe optics methods in scattering. *Phys. Acoust.* 21, 1–234 (1992).

52. **Marston, P. L.** Transverse cusp diffraction catastrophes: some pertinent wave fronts and a Pearcey approximation to the wave field. *J. Acoust. Soc. Am.* 81, 226–232 (1987).

53. **Mazeron, P. and Muller, S.** Light scattering by ellipsoids in a physical optics approximation. *Appl. Opt.* 35, 3726–3735 (1996).

54. **Mie, G.** Beiträte zur Optik trüber Medien, speziell kolloidaler Meatllösungen. *Annalen der Physik,* 25, 377–445 (1908).

55. **Möbius, W.** Zur Theorie des Regenbogens und ihrer experimentellen Prüfung. *Ann. Phys.* 33, 1493–1558 (1910).

56. **Ng, K. S. and Lee, W. K.** Interference of the nth- and the higher-order rainbows formed by a water drop. *J. Opt. Soc. Am.* B24, 3072–3076 (2007).

57. **Ng, P. H., Tse, M. Y. and Lee, W. K.** Observation of high-order rainbows formed by a pendant drop. *J. Opt. Soc. Am.* B15, 2782–2787 (1998).

58. **Nussenzveig, H. M.** Complex angular momentum theory of the rainbow and the glory. *J. Opt. Soc.Am.* 69, 1068–1079 (1979).

59. **Nussenzveig, H. M.** High-frequency scattering by a transparent sphere. I. direct reflection and transmission. *J. Math. Phys.* 10, 82–124 (1969).

60. **Nussenzveig, H. M.** The Theory of the Rainbow. *Sci. Am.* 236, 116–127 (1977).

61. **Nye, J. F.** Rainbow scattering from spheroidal drops-an explanation of the hyperbolic umbilic foci. *Nature,* 312, 531–532 (1984).

62. **Nye, J. F.** Rainbows from ellipsoidal water drops. *Proc. R. Soc. London,* 438, 397–417 (1992).

63. **Onofri, F. R. A.; Radev, S.; Sentis, M.; and Barbosa, S.** Physical-optics approximation of near-critical-angle scattering by spheroidal bubbles. *Opt. Lett.* 37, 4780–4782 (2012).

64. **Ravey, J, C. and Mazeron, P.** Light scattering in the physical optics approximation; application to large spheroids. *J. Opt.(Paris).* 13, 273–282 (1982).

65. **Ren, K. F.; Onofri, F.; Rozé, C.; and Girasole, T.** Vecctorial complex ray model and application to two-dimensional scattering of plane wave by a spheroidal particle. *Opt. Lett.* 36, 370–372 (2011).

66. **Roth, N., Anders, K. and Frohn, A.** *Simultaneous measurement of tecmperature and size of droplets in the micrometer range.* LIA : Int. Conf. on Optical Methods in Flow and Part. Diag. 294–304 (1988).

67. **Roth, N., Anders, K. and Frohn, A.** *Size insensitive rainbow refractometry: theoretical aspects.* Lisbon : 8th Int. Symp. Appl. Laser Techn. to Fluid Mech. 9.2.1–9.2.6 (1996).

68. **Saengkaew, S.; Godard, G.; Blaisot, J.; and Gréhan, G.** Experimental analysis of global rainbow technique: sensitivity of temperature and size distribution measurements to non-spherical droplets. *Exp. Fluids.* 47, 839–848 (2009).

69. **Saengkaewa, S.; Charinpanitkul, T.; Vanisri, H.; Tanthapanichakoon, W.; Mees, L.; Gouesbet, G.; and Grehan, G.** Rainbow refractrometry: On the validity domain of Airy's and Nussenzveig's theories. *Opt. Commun.* 259, 7–13 (2006).

70. **Sassen, K.** Angular scattering and rainbow formation in pendant drops. *J. Opt. Soc. Am.* 69, 1083–1089 (1979).

71. **Schäfer, W. and Tropea, C.** *Time-shift technique for characterization of transparent particles in sprays.* Lisbon : 16th Int. Symp. Appl. Laser Techn. to Fluid Mech., (2012).

72. **Semidetnov, N.** Investigation of laser Doppler anemometer as instrumentation for two-phase flow measurements. *Doctoral Dissertation.* Leningrad Inst Precis Mech Optics, (1985).

73. **Shen, J. Q. and Cai, X. S.** Algorithm of numerical calculation on Lorentz Mie theory. *PIERS Online 1.* 691–694 (2005).

74. **Shen, J. Q. and Wang, H. R.** Calculation of Debye series expansion of light scattering. *Appl. Opt.* 49, 2422–2428 (2010).

75. **Simpson, H. J. und Marston, P. L.** Scattering of white light from levitated oblate water drops near rainbows and other diffraction catastrophes. *Appl. Opt.* 30, 3468–3473 (1991).

76. **Tian, Y., Holt, R. G. and Apfel, R. E.** Deformation and Location of an Acoustically Levitated Liquid Drop. *J. Acoust. Soc. Am.* 93, 3096–3104 (1993).

77. **Tropea, C.** Optical particle characterization in flows. *Ann. Rev. Fluid Mech.* 43, 399–426 (2011).

78. **van Beeck, J. P. A. J. and Riethmuller, M. L.** Nonintrusive measurements of temperature and size of single falling raindrops. *Appl. Opt.* 34, 1633–1639 (1995).

79. **van Beeck, J. P. A. J. and Riethmuller, M. L.** Rainbow phenomena applied to the measurement of droplet size and velocity and to the detection of nonsphericity. *Appl. Opt.* 35, 2259–2266 (1996).

80. **van Beeck, J. P. A. J.** Rainbow phenomena: development of a laser-based, non-intrusive technique for measuring droplet size, temperature and velocity. *Doctoral Dissertation.* Technische Universiteit Eindhoven (1997).

81. **van Beeck, J. P. A. J.; Giannoulis, D.; Zimmer, L.; and Riethmuller, M. L.** Global rainbow thermometry for droplet-temperature measurement. *Opt. Lett.* 24, 1696–1698 (1999).

82. **van Beeck, J. P. A. J., Zimmer, L. and Riethmuller, M. L.** Global rainbow thermometry for mean temperature and size measurement of spray droplets. *Part. Part. Syst. Charact.* 18, 196–204 (2001).

83. **van de Hulst, H. C.** *Light scattering by small particles.* Dover (1981).

84. **Vetrano, M. R., van Beeck, J. P. A. J. and Riethmuller, M. L.** Global rainbow thermometry: improvements in the data inversion algorithm and validation technique in liquid-liquid suspension. *Appl. Opt.* 43, 3600–3607 (2004).

85. **Walker, J.** How to create and observe a dozen rainbows in a single drop of water. *Sci. Am.* 237, 138–144 (1977).

86. **Wang, Ru. T and van de Hulst, H. C.** Rainbows: Mie computations and the Airy approximation. *Appl. Opt.* 30, 106–117 (1991).

87. **Wriedt, T.** A review of elastic light scattering theories. *Part. Part. Syst. Charact. 1*5, 67–74 (1998).

88. **Wu, Z. S. and Ying, H. H.** Debye series of scattering by a multi-layered cylinder in an off-axis 2D gaussian beam. *Chin. Phys. Lett.* 25, 1672–1675 (2008).

89. **Xu, F. and Lock, J. A.** Debye series for light scattering by a coated nonspherical particle. *Phys. Rev.* A81: 063812 (2010).

90. **Xu, F., Cai, X. S. and Ren, K. F.** Geometrical optics approximation of forward scattering by coated particles. *Appl. Opt.* 43, 1870–1879 (2004).

91. **Xu, F.; Ren, K. F.; Cai, X. S.; and Shen, J. Q.** Extension of geometrical-optics approximation to on-axis Gaussian beam scattering. II. By a spheroidal particle with end-on incidence. *Appl.Opt.* 45, 5000–5009 (2006).

92. **Xu, F.; Ren, K. F.; Gouesbet, G.; Gréhan, G.; and Cai, X. S.** Generalized Lorenz-Mie theory for an arbitrarily oriented, located, and shaped beam scattered by a homogeneous spheroid. *Opt. Soc. Am.* A24, 119–131 (2007).

93. **Xu, F., Lock, J. A. and Gouesbet, G.** Debye series for light scattering by a nonspherical particle. *Phy. Rev.* A81, 043824 (2010).

94. **Xu, F., Lock, J. A. and Tropea, C.** Debye series for light scattering by a spheroid. *J. Opt. Soc. Am.* A27, 671–686 (2010).

95. **Xu, F., Ren, K. F. and Cai, X. S.** Extension of geometrical-optics approximation to on-axis Gaussian beam scattering. I. By a spherical particle. *Appl. Opt.* 45, 4990–4999 (2006).

96. **Yarin, A. L., Pfaffenlehner, M. and Tropea, C.** On the acoustic levitation of droplets. *J. Fluid Mech.* 356, 65–91 (1998).

97. **Yu, H. T.** Study of geometrical optics approximation of light scattering. *Master Dissertation.* University of Shanghai for Science and Technology (2008).

98. **Yu, H. T., Shen, J. Q. and Wei, Y. H.** Geometrical optics approximation for light scattering by absorbing spherical particles. *J. Quant. Spectosc. Radiat. Transfer*, 110: 1178–1189 (2009).

99. **Yu, H. T., Shen, J. Q. and Wei, Y. H.** Geometrical optics approximation of lightscattering by large air bubbles. *Particuology*, 6, 340–346 (2008).

100. **Yu, H. T., Xu, F. and Tropea, C.** Application of generalized rainbow patterns on spheroidal droplets measurement. in the 21st GALA Conference on Laser Methods in Fluid Measurement (3–5 September, München), 57.1–57.8 (2013).

101. **Yu, H. T., Xu, F. and Tropea, C.** Optical caustics associated with the primary rainbow of oblate droplets: simulation and application in non-sphericity measurement. Opt. Express, 21, 25761–25771 (2013).

102. **Yu, H. T., Xu, F. and Tropea, C.** Simulation of optical caustics associated with the secondary rainbow of oblate droplets. Opt. Lett. 38, 4469–4472 (2013).

103. **Yu, H. T., Xu, F. and Tropea, C.** Spheroidal droplet measurements based on generalized rainbow patterns. J. Quant. Spectosc. Radiat. Transfer, 126, 105–112 (2013).

Publication list

1. Haitao Yu, Feng Xu, and Cameron Tropea, Simulation of optical caustics associated with the secondary rainbow of oblate droplets, Optics Letters, 38(21), 4469–4472 (2013).

2. Haitao Yu, Feng Xu, and Cameron Tropea, Optical caustics associated with the primary rainbow of oblate droplets: simulation and application in non-sphericity measurement, Optics Express, 21(22), 25761–25771 (2013).

3. Haitao Yu, Feng Xu, and Cameron Tropea, Application of generalized rainbow patterns on spheroidal droplets measurement, in the 21st GALA Conference on Laser Methods in Fluid Measurement (3-5 September 2013, München), 57.1–57.8.

4. Haitao Yu, Feng Xu, and Cameron Tropea, Spheroidal droplet measurements based on generalized rainbow patterns, Journal of Quantitative Spectroscopy and Radiative Transfer, 126, 105–112 (2013).

Conference reports

1. Haitao Yu, Feng Xu, and Cameron Tropea, Application of generalized rainbow patterns on spheroidal droplets measurement, in the 21st GALA Conference on Laser Methods in Fluid Measurement, Munich, Germany, 3–5 September 2013.

2. Haitao Yu, Feng Xu, and Cameron Tropea, Spheroidal droplet measurements based on generalized rainbow patterns, in the 9th Lasers and Interactions with Particles, Rouen, France, 26–30 March 2012.

Participated research projects

1. Optical characterization for non-spherical droplet, supported by GRK 1114: Optical techniques for measurement of interfacial transport phenomena (DFG, 52400053), 01.2013–03.2014.

2. Development of Debye series for light scattering by a spheroid, supported by German Research Foundation (DFG, TR 194/49-1), 05.2009–05.2012.

Curriculum Vitae

Personal Data

Name	Haitao Yu
Date of Birth	25 October 1980
Place of Birth	Province Shandong, China
Nationality	Chinese

Education

November 2009 – November 2013	Doctor degree
	Fachgebiet Strömungslehre und Aerodynamik,
	Technische Universität Darmstadt, Darmstadt, Germany
September 2006 – March 2009	Master Degree
	College of Science, University of Shanghai for Science
	and Technology, Shanghai, China
September 2004 – July 2006	Bachelor degree
	College of Physics and Electronic Engineering, Ludong
	University, Yantai, China
September 2001 – July 2004	Bachelor student
	College of Physics and Electronic Engineering, Yantai
	Normal University, Yantai, China